Terms and Conditions of Use of Digitised Theses from Trinity College Library Dublin

Copyright statement

All material supplied by Trinity College Library is protected by copyright (under the Copyright and Related Rights Act, 2000 as amended) and other relevant Intellectual Property Rights. By accessing and using a Digitised Thesis from Trinity College Library you acknowledge that all Intellectual Property Rights in any Works supplied are the sole and exclusive property of the copyright and/or other IPR holder. Specific copyright holders may not be explicitly identified. Use of materials from other sources within a thesis should not be construed as a claim over them.

A non-exclusive, non-transferable licence is hereby granted to those using or reproducing, in whole or in part, the material for valid purposes, providing the copyright owners are acknowledged using the normal conventions. Where specific permission to use material is required, this is identified and such permission must be sought from the copyright holder or agency cited.

Liability statement

By using a Digitised Thesis, I accept that Trinity College Dublin bears no legal responsibility for the accuracy, legality or comprehensiveness of materials contained within the thesis, and that Trinity College Dublin accepts no liability for indirect, consequential, or incidental, damages or losses arising from use of the thesis for whatever reason. Information located in a thesis may be subject to specific use constraints, details of which may not be explicitly described. It is the responsibility of potential and actual users to be aware of such constraints and to abide by them. By making use of material from a digitised thesis, you accept these copyright and disclaimer provisions. Where it is brought to the attention of Trinity College Library that there may be a breach of copyright or other restraint, it is the policy to withdraw or take down access to a thesis while the issue is being resolved.

Access Agreement

By using a Digitised Thesis from Trinity College Library you are bound by the following Terms & Conditions. Please read them carefully.

I have read and I understand the following statement: All material supplied via a Digitised Thesis from Trinity College Library is protected by copyright and other intellectual property rights, and duplication or sale of all or part of any of a thesis is not permitted, except that material may be duplicated by you for your research use or for educational purposes in electronic or print form providing the copyright owners are acknowledged using the normal conventions. You must obtain permission for any other use. Electronic or print copies may not be offered, whether for sale or otherwise to anyone. This copy has been supplied on the understanding that it is copyright material and that no quotation from the thesis may be published without proper acknowledgement.

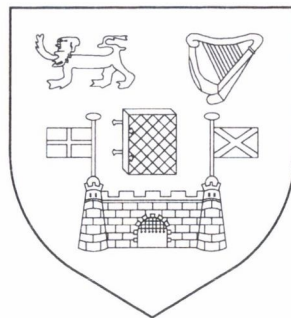# Comparing the excitations of the periodic flux tube with effective string models.

by

Francesca Maresca

Dottore in Fisica and M.Sc.

A Thesis submitted to
The University of Dublin
for the degree of

Doctor in Philosophy

Department of Mathematics
University of Dublin
Trinity College

July, 2004

Declaration

This thesis has not been submitted as an exercise for a degree at any other University. Except where otherwise stated, the work described herein has been carried out by the author alone. This thesis may be borrowed or copied upon request with the permission of the Librarian, University of Dublin, Trinity College. The copyright belongs jointly to the University of Dublin and Francesca Maresca.

Signature of Author.............. *Francesca Maresca* ....

Francesca Maresca
09 July, 2004

Summary

The spectrum of a periodic flux tube in pure SU(3) Yang-Mills theory is evaluated non-perturbatively through computations on the lattice in the region from intermediate to long distances ($1.5 < L < 4$ fm). For these flux lengths our results are compared with the predictions of a bosonic effective string theory, finding a surprising good agreement. The main object of the first part of this work is the description of the lattice technology and methodology used to evaluate the spectrum of a periodic flux tube. We give details of the improved anisotropic lattice action we used in our calculations and of the methodology we adopted in order to identify the symmetries of a periodic flux tube that winds around one direction. A large number of torelon operators are then systematically constructed and details on the implementation and on the form of these operators are also given. We perform several long numerical Monte Carlo simulations for different flux lengths and with different volumes and different values of β. The second part of this work is dedicated to the description of an effective string theory with central charge not equal to the dimension d and the resulting covariant quantization with $d - 2$ oscillators presented by Polchinski and Strominger in 1991. However, as it is also clear from their article, the spectrum derived from it does not deviate from the Nambu-Goto spectrum at least for the corrections they introduced. We then proceed to compare the spectrum of the QCD periodic flux tube with the string expectations. Our numerical results confirm the string-like flux formation and details are given regarding the Lüscher term in the ground state, the level ordering, degeneracy and energy gaps between levels. The agreement with a string theory is striking in the presence of the Lüscher term, in the level ordering and in the degeneracy of all of the fourteen states we considered (apart from the $A_{2u}(0)$ state that reaches a perfect degeneracy only at $L > 2.5$ fm and the problematic $A_2(1)$ state which seems to show a string-like behavior for bigger L). The deviations from the string energy gap for lengths $L > 2.5$ fm is problematic and already seen in the spectrum of a quark-antiquark system. Further studies are required in order to settle this issue.

Acknowledgements

In memory of Oscar

Contents

List of Figures

List of Tables

Introduction

The theory of strong interactions, quantum chromodynamics (QCD), was formulated 30 years ago and has since been a very active field of research. Nowadays, there is no doubt that QCD is in reasonable agreement with experimental results of high-energy scattering, however work has still to be done to answer the question whether QCD is the correct theory of strong interactions at all scales or just an effective high-energy limit of a yet undiscovered theory. For instance, the infrared regime of QCD is very hard to treat theoretically, since the usual field-theoretical methods are not adequate for this theory. This is because the QCD coupling constant $\alpha(q^2)$ increases at small momentum transfers, reaching a value comparable to 1 at momenta q around $\sqrt{|q^2|} \approx 500$ MeV [1]. A power-series expansion in α does not converge, which makes the Feynman diagrammatic technique inapplicable in this region.

Therefore QCD at small momenta or energies $E \leq 1$ GeV has to be treated non-perturbatively and up to now the best method available is lattice gauge theory. Various ideas and methods elaborated during the last two decades, together with the development of algorithms for numerical calculations and progress in computer technology have made lattice gauge theory one of the most powerful tools for the evaluation of non-perturbative characteristics of QCD.

In a lattice simulation, Euclidean space-time is discretized on a torus with L^4 points separated by the lattice spacing a, which provides an ultra-violet cut-off. While the dirac fields, q_x, are represented by 4-tuples at lattice sites, x, the gauge fields live on the links that connect two sites. The lattice allows for a *first principles* numerical

1

evaluation of expectation values of any observable $\mathcal{O}$ from the computation of the path integral,

$$\langle\mathcal{O}(U,q,\bar{q})\rangle = \int [dU][dq][d\bar{q}]\mathcal{O}[U,q,\bar{q}]e^{-S(U,q,\bar{q})}, \tag{1}$$

where the high-dimensional integral is evaluated by means of a stochastic Monte-Carlo method as an average over an ensemble of n *representative* gauge configurations. An introduction on the recent advances in lattice simulation technology, including particular attention to anisotropic lattice and improved gauge actions is given in Chapter 1.

The most fundamental problem associated with the infrared dynamics of QCD is the explanation and description of *confinement*. In general, by confinement one implies that there are no isolated particles in Nature with non-vanishing color charge, that is, all asymptotic particle states ($|\text{in}\rangle$ and $|\text{out}\rangle$) are color singlets. Unfortunately there is no derivation of quark confinement starting from first principles nor is there a totally convincing explanation of the effect (see Ref. [2] for a review). By numerically simulating gauge theories on the lattice one can predict properties and give hints to the underlying mechanisms of quark confinement.

One common choice of order parameter for confinement to be studied on the lattice is the Wilson loop. It is defined as the trace of the product of gauge variables along a closed oriented contour, ∂C, enclosing an area, C,

$$\langle W(C)\rangle = \text{Tr}\left\{\mathcal{P}\left[exp\left(\int_{\partial C} dx_\mu A_\mu(x)\right)\right]\right\}. \tag{2}$$

The Wilson loop can be related to the potential energy of a pair of static color sources (see Wilson's original work [3] or a more recent monograph [7]), in particular when the contour ∂C is a rectangular of dimension $C = \mathbf{r} \times t$, eq. (2) can be re-expressed as

$$\langle W(C) \rangle = \sum_n |c_n|^2 e^{-E_n t}. \tag{3}$$

In the limit of large t, the ground state E_0 that will dominate in eq. (3) can be identified as the potential between two static quarks separated by a distance $\mathbf{r}$, i.e. $E_0 = V(\mathbf{r})$.

Lattice gauge theory provides an exact result for the static potential by simply exploiting the symmetry of a Wilson loop under the interchange of space and time directions and by using the reflection positivity of Euclidean n-point functions. In fact, it can be proved [8] that the static potential cannot rise faster than linearly as a function of the distance $\mathbf{r}$ in the limit $\mathbf{r} \to \infty$ and moreover it is a convex function, i.e.

$$\frac{dV}{dr} > 0 \qquad \text{and} \qquad \frac{d^2V}{dr^2} \leq 0. \tag{4}$$

Expectation values, as in eq. (2), can also be approximated by expanding the exponential of the lattice action in eq. (1), in terms of the lattice coupling constant β. From this strong coupling expansion one obtains the expectation value

$$\langle W(C) \rangle = \begin{cases} (\beta/4)^{-C} + \dots, & N = 2 \\ (\beta/2N^2)^{-C} + \dots & N > 2, \end{cases} \tag{5}$$

where C is the area of the Wilson loop. Considering therefore the case of a rectangular Wilson loop that extends r/a points into a spatial direction and t/a points into the temporal direction one finds the area law

$$\langle W(C) \rangle = \exp[-\sigma r t] + \dots, \tag{6}$$

with a string tension

$$\sigma a^2 = -\ln \frac{\beta}{18}. \tag{7}$$

The fact that lattice gauge theories confirmed the area law for Wilson loops, which is one important characteristic of the confining force, does not give a conclusive answer to the question of whether QCD is the right theory for confinement since bag models also predict a linear rising of the ground state energy [1, 37].

Probably the most striking feature of the confining force that could be checked using the lattice technology is its string-like behavior. In fact, the strong coupling expansion of a Wilson loop can be cast into a sum of weighted random deformations of the minimal area world sheet and this sum can be interpreted as representing a vibrating string. The idea that the chromoelectric flux between two static sources is squeezed into a thin flux tube and that this can be regarded as a string is a fascinating conjecture that has been explored with Monte-Carlo simulations by different lattice collaborations [33, 45, 36]. The string action to be employed is not a priori known, but the simplest possible assumption is that the string is described by the Nambu-Goto action in terms of the $(d-2)$ transverse degrees of freedom of the string. The bosonic string model predicts the existence in the potential of the ground state of a term proportional to $1/r$, the so-called Lüscher term and also how the thickness of a QCD flux tube depends on the separation, r of the quarks. In contrast to the string picture that finds a logarithm dependence on r for the flux width, the strong coupling lattice gauge theory found that the width of the flux tube remains finite at $r \to \infty$, for small β [6]. However, the strong coupling expansion seems to break down at a certain value of the coupling constant and nowadays it is a well accepted fact that the confining regime of lattice gauge theories contains two phases: the strong coupling phase and the rough phase. The two are separated by the so-called *roughening transition* which is the point in which the strong coupling ceases to converge. While at strong coupling the dynamics is confined to the minimal area spanned by a

Wilson loop (plus small "bumps" on top of the surface) and the fluctuations of the flux tube are massive, as the coupling decreases, the color fields between the sources can penetrate over several lattice sites into the vacuum and the fluctuations of the flux tube become massless.

Lüscher and Weisz [4] were able to compute the static potential in SU(3) lattice gauge theory in $d = 3, 4$ to very high accuracy, and extract

$$c(r) = -\frac{24}{\pi(d-2)} r^3 \frac{\partial^2 V}{\partial r^2}, \tag{8}$$

from the second lattice derivative of $V(r)$, in the range 0.2 fm $< r < 1.0$ fm . The value of $c(r)$ breaks away from the short-distance running Coulomb law towards the string-like $c(r) \approx 1$ behavior for values of r surprisingly well below 1 fm. Independent investigations by Juge et al. [36] on the excitation spectrum of the flux tube between two static sources also gave evidence of its string-like behavior. However their studies showed a complex non-string level ordering for quark separation $r < 2$ fm and a crossover around 2 fm, a value far from the one found by Lüscher and Weisz.

In $d = 4$ it is hard to disentangle the large-distance $1/r$ term (the Lüscher term) expected from the string vibrations, from the perturbative Coulomb term at short distances. A way out is to determine the mass of a closed string, encircling a boundary of the lattice for which the string correction term is four times as large as for the static potential. Adopting the viewpoint of Juge at al. [36] that the nature of the confining gluon field is best revealed in its excitation spectrum we started a series of studies on the spectrum of a periodic flux tube that we present in Chapter 2. In fact, the absence of fixed color sources in a periodic flux tube provides a particularly favorable theoretical environment in which to observe the onset of string behavior. Comparisons with an effective string theory are also presented in Chapter 3.

Chapter 1

Lattice gauge theories (LGT)

1.1 Introduction

Progress in Lattice QCD has required a combination of improvements in formulation, numerical techniques and computer technology. When Lattice QCD was invented, in the mid 1970's, most of the lattice theorist's effort was spent in accumulating computer time on the world's largest supercomputers or in designing and building faster computers. In fact, until very recently it was thought that the lattice spacings as small as $.05 - .1$ fm would be essential for reliable simulations of QCD. The formula that governs the computing time cost of a full QCD simulation is given by

$$\text{cost} \approx \left(\frac{L}{a}\right)^4 \left(\frac{1}{a}\right) \left(\frac{1}{m_\pi^2 a}\right), \tag{1.1}$$

where the first factor is just the number of lattice sites in the grid, and the remaining factors account for the "critical slowing down" of the algorithms used in the numerical integration as described in Ref. [12]. The formula in eq. (1.1) clearly shows that the single most important factor is the lattice spacing, therefore making most simulations prohibitive. Improved discretizations and therefore the possibility to work with large lattice spacings are old ideas, pioneered by Wilson

and Symanzik and others [9]. Coarse lattices offer the advantage of a significant reduction in computation overheads making the simplest calculations possible on a personal computer. However an attempt to use improved actions on coarse lattices to examine the glueball spectrum of QCD proved to be very difficult [10]. This is due to the fact that the number of correlator time intervals which can be measured is reduced greatly when the masses in lattice units are large (as in the case of the glueball spectrum). A solution to this problem is to make use of anisotropic lattices in which the temporal spacing is much smaller than that in the spatial directions. In this chapter we want to summarize briefly the recent advances in lattice simulation technology on anisotropic lattices that we employed in our series of studies.

1.2   Anisotropic formulation of LGT

A lattice calculation is a non-perturbative implementation of field theory using the path integral approach. The Euclidean space-time is discretized on a torus with $L_s^3 L_t$ lattice points separated by lattice spacings a_s and a_t in the spatial direction and in the temporal direction respectively. The lattice spacing provides an ultraviolet cut-off on the gluonic momentum $q_i < \frac{\pi}{a_i}$ and regulates the theory. The gauge degrees of freedom are then represented by oriented links connecting two adjacent sites:

$$U_\mu(x) = \mathcal{P}[e^{-ig \int_x^{x+a\hat{\mu}} A \cdot dy}] \approx e^{-iag A_\mu^b T_b} \in SU(N), \qquad (1.2)$$

where T_b are the generators of $SU(N)$ and the $\mathcal{P}$-operator orders the A_μ's along the integration path. Under a gauge transformation $G(x) \in SU(N)$ these links transform as

$$U_\mu(x) \rightarrow U_\mu(x)^G = G(x)U_\mu(x)G^\dagger(x + a\hat{\mu}), \qquad (1.3)$$

from which it is clear that the trace of a product of links along a closed loop is

gauge invariant. These loops, the Wilson loops, can have an arbitrary shape and size and can be taken to lie in any representation of $SU(N)$. Lattice actions are then constructed in a manifestly gauge-invariant way and should approach the continuum action, $S_{YM} = \frac{1}{2} \int d^4 x \text{Tr} F_{\mu\nu} F_{\mu\nu}$ in the limit a_t, $a_s \to 0$.

The simplest non-trivial gauge-invariant objects that can be constructed are the traces of the following spatial (sp) and temporal plaquettes (tp),

$$U_{sp} = U_i(x) U_j(x + \hat{i}) U_i^\dagger(x + \hat{j}) U_j^\dagger(x), \tag{1.4}$$

$$U_{tp} = U_t(x) U_i(x + \hat{t}) U_t^\dagger(x + \hat{i}) U_i^\dagger(x), \tag{1.5}$$

from which it is possible to construct the simplest lattice action. In fact, one readily verifies that the following action possesses the naive correct continuum limit

$$S_G[U] = \beta(\frac{1}{\xi} \Omega_{sp} + \xi \Omega_{tp}) = \frac{1}{2} \int d^4 x \text{Tr} F_{\mu\nu} F_{\mu\nu} + O(a_s^2, a_t^2), \tag{1.6}$$

where $\beta = \frac{2N}{g^2}$, g is the QCD coupling, ξ is the anisotropic parameter a_s/a_t and the Ω's are explicitly given in terms of the plaquettes,

$$\Omega_{sp} = \sum_x \sum_{i>j} \frac{1}{3} \text{ReTr}(1 - U_{sp}), \tag{1.7}$$

$$\Omega_{st} = \sum_x \sum_i \frac{1}{3} \text{ReTr}(1 - U_{tp}). \tag{1.8}$$

Once the gauge degrees of freedom and the action have been defined the expectation value of any observable $O[U]$ can be determined by the computation of the path integral

$$<O> = \frac{1}{\mathcal{Z}} \int D[U] O[U] e^{-S[U]}, \tag{1.9}$$

8

where $\mathcal{Z} = \int D[U]e^{-S[U]}$ is the partition function and $D[U] = \Pi_{x,\mu}dU_\mu(x)$ is the Haar measure.

The high-dimensional integral is then evaluated by means of a stochastic Monte-Carlo method as an average over an ensemble of n representative gauge configurations $C_i = \{U_\mu^i(x)\}_{i=1...n}$,

$$< O > = \frac{1}{n}\sum_{i=1}^{n}O[C_i] + \Delta\mathcal{O}(\frac{1}{\sqrt{n}}). \tag{1.10}$$

1.3 Continuum limit and improvement

The expansion of the link variable in eq. (1.2) shows the presence of higher dimensional operators. For instance, examining the spatial plaquette by means of Stoke's theorem [12],

$$
\begin{aligned}
\oint_\square A \cdot dx &= \int_{-\frac{a}{2}}^{\frac{a}{2}} dx_i dx_j \left(\partial_i A_j(x_0 + x) - \partial_j A_i(x_0 + x)\right) \\
&= a_s^2 F_{ij}(x_0) + \frac{1}{24}a_s^4(D_i^2 + D_j^2)F_{ij}(x_0),
\end{aligned}
\tag{1.11}
$$

we readily find

$$\frac{1}{N}\text{Re Tr}(1 - U_{sp}) = \frac{1}{N}g^2\left[\frac{a_s^4}{2}\text{Tr}F_{ij}F_{ij} + \frac{a_s^6}{24}\text{Tr}F_{ij}(D_i^2 + D_j^2)F_{ij}\right], \tag{1.12}$$

and similarly for the temporal plaquette,

$$\frac{1}{N}\text{Re Tr}(1 - U_{tp}) = \frac{1}{N}g^2\left[\frac{a_s^2 a_t^2}{2}\text{Tr}F_{it}F_{it} + \frac{a_s^4 a_t^2}{24}\text{Tr}F_{it}D_i^2 F_{it} + \frac{a_s^2 a_t^4}{24}\text{Tr}F_{it}D_t^2 F_{it}\right]. \tag{1.13}$$

9

The higher dimensional operators in eq. (1.12) and (1.13) are suppressed by powers of the lattice spacing and therefore are irrelevant operators.

However, the choice of the lattice action is far from unique and one is free to add any irrelevant operator with a sensible strength and still recover QCD continuum limit. The Symanzik's improvement program [11] employs this strategy in order to reduce discretization errors. This allows one to work on coarser lattices (smaller L_s, L_t) for a given accuracy and consequently to reduce computer time.

The representation of gauge fields by eq. (1.2) also gives rise to lattice artifacts due to the presence of higher order terms of gaA_μ and the A_μ's if contracted with each other generate tadpole contributions. Parisi, Lapage and Mackenzie, in [13, 14], proposed a mean-field improvement to get rid of these artifacts. In the following sections, the Symanzik approach and the tadpole (mean-field) improvement will be briefly explained and applied to anisotropic lattices.

1.4   Symanzik's improvement

As mentioned in the previous section, any lattice operator $\mathcal{O}$, constructed from the link variables, will have an asymptotic expansion for a_s, $a_t \to 0$ of the form

$$\mathcal{O} \approx \sum_{k=0}^{\infty} a_s^{k_s} a_t^{k_t} \left(\sum_{\alpha}^{M(k)} r_\alpha^{(k)} O_\alpha^{(k)} \right), \qquad (1.14)$$

where $O_\alpha^{(k)}$ are local continuum operators with dimension $k = k_s + k_t$. Moreover, when the lattice operator $\mathcal{O}$ is invariant under gauge transformations, rotations and reflections the operators $O_\alpha^{(k)}$ that can occur in the expansion (1.14) are severely restricted since they must have the same symmetries of $\mathcal{O}$.

It turns out that there are only two dimension-four operators,

$$O_1^{(4)} = g^2 \sum_{ij} \text{Tr} F_{ij} F_{ij} \quad \text{and} \quad O_2^{(4)} = g^2 \sum_{i} \text{Tr} F_{it} F_{it}.$$

There are no dimension-five operators and eighteen independent, dimension-six operators, ten of which may be expressed as unimportant total derivatives [15]. To eliminate $O(a^2)$ lattice artefacts one can perform an asymptotic expansion of a suitable lattice action and adjust the interaction couplings so as to reproduce the correct continuum QCD action with the $O(a^2)$ terms absent. For instance, a general improved action can be written as,

$$S[U] = \frac{2N}{g^2} \sum_{i} c_i(g^2) O_i[U], \tag{1.15}$$

where $O_i[U]$ are the lattice operators defined by

$$O_i[U] = \sum \frac{1}{N} \text{ReTr}(1 - U_C), \tag{1.16}$$

U_C being the ordered product of link variables along a closed loop C. There are several elementary loops on the lattice that can occur in the improved action of eq. (1.15). We are going to follow the choice of C. Morningstar and M. Peardon [16, 17] who adopted an improved action with the spatial and temporal plaquette U_{sp}, U_{tp}, the planar 2×1 spatial rectangles U_{sr} and the short temporal rectangles U_{str} given respectively by eq. (1.4), (1.5) and

$$U_{sr} = U_i(x)U_i(x+\hat{\imath})U_j(x+2\hat{\imath})U_i^\dagger(x+\hat{\imath}+\hat{\jmath})U_i^\dagger(x+\hat{\jmath})U_j^\dagger(x), \tag{1.17}$$

$$U_{str} = U_i(x)U_i(x+\hat{\imath})U_t(x+2\hat{\imath})U_i^\dagger(x+\hat{\imath}+\hat{t})U_i^\dagger(x+\hat{t})U_t^\dagger(x). \tag{1.18}$$

By means of Stoke's theorem it is easy to find the asymptotic expansion of the spatial and temporal rectangles,

$$\frac{1}{N}\text{Re Tr}(1 - U_{sr}) = \frac{g^2}{N}\left[2a_s^4\text{Tr}F_{ij}F_{ij} + \frac{2a_s^6}{3}\text{Tr}F_{ij}D_i^2F_{ij} + \frac{2a_s^6}{12}\text{Tr}F_{ij}D_j^2F_{ij}\right], \quad (1.19)$$

and similarly for the temporal rectangles,

$$\frac{1}{N}\text{ReTr}(1 - U_{str}) = \frac{g^2}{N}\left[2a_s^2a_t^2\text{Tr}F_{ij}F_{ij} + \frac{2a_s^4a_t^2}{3}\text{Tr}F_{it}D_i^2F_{it} + \frac{2a_s^2a_t^4}{12}\text{Tr}F_{it}D_t^2F_{it}\right].$$
$$(1.20)$$

The interaction couplings c_i in the improved action

$$S = \frac{1}{\xi}c_1\Omega_{sp} + \xi c_2\Omega_{tp} + \frac{1}{\xi}c_3\Omega_{sr} + \xi c_4\Omega_{str}, \quad (1.21)$$

can then be chosen to eliminate $O(a_s^2)$ errors. Here Ω_{sp} and Ω_{tp} are given by eq. (1.7) and (1.8) and Ω_{sr}, Ω_{str} by

$$\Omega_{sr} = \sum_x \sum_{i \neq j} \frac{1}{3}\text{ReTr}(1 - U_{sr}), \quad (1.22)$$

$$\Omega_{str} = \sum_x \sum_i \frac{1}{3}\text{ReTr}(1 - U_{str}). \quad (1.23)$$

Using the asymptotic expansion given above we find that imposing the following three constraints at tree-level

$$\frac{1}{4}c_1 + \frac{1}{4}c_2 + 2c_3 + c_4 = \frac{1}{2},$$
$$\frac{1}{24}c_1 + \frac{5}{6}c_3 = 0,$$
$$\frac{1}{24}c_2 + \frac{2}{3}c_4 = 0, \quad (1.24)$$

the classical action

$$S = \beta \left\{ \frac{5}{3\xi} \Omega_{sp} + \frac{4\xi}{3} \Omega_{tp} - \frac{1}{12\xi} \Omega_{sr} - \frac{\xi}{12} \Omega_{str} \right\}, \qquad (1.25)$$

has $O(a_t^2, a_s^4)$ discretization errors.

The $O(a_t^2)$ error can be removed by the addition of counterterms which couple next-nearest-neighbor time slices, for instance by adding the tall temporal rectangle in the lattice action [15]. However, this operator introduces spurious high-energy modes that have detrimental effects on the correlation functions [18].

1.5 Tadpole Improvement

It was noticed that traditional perturbation theory for lattice QCD begins to fail at distances of order 1/20 to 1/10 fm and therefore lattice spacings must be at least this small before improved actions are useful. A trivial modification of lattice QCD, called "tadpole improvement" allows perturbation theory to work even at distances as large as 1/2 fm, as phenomenological applications of continuum perturbative QCD suggested [12]. The cause of the mismatch between perturbation theory for lattice QCD and for the continuum resides in the fact that all gluonic operators in lattice QCD are built from the link operator,

$$U_\mu(x) = e^{-iagA_\mu(x)} \approx 1 - iagA_\mu(x) - \frac{a^2 g^2}{2} A_\mu^2(x), \qquad (1.26)$$

rather than from the vector potential $A_\mu(x)$.

In fact, contracting the two gluons in $a^2 g^2 A_\mu^2(x)/2$ gives rise to tadpole diagrams. However tadpole contributions are generally process independent and so it is possible to measure their contribution in one quantity and then correct for them in all other quantities. Assuming that we can evaluate the tadpoles contribution in the link operators,

$$U_i(x) = u_s \tilde{U}_i(x), \qquad\qquad (1.27)$$

and

$$U_t(x) = u_t \tilde{U}_t(x), \qquad\qquad (1.28)$$

we can then replace every lattice operator by $U_i(x) \rightarrow U_i(x)/u_s$ and $U_t(x) \rightarrow U_t(x)/u_t$.

The tadpole factors u_s and u_t are computed numerically in a simulation. They are determined by guessing input values for use in the action, measuring the values of $\langle \frac{1}{3}\mathrm{ReTr}U_{sp}\rangle^{\frac{1}{4}}$ and $\langle \frac{1}{3}\mathrm{ReTr}U_{tp}\rangle^{\frac{1}{4}}$ respectively [1], then readjusting the input values accordingly. Since in the Landau-gauge perturbation theory, $1 - \langle \frac{1}{3}\mathrm{Tr}U_t\rangle \propto (a_t/a_s)^2$, when a_t is significantly smaller than a_s, we can safely set $u_t = 1$. Applying tadpole improvement in our action of eq. (1.25) we get,

$$S = \beta \left\{ \frac{5}{3\xi u_s^4}\Omega_{sp} + \frac{4\xi}{3u_s^2 u_t^2}\Omega_{tp} - \frac{1}{12\xi u_s^6}\Omega_{sr} - \frac{\xi}{12\ u_s^4 u_t^2}\Omega_{str} \right\}. \qquad (1.29)$$

Tadpole improvement is the first step in a systematic procedure for improving the action. The next step is to add in renormalizations due to contributions from $k > \pi/a$ physics not already included in the tadpole improvement. However the coefficients of the correction terms in the gluonic action (1.29) are known only to the leading order in α_s (so that the action (1.29) has leading $O(a_s^4, a_t^2, \alpha_s a_s^2)$ discretization errors). In principle the coefficients of the correction terms should be computed by "matching" physical quantities computed using perturbation theory in the lattice with the analogous quantities in the continuum. It is, however, clear from the simulations [20, 12, 17] that tree-level tadpole improvement automatically captures most of the $O(\alpha_s)$ corrections. Also, the restoration of continuum symmetries can be used as

---

[1] Alternatively the mean link can be determined evaluating the expectation value of the link in Landau gauge.

a criterion for tuning the input parameters (i.e. spatial mean link u_s, anisotropic parameter) beyond their tadpole-improved tree-level values. In Section 1.7 we describe in detail how the tuning is performed.

1.6   Further improvement

In the seminal work on the glueball spectrum [17] C. Morningstar and M. Peardon noticed that the Symanzik-tadpole-improved action of eq. (1.29) gave good scaling for the 2^{++} and 1^{+-} glueballs. However they also found that for the lightest, scalar state, the mass (in unit of r_0) was seen to fall rapidly to a minimum when the spatial lattice spacing is ≈ 0.25 fm, where the scaling violations are $\approx 25\%$ and then rise as the lattice spacing is increased further: the so-called "scalar dip". In comparison with Wilson simulations, the use of the improved action reduced the depth of the dip, but only by about a third. It has been conjectured that this dip may be related to the presence of a critical endpoint in a line of phase transitions in gluonic actions that include an adjoint coupling [23, 26]. It is indeed known that pure $SU(3)$ lattice gauge theory containing fundamental and adjoint representations of the gauge fields undergoes a first order phase transition for positive values of the adjoint coupling [24, 25, 26]. From the action constructed from plaquettes in both the fundamental and the adjoint representations of $SU(N)$

$$S = \beta_f \sum \left(1 - \frac{1}{N}\mathrm{ReTr}U_{sp}\right) + \beta_A \sum \left(1 - \frac{1}{N^2}|\mathrm{ReTr}U_{sp}|^2\right), \tag{1.30}$$

various authors revealed a non-trivial phase structure and in particular a critical endpoint. A current estimate (see Ref. [26]) of the location of this endpoint for $SU(3)$ gauge theory is $(\beta_f, \beta_A) = (4.00(7), 2.06(8))$, that lies well above the β_f axis. This is consistent with the observation that there is no discontinuity in the behavior of the expectation values of Wilson loops and in the glueball masses, obtained with

fundamental loop actions ($\beta_A = 0$). This implies that it is safe to take the continuum limit along the line $\beta_A = 0$. However, U. Heller [26] showed that at the critical endpoint the scalar glueball mass $m_{0^{++}}$ vanishes and along the line $\beta_A = 0$, although there are no singularities, this critical endpoint could cause significant deviations in the scaling for the scalar glueball mass, the "scalar dip" found in both the Wilson action and improved actions. It is also expected that on a trajectory that lies below the β_f axis (negative β_A) the influence of the endpoint should be less than along $\beta_A = 0$. To test this conjecture C. Morningstar and M. Peardon [16, 29] added adjoint-like terms to the anisotropic action of eq. (1.29):

$$\Omega_{sp}^{(2t)} = \frac{1}{2} \sum_{x, i>j} \left[1 - \frac{1}{N^2} \left(\mathrm{ReTr} U_{sp}(x) \right) \left(\mathrm{ReTr} U_{sp}(x+t) \right) \right]. \tag{1.31}$$

This term correlates pairs of spatial plaquettes separated by one site temporally. The separation of the two plaquettes allows the standard Cabibbo-Marinari and over-relaxation gauge field update methods to be applied. The asymptotic expansion of eq. (1.31) is readily found to be identical to Ω_{sp} up to $O(a_s^4)$

$$\sum_{x, i>j} \left[1 - \left(1 - \frac{g^2}{2N} \mathrm{ReTr} \left(\oint_{\square_x} A \cdot dx \right)^2 \right) \left(1 - \frac{g^2}{2N} \mathrm{ReTr} \left(\oint_{\square_{x+i}} A \cdot dx \right)^2 \right) \right] =$$
$$= \sum_{x, i>j} \frac{g^2}{N} \left[\frac{a_s^4}{2} \mathrm{Tr} F_{ij}(x) F_{ij}(x) + \frac{a_s^6}{24} \mathrm{Tr} F_{ij}(x) (D_i^2 + D_j^2) F_{ij}(x) \right] \tag{1.32}$$

This also implies that the operator combination

$$\tilde{\Omega}_{sp} = (1 + \omega) \Omega_{sp} - \omega \Omega_{sp}^{(2t)}, \tag{1.33}$$

has an identical expansion in powers of the lattice spacing to Ω_{sp} for all values of ω up to $O(a_s^4)$. Thus, starting from the improved action in eq. (1.29) it is straightforward to construct a Symanzik improved, two-plaquette action by simply replacing the

spatial plaquette term in eq. (1.29) with the linear combination $\tilde{\Omega}_{sp}$. In full this action is

$$S = \beta \left\{ \frac{5(1+\omega)}{3\xi u_s^4} \Omega_{sp} + \frac{4\xi}{3u_s^2 u_t^2} \Omega_{tp} - \frac{5\omega}{3\xi u_s^8} \Omega_{sp}^{(2t)} - \frac{1}{12\xi u_s^6} \Omega_{sr} - \frac{\xi}{12 u_s^4 u_t^2} \Omega_{str} \right\}. \quad (1.34)$$

It has leading $O(a_s^4, a_t^2, \alpha_s a_s^2)$ discretization errors and only connects sites on adjacent time-slices, ensuring the free gluon propagator has only one real mode. In the next section we will describe how to set this free parameter in such a way that physical mass ratios are independent of ω.

1.7 Tuning the parameters

Tadpole parameters.

As we have already mentioned in the previous sections the coefficients of each term in the action (1.34), obtained using the Symanzik approach, are chosen so that the action has no $O(a_s^2)$ discretization errors in tree-level perturbation theory. Tadpole improvement of the perturbative expansion is achieved by tuning the input spatial tadpole parameter u_s ($u_t = 1$, since $a_t \ll a_s$) for self-consistency at each choice of β and ξ. For instance, the expectation value of the spatial plaquette is computed for a range of input parameters u_s close to the self-consistent value $u_s^\star$. A linear interpolation is sufficient to give an accurate value of $u_s^\star$. This value is then checked in a further Monte-Carlo simulation.

Anisotropy

The anisotropic parameter ξ is equal to the aspect ratio of the spatial and temporal lattice spacings, a_s and a_t at tree-level. At higher orders in the perturbative expansion, this aspect ratio receives quantum corrections, so a renormalized anisotropy

17

determined from a physical process, ξ_R, differs from ξ at $O(\alpha_s)$. The renormalization of the anisotropy can be determined by measuring the static-quark potential $V(x, y, z)$ from Wilson loops in different orientations. Following a procedure similar to Ref. [21], the potentials between two static sources propagating along the z-axis separated along both coarse and fine axes are measured by

$$V_s(\vec{x}, z) = \log\left(\frac{W_{ss}(\vec{x}, z)}{W_{ss}(\vec{x}, z+1)}\right), \quad V_t(t, z) = \log\left(\frac{W_{ts}(t, z)}{W_{ts}(t, z+1)}\right), \tag{1.35}$$

letting $z \to \infty$ (here $W_{ss}(\vec{x}, t)$ are spatial Wilson loops and $W_{ts}(t, z)$ are loops using the fine direction).

Since the UV divergences due to the static sources are the same and for a physical distance r we have $|\vec{x}| = t = r$ we can set $\vec{x} = na_s$ and $t = nma_t$ and tune ξ such that the ratio

$$\rho_n = \frac{a_s V_s(na_s)}{a_s V_t(mna_s)} \equiv 1, \tag{1.36}$$

which implies the anisotropy $\xi_R = m$.

An alternative method for determining ξ_R is the use of the dispersion relation for the torelon. This state will be described in detailed in the next chapter, but for the moment it will be enough to say that it is a Polyakov line that loops around the lattice in one direction, eg. $\hat{z}$.

$$L_z(p, t) = \sum_{x,y} L_z(x, y, t)e^{i(p_x x + p_y y)}, \tag{1.37}$$

where

$$L_z(x, y, t) = \text{Tr } \Pi_{k=1}^{L_s} U_z(\vec{x} + k\hat{z}, t). \tag{1.38}$$

It is constructed from links which are smeared in a manner to be described in the

18

next chapter and its correlation function is evaluated for various choices of momentum $\mathbf{p} = (p_x, p_y) = (n_x, n_y)(2\pi/L_s a_s)$ where L_s is the lattice extent in the x and y directions. We thus measure

$$C(\mathbf{p}, t) = c(\mathbf{p})e^{-E(\mathbf{p})t/a_t}, \tag{1.39}$$

$$E(\mathbf{p})a_t = \frac{a_s\sqrt{\mathbf{p}^2 + M_T^2}}{\xi_R}, \tag{1.40}$$

where M_T is the torelon mass and from eq. (1.40) we can easily obtain ξ_R. In Chapter 2 we present an example of a torelon dispersion relation for a $12^2 \times 6 \times 48$ lattice.

Free parameter ω

As we mentioned in the previous section ω must be chosen to be greater than zero so that the approach to the QCD continuum is made on a trajectory far away from the critical endpoint in the plane of fundamental-adjoint couplings ($\beta_A = 0$, which implies $\omega > 0$) also the physical quantities should be independent of it. It has been confirmed in Ref. [16] that once the input is set beyond $\omega = 1$ there is little dependence of physical mass ratios on the precise value of the parameter and thus no fine tuning is required to reproduce continuum results.

1.8   Setting the energy scale

In order to convert quantities measured with lattice simulations into physical units the energy scale must be set by determining the lattice spacing a_t for each β and ξ. An experimentally well known quantity is chosen and then measured on the lattice in terms of a_t. The hadronic scale parameter r_0 defined in terms of the force between static quarks by $[r^2 dV(\vec{r})/dr]_{r=r_0} = 1.65$, where $V(\vec{r})$ is the static quark potential, is

19

an attractive possibility since it can be measured very accurately both experimentally (where $r_0^{-1} \approx 410$ MeV) and on the lattice [17, 22]. In fact on the lattice the values of the potential $V(\vec{r})$ were extracted as usual from the Wilson loop for each $\vec{r}$. The potential so found fit the form $V(\vec{r}) = e_c/r + \sigma r + V_0$ very well. The fit parameters e_c, σ and V_0 are then used to extract the ratio

$$r_0/a_s = \sqrt{(1.65 + e_c)/\sigma a_s^2}. \tag{1.41}$$

1.9 Comments and comparisons with the literature

In this chapter we gave a brief introduction to the construction of the anisotropic lattice action of eq. (1.34) proposed by C. Morningstar and M. Peardon in Refs. [16, 29]. We adopted an anisotropic action in our calculation of the QCD periodic flux tube spectrum (to be presented in the next chapter) since the use of anisotropic lattices proved to be essential in the calculation of the glueball spectrum (see Ref. [19]). It is also important to realize that due to the enormous effort required by lattice QCD simulations, one is restricted to rather coarse lattice spacings and therefore it is vital to choose the lattice action such that already at a coarse lattice spacing the lattice artefacts are small. The action of eq. (1.34) is constructed using the Symanzik scheme that allows the systematic elimination of lattice artefacts, order by order in the lattice spacing and the coupling constant. For SU(3) isotropic lattice gauge theory a complete Symanzik method has been worked out by Lüscher and Weisz [5], up to the 1-loop level in perturbation theory, to eliminate the $O(a_s^2, a_t^2)$ corrections. The action of eq. (1.34) does not include counterterms which would eliminate the $O(a_t^2)$ errors. In fact it was noticed that these terms introduce spurious high energy modes that have detrimental effects on the correlation functions. Also, the action of eq.

(1.34) is improved only at tree level, but, since we work at rather large values of the gauge-coupling, it is not clear a priori, whether a 1-loop improvement is of any help. To clarify this question we refer the reader to Ref. [34] where studies of the scaling behavior of various quantities have been considered. The introduction of an adjoint part in the action of eq. (1.34) with a negative value for β_A was considered in order to stay away from the SU(3) first order phase transition line. As already explained in Sec. 1.6 at the end-point of this SU(3) first order phase transition (see Ref. [28]) lattice artefacts might completely disguise the continuum physics. A recent study investigating whether corrections to scaling can be reduced by using a negative value of the adjoint coupling is presented in Ref. [35].

Chapter 2

QCD Spectrum

2.1 Introduction

It is widely believed that QCD is linearly confining and that this explains why we do not observe quarks or gluons in nature. The chromo field distribution between static quarks in $SU(2)$ was computed in Ref [32] on lattices with physical extent ranging from 1.3 fm up to 2.7 fm. The energy flux profile suggested that gluon field forms a string-like object over physical distances as large as 2 fm. Innumerable lattice QCD simulations [33] have also confirmed that the energy of the ground state rises linearly with the separation between the quark and antiquark, naively suggesting that the gluon field forms a string-like object connecting the quark and the antiquark. However, Juge, Kuti and Morningstar in Ref. [37] stressed the fact that the spherical bag model also predicts a linearly rising energy and hence the linearly rising ground-state energy is not conclusive evidence of string formation. We, thus, adopted the viewpoint of Juge, Kuti and Morningstar that the relevant properties of the confining gluon field are best revealed in its excitation spectrum. They reported in a series of studies [36, 37, 38, 39, 40, 41, 42] a comprehensive lattice determination of the excited gluon field between a static quark-antiquark pair.

A particularly favorable theoretical environment in which to observe the onset of

string behavior is provided by the analysis of the spectrum of a QCD periodic flux tube due to the absence of fixed color sources.

2.2   How to calculate the energy spectrum

The starting point is the observation that

$$C(t) = \langle \phi^\dagger(t)\phi(0) \rangle = \sum_n |\langle \text{vac}|\phi|n \rangle|^2 e^{-E_n t} \rightarrow |\langle \text{vac}|\phi|0 \rangle|^2 e^{-E_0 t}, \qquad (2.1)$$

where $|0\rangle$ is the lightest state that couples to the operator ϕ and E_0 is its energy.

However, because the correlation function of eq (2.1) is decreasing exponentially in t, it will, at large t, disappear into statistical noise. It is very important, then, to obtain the asymptotic behavior of the correlator as quickly as possible. In order to do so we choose operators for which the overlap with the lightest state is as large as possible using smearing and variational methods. Also the use of an anisotropic lattice, described in the previous chapter, in which the temporal spacing a_t is much smaller than that in the spatial direction a_s, enables us to exploit the enhanced signal-to-noise of the correlation function at smaller temporal separations.

So if we want the energy spectrum of a flux tube that winds once around one direction, we have to use the following strategy:

- identify the symmetries of this particular problem

- construct an operator with the quantum numbers of the desired symmetries

- employ smearing and variational techniques to find the operator that best overlaps the state with the quantum numbers desired.

2.3 Symmetries of the problem

On a torus, a global $\mathbb{Z}_3$ symmetry is associated with each compactified space-time direction, μ. In particular, multiplying all links in one direction by z, a non-trivial element of $\mathbb{Z}_3$, the center of the group $SU(3)$,

$$U_\nu(x) \rightarrow U_\nu(x)^z = \begin{cases} z\, U_\nu(x) & \text{for } x_\mu = 0 \text{ and } \nu = \mu, \\ U_\nu(x) & \text{otherwise,} \end{cases} \tag{2.2}$$

leaves the Haar integration measure dU_l and the plaquette action invariant. In fact in a contractible loop, such as a plaquette, any factor of z from a forward going link is necessarily cancelled by a corresponding factor $z^\dagger$ from a backward going link. One of the simplest objects that is sensitive to the center symmetry is a Wilson line that encircles a spatial lattice direction, $\hat{\imath}$:

$$L_i(t) = \text{Tr } \Pi_{k=1}^{L_s} U_i(\vec{x} + k\hat{\imath}, t). \tag{2.3}$$

From its correlation function

$$\langle ReL_i(t)\, ReL_i(0) \rangle \approx e^{-E_T t} \quad \text{for } t \rightarrow 0, \tag{2.4}$$

the energy of the "torelon" can be extracted, a state that exists only on a torus and that corresponds to a color flux tube wrapping around a periodic boundary. In contrast to the plaquette, the Wilson line will acquire just a single factor z

$$L_i(t) \rightarrow z\, L_i(t). \tag{2.5}$$

The transformation property of the Wilson line under the center symmetry implies that [7, 50]

1. $\langle L_i(t) \rangle = \sum_{z \in \mathbb{Z}(3)} z\, \langle L_i(t) \rangle = 0,$

24

2. $\langle L_i(t)\ L_i(0)\rangle = \sum_{z\in\mathbb{Z}(3)} z^2\ \langle L_i(t)\ L_i(0)\rangle = 0 =$

    $= \langle ReL_i(t)\ ReL_i(0)\rangle - \langle ImL_i(t)\ ImL_i(0)\rangle$ [1],

3. $\langle ReL_i(t)\ ReL_j(0)\rangle = 0$ for $i \neq j$.

The first property is directly related to confinement. Recalling that confinement can be identified as the phase in which global center symmetry is also a symmetry of the vacuum [44], the vacuum expectation value of a torelon can be regarded as a true order parameter: zero in one phase and non-zero in another, which associates the breaking of a global symmetry with the transition from one phase to the other.

$$\langle L_i(t)\rangle = 0 \Leftrightarrow \text{unbroken } \mathbb{Z}_3 \text{ symmetry} \Leftrightarrow \text{confinement phase.}$$

An analogy with the Polyakov loop, a loop that winds around the temporal direction, would also disclose the physical implications of a non-zero vacuum expectation value of the torelon, in particular the breaking of the flux tube [45]. The last two properties are useful in the determination of the symmetries that we have to consider when calculating the energy spectrum of a flux tube. For instance, property 2 implies

$$\frac{1}{2}\langle L_i^\dagger(t)\ L_i(0)\rangle = \langle ReL_i(t)\ ReL_i(0)\rangle = \langle ImL_i(t)\ ImL_i(0)\rangle, \qquad (2.6)$$

and so torelon states are degenerate with respect to charge conjugation since under charge conjugation the trace of an ordered product of link matrices will go to its complex conjugate: so the real part is $C = +$ and the imaginary part is $C = -$,

$$L_i(t) \xrightarrow{C} L_i^\dagger(t),$$

$$Re\ L_i(t) \xrightarrow{C} Re\ L_i(t),$$

$$Im\ L_i(t) \xrightarrow{C} -Im\ L_i(t).$$

---

[1] Here the imaginary part $i\langle ReL_i(t)\ ImL_i(0)\rangle + \langle ImL_i(t)\ ReL_i(0)\rangle$ vanishes by charge invariance.

Property 3 tells us that the overlap of torelons winding around orthogonal spatial directions is zero, thus nothing is to be gained by producing linear combinations that transform according to irreducible representations of the rotation group O_h [50]. To clarify this point it is helpful to describe in detail how torelon states are constructed (for a review applied to glueballs see Refs. [46, 47]). The gauge invariant operator in eq. (2.3) is the simplest torelon operator that can be constructed on the lattice. It is clear, however, that it transforms trivially under translations on the winding axis and under rotations and reflections on the plane perpendicular to the winding axis. Thus more complex operators need to be considered to obtain the excited states of the flux tube. In order to do so, consider the trace of a product of link matrices around an arbitrary closed loop C that encircles a winding direction and call it τ_C:

$$\tau_C = \text{Tr } \Pi_{l \in C} U_l. \tag{2.7}$$

It is clear that properties (1)-(3) equally apply to this operator, for any shape C. In order to construct states with the right quantum numbers we assume that the continuum limit of $SU(3)$ lattice gauge theory exists. The states to be considered are then described by the irreducible representations of $SO(3) \otimes \mathbb{Z}_2 \otimes \mathbb{Z}_2$ where $\mathbb{Z}_2$ are the two discrete symmetries: the total space reflection and the charge conjugation. In addition we want to consider states with definite momentum. Call the symmetry group of interest $G = SO(3) \otimes \mathbb{Z}_2 \otimes \mathbb{Z}_2 \otimes \mathcal{I}$, where $\mathcal{I}$ is the translation group, and $T(\theta)C$ the shape obtained by applying the transformation $T \in G$ on C. Torelon operators that transform irreducibly under an irreducible representation of the group G can be built by taking an appropriate linear combination:

$$\phi^{(R)}(t) = \sum_{\vec{x}} e^{i\vec{p}\cdot\vec{x}} \sum_{T \in G_p} a^{(R)} \text{Tr } U_{T(\theta)C}. \tag{2.8}$$

The coefficients $a^{(R)}$ depend on the irreducible representation R of the little group

G_p, and the factor $e^{i\vec{p}\cdot\vec{x}}$ has been included to obtain operators with non-zero momentum $\vec{p}$. Applying the torelon operator of eq. (2.8) to the vacuum will create a state with momentum $\vec{p}$ and quantum numbers that correspond to the irreducible representation R of the group G_p. As described above, the center symmetry of the lagrangian allows us to restrict our torelon operators to be positive under charge conjugation and therefore only the real part of the trace will be considered in eq. (2.8). If we consider operators with non-zero momentum along the $\hat{z}$-axis, p_z, the little group G_p consists of rotations on the plane perpendicular to the $\hat{z}$-axis and of the $\mathbb{Z}_2(\mathcal{P})$ parity reflection that reflects operators in one coordinate axis on the $z = 0$ plane, $\mathcal{P} : (x, y) \rightarrow (x, -y)$. Operators with zero momentum are described by the irreducible representations of $SO(3) \otimes \mathbb{Z}_2$. However, because the overlap between torelons winding in orthogonal directions is zero, we can reduce this symmetry group to rotations on the plane perpendicular to one winding direction $\hat{z}$, to the $\mathbb{Z}_2(\mathcal{P})$ and to the $\mathbb{Z}_2(\mathcal{R})$ that reflects operators about the midpoint on the winding axis. Summarizing, the representations to be considered are the ones that correspond to the following group:

$$
G^{\text{cont.}} = \begin{cases} SO(2) \otimes \mathbb{Z}_2(\mathcal{P}) \otimes \mathbb{Z}_2(\mathcal{R}) & \text{for } \vec{p} = 0, \\[2em] SO(2) \otimes \mathbb{Z}_2(\mathcal{P}) & \text{for } p_z \neq 0 \ \ p_x = p_y = 0. \end{cases}
\tag{2.9}
$$

On the lattice this symmetry group is broken to the point group $C_{4v} \otimes \mathbb{Z}_2(\mathcal{R})$ for $p_z = 0$ and C_{4v} for $p_z \neq 0$. C_{4v} contains rotations of $\frac{\pi}{2}$ and the reflection in the xy plane ($\mathcal{P}$-parity) and has five irreducible representations: A_1, A_2, B_1, B_2, E. $\mathbb{Z}_2(\mathcal{R})$ denotes the two-element group consisting of the identity operation and the reflection about the midpoint on the winding axis z. States that are even/odd under $\mathcal{R}$-parity are labeled by the subscripts g/u respectively. The irreducible representations of C_{4v} and the corresponding coefficients a^R in the linear combinations

27

$$\phi_i^{(R)}(t) = \begin{cases} \sum_{x,y,z} \sum_{T \in C_{4v}} a^{(R)} \mathrm{ReTr}(U_{T(\theta)C_i} \pm U_{\mathcal{R}T(\theta)C_i}) & \text{for } \vec{p} = 0, \\ \\ \sum_{x,y,z} e^{ip_z z} \sum_{T \in C_{4v}} a^{(R)} \mathrm{ReTr} U_{T(\theta)C_i} & \text{for } p_z \neq 0, \end{cases} \tag{2.10}$$

are described in detail in Appendix A. The index i is introduced, here, because the closed loop C_i used to build torelon states in eq. (2.10) can take any shape. We constructed fifteen different shapes and from each one we built a basis for each irreducible representation of C_{4v} using the character projection operator as described in detail in Appendix A. In Fig 2-1 we present the shapes used and in Table 2.1 we summarize the irreducible contents for each shape, C_i.
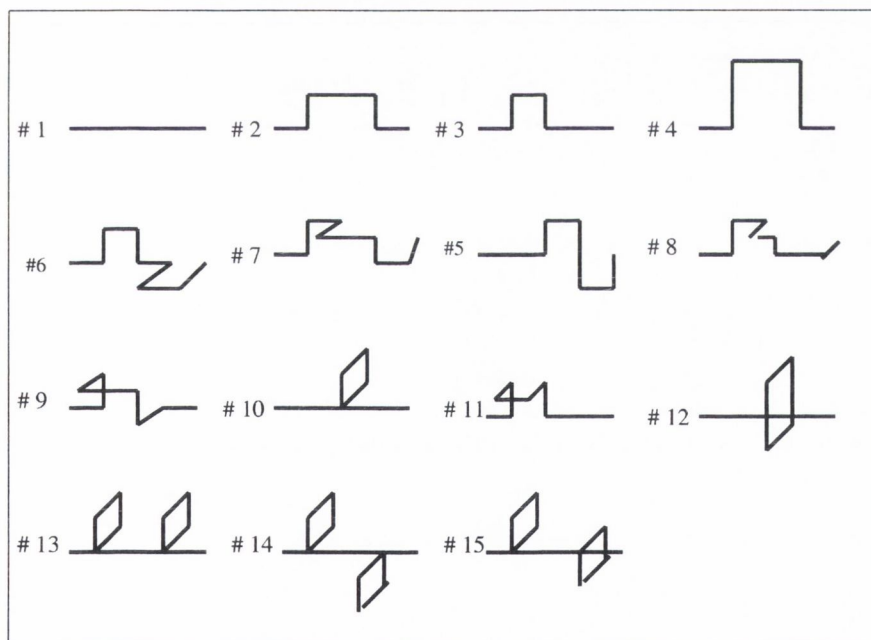
Figure 2-1: The fifteen prototype lattice paths used in the construction of torelon operators

It is worth making a comment on the $\mathcal{P}$-parity, $\mathcal{P} : (x, y) \to (x, -y)$ (see Ref [47]). The fact that the angular momentum operator $x\partial_y - y\partial_x$ flips sign under parity has important consequences for the spectrum. In the continuum, states that transform irreducibly under $SO(2) \otimes \mathbb{Z}_2(\mathcal{P})$ are built as $|j, \pm\rangle = |j\rangle \pm \mathcal{P}|j\rangle$ where $|j\rangle$ is some

state with angular momentum j and energy E_j. As long as $j \neq 0$ these two states cannot be null since $|j\rangle$ and $\mathcal{P}|j\rangle$ are orthogonal to each other and also they are degenerate since $\mathcal{P}$ commutes with the Hamiltonian. This argument clearly fails for $j = 0$, thus in the continuum we expect parity doubling for states with $j \neq 0$. On the lattice $SO(2)$ is broken to C_4 and as explained in Appendix A the states that transform irreducibly under the j representation also transform irreducibly under representations with $j' = j \pm 4k$ for $k = 0, \pm 1, \pm 2, \ldots$

shape [1]	$A_{1g}(0)$	$E(1)$	$B_{1g}(0)$	$B_{2g}(0)$	$A_{2u}(0)$	$A_1(2)$	$B_1(2)$	$B_2(2)$	$E(2)$	$A_1(1)$	$A_2(1)$	$B_1(1)$	$B_2(1)$
#1	1	0	0	0	0	0	0	0	0	0	0	0	0
#2	1	1	1	0	0	1	1	0	0	0	0	0	0
#3	1	1	1	0	0	1	1	0	1	1	0	1	0
#4	1	1	1	0	0	1	1	0	0	0	0	0	0
#5	1	1	1	0	0	1	1	0	1	1	0	1	0
#6	1	1	0	1	0	1	0	1	1	0	1	1	0
#7	1	1	0	0	1	0	1	1	0	0	0	0	0
#8	1	1	1	1	1	1	1	1	1	1	1	1	1
#9	1	1	0	1	1	1	1	1	0	0	0	0	0
#10	1	1	0	1	1	1	1	1	1	1	1	1	1
#11	1	1	1	1	0	1	1	1	1	1	1	1	1
#12	1	1	1	0	1	1	1	1	1	1	1	1	1
#13	1	0	0	1	1	1	1	1	1	0	0	0	0
#14	1	1	0	1	0	1	0	1	1	0	1	1	0
#15	1	1	1	0	0	1	1	0	0	0	1	0	1
$d^{(R)}$ [2]	15	13	8	7	6	13	12	9	9	6	7	8	5

[1] The notation is to be read as first letter corresponds to the irreducible representation of $C_{4v} \times \mathcal{R}$ and the number in parenthesis represents the momentum along the winding axis.
[2] $d^{(R)}$ is the number of shapes that projects on the representation R.

Table 2.1: Irreducible contents of the representations of C_{4v} on the different loop shapes.

Thus on the lattice there is no reason to expect parity doubling for $j = 2$, any more than for $j = 0$, although we should continue to observe parity doubling for the $1^\pm$ states. Obviously once the continuum limit is reached by taking the lattice spacing to zero and the volume to infinity we should also be able to recover parity doubling for the $2^\pm$ states.

2.4 Smearing operators

As already pointed out, the signal-to-noise ratio in the determination of the correlation function, $C(t) = \langle \phi^{\dagger(R)}(t) \, \phi^{(R)}(0) \rangle$ falls exponentially fast with respect to t. Thus it is crucial to use operators for which the overlap $\langle \mathrm{vac}|\phi^{(R)}|0\rangle$ is as large as possible, that it is to say we want operators that are close to the wave-function of the state in question. In Ref [51], M. Teper showed, in a study on glueballs, that the mismatch between $\phi|\mathrm{vac}\rangle$ and the physical ground-state wave function $|0\rangle$ increases rapidly as the lattice spacing goes to zero. This is intuitively obvious since the physical extension of the state remains fixed while the operator ϕ probes an ever smaller region as one decreases the lattice spacing. A crucial ingredient in constructing operators ϕ that possess the extended structure of the physical state is the link variable smearing. The smeared link is a combination of the original link and the spatial staples surrounding it

$$U_\mu^{(1)}(x) = U_\mu^{(0)}(x) + \sum_{\nu \neq \mu} \rho_{\mu\nu} C_\nu^{(0)}(x), \tag{2.11}$$

with

$$C_\mu^{(0)}(x) = U_\nu^{(0)}(x)U_\mu^{(0)}(x+\hat\nu)U_\nu^{\dagger(0)}(x+\hat\mu)+U_\nu^{\dagger(0)}(x-\hat\nu)U_\mu^{(0)}(x-\hat\nu)U_\nu^{(0)}(x-\hat\nu+\hat\mu), \tag{2.12}$$

where $\rho_{\mu\nu}$ is a free parameter and is usually chosen such that $\rho_{\mu\nu} = \rho$. The smeared link is then projected back onto the gauge group: $U_\mu^{(1)}(x) = \mathcal{P}_{SU(3)}\{U_\mu^{(0)}(x)+C_\mu^{(0)}(x)\}$. The process can be iterated n-times and one then constructs from these smeared links $U_\mu^{(n)}$ the operators $\phi_i^{(R)}$ described in the previous section.

In our calculations we used a new analytic smearing of the $SU(3)$ links proposed by C. Morningstar and M. Peardon [53]. Noting that the matrix $Q_\mu(x)$, defined by

$$Q_\mu(x) = \frac{i}{2}(\Omega_\mu^\dagger(x) - \Omega_\mu(x)) - \frac{i}{2N}Tr(\Omega_\mu^\dagger(x) - \Omega_\mu(x)), \qquad (2.13)$$

where

$$\Omega_\mu(x) = C_\mu(x)U_\mu^\dagger(x), \qquad (2.14)$$

is Hermitian and traceless, and hence, $e^{iQ_\mu(x)}$ is an element of $SU(3)$, they defined an iterative, analytic link smearing algorithm in which the links $U_\mu^{(n)}(x)$ at step n are mapped into links $U_\mu^{(n+1)}(x)$ using

$$U_\mu^{(n+1)}(x) = e^{iQ_\mu(x)}U_\mu^{(n)}(x). \qquad (2.15)$$

The implementation of $e^{iQ_\mu(x)}$ is done in an efficient way as described in Ref [53]. Our operators $\phi_i^{(R)}(x)$ are then constructed as in eq. (2.10) using these stout, smeared links instead of the simple $U_\mu(x)$.

In particular, we used two different smeared links: one obtained from $U_\mu(x)$ after 6 iterations with $\rho = 0.12$ and the other obtained from $U_\mu(x)$ after 12 iterations with the same value of ρ. The two levels of smearing, combined with the fifteen shapes of Fig 2-1, give us a large basis of operators to which we apply variational methods. The dimension of this basis for each representation is $N^{(R)} = 2d^{(R)}$ where $d^{(R)}$, presented in the last row of Table 2.1, is the number of shapes that project on one particular irreducible representation, R.

2.5   Implementation details

The evaluation of the torelon operators of eq. (2.10) is done in two steps using two different C programs. The first program chooses some initial paths C_i (see Fig. 2-1) and represents them in some graphical representation, i.e. (z,x,z,z,-x,z). These initial paths are chosen to be combinations of some "basic operators". These basic operators

31

could be straight lines, i.e. (z,...) with NZlink steps in the z-direction (similarly for other directions) and angles, i.e (z..,x...) with NZlink steps in the z-direction and NXlink steps in the x-direction (and similarly for the other directions). The use of these "basic operators" reduces the computational cost during the evaluation of the trace of links around the paths [2]. The operations of the group of interest $K = G \otimes \mathcal{I}$ (where G is the group of rotations and reflections as given in eq. (2.9) and $\mathcal{I}$ are the translations on the z-axis) are then applied on the initial paths. Of the resulting paths TC_i (where $T \in K$) only those that differ with respect to each other are kept, reducing greatly the computational cost in the evaluation of sums of eq. (2.10). These paths are then labeled according to the group operation $T \in K$ that was performed. From the character table presented in Appendix A, it is then straightforward to get the coefficient in each irreducible representation that must be assigned to each transformed path TC_i in the sum of eq. (2.10). The second program performs the product of links along all the paths TC_i generated by the first program in terms of the "basic operators" and multiplies their trace by the corresponding coefficients. Before evaluating the correlators we performed several checks. In particular we checked if the torelon operators were gauge invariant and also if they transformed according to the irreducible representation under consideration. The last check was done by applying the same group operations $T \in K$ (translations and rotations) on the lattice and evaluating the torelon operators on these transformed lattices. These values were then compared with the torelon operators of the untransformed lattice to check if they transformed irreducibly under the representation of interest.

---

[2] As a simple example, choosing among the basic operators the following: #1 = (z,x), #2 = (z,z) and #3 = (-x,z), an original path of the form (z,x,z,z,-x,z) can be re-expressed as (#1,#2,#3), which halves the number of operations to be performed in the evaluation of the trace.

2.6 Analysis details

From the large basis of operators constructed in the previous sections we form the best operator $\boldsymbol{\Phi}^{(R)}(t)$ as a linear combination of the basis operators

$$\boldsymbol{\Phi}^{(R)}(t) = \sum_{i=1}^{N^{(R)}} v_i^{(R)} \phi_i^{(R)}(t). \tag{2.16}$$

The coefficients $v_i^{(R)}$ are determined by maximizing the correlation function

$$C(t) = \frac{\langle \boldsymbol{\Phi}^{(R)\dagger}(t)\boldsymbol{\Phi}^{(R)}(0)\rangle}{\langle \boldsymbol{\Phi}^{(R)\dagger}(0)\boldsymbol{\Phi}^{(R)}(0)\rangle}. \tag{2.17}$$

The requirement $\frac{dC}{dv^{(R)}} = 0$ yields a generalized eigenvalue problem

$$\sum_{km} C_{jk}^{-1\,(R)}(0)C_{km}^{(R)}(t)v_m^{(R)}(t) = \lambda^{(R)}(t)v_j^{(R)}(t), \tag{2.18}$$

where C_{km} is the $N^{(R)} \times N^{(R)}$ correlation matrix

$$C_{km}^{(R)}(t) = \sum_{\tau} \langle \phi_k^{(R)\dagger}(\tau + t)\phi_m^{(R)}(\tau)\rangle. \tag{2.19}$$

In common with most implementations, the eigenvectors are calculated with normalization

$$\sum_{km} v_k^{(R)}(t)C_{km}^{(R)}(t)v_m^{(R)}(t) = 1, \tag{2.20}$$

at $t = 1$ and then frozen at all subsequent times. The eigenvector $v_0^{(R)}$ corresponding the largest eigenvalue $\lambda^{(R)}$ then yields the coefficients for the operator $\Phi_0^{(R)}(t) = \sum_{i=1}^{N^{(R)}} v_0^{(R)} \phi_i^{(R)}(t)$ which best overlaps the lowest lying torelon state $|0\rangle$ in the representation R of interest. Operators which overlap excited states can also be constructed using other eigenvectors of eq (2.18). In Fig 2-2 we present the lowest and the first exited energies for the channel $A_{1g}(0)$ obtained using the method de-

scribed above. Information about the composition of $\mathbf{\Phi}_n$ in terms of the operators used in the simulation is obtained from the overlap $\langle \mathbf{\Phi_n}^\dagger \phi_i \rangle = \sum_j C_{ij}(0) v_{nj}^{(R)}$.

In the limit where the basis $\{\phi_i\}$ is complete this procedure becomes exact [54]. This means that we can extract the energy of the lightest state, with the quantum numbers of the irreducible representation R, directly from the correlation function at any time t,

$$C(t) = \langle \mathbf{\Phi}^\dagger(t) \mathbf{\Phi}(0) \rangle = \langle \mathbf{\Phi}^\dagger(0) e^{-Et} \mathbf{\Phi}(0) \rangle = e^{-E_0 t}. \tag{2.21}$$
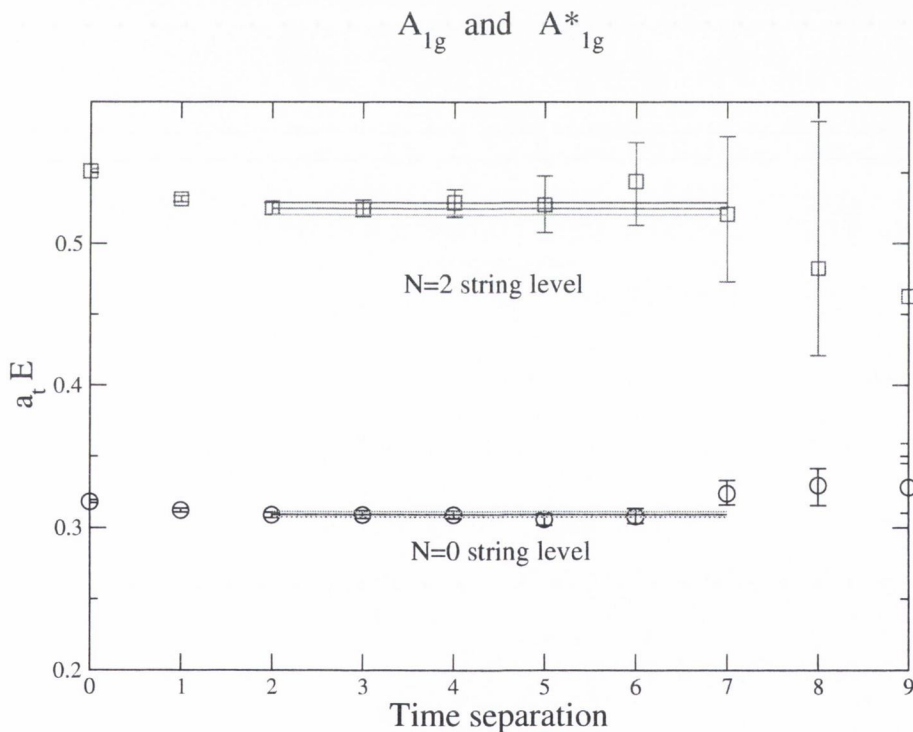
Figure 2-2: Lowest and first excited state for the channel $A_{1g}(0)$ for a $8^3 \times 48$ lattice with $\beta = 2.0$. 500 bins (10 configurations per bin) have been used.

In practice, however, we have a limited basis and eq. (2.21) gives us at best just an upper bound estimate for the energy E_0. We can improve this estimate by calculating $C(t)$ at all times t. For each time then we define an effective energy by

$$\langle \boldsymbol{\Phi}^{\dagger}(t)\boldsymbol{\Phi}(0)\rangle = \langle \boldsymbol{\Phi}^{\dagger}(0)e^{-Ht}\boldsymbol{\Phi}(0)\rangle = e^{-E_{\text{eff}}(t)t}, \tag{2.22}$$

and we know that E_{eff} will approach E_0 from above as t increases. The better our choice of basis operators, the smaller the value of t at which this occurs. Again, if our basis was complete then $E_{\text{eff}}(t) = E_0$ for all t. So we can estimate the value of E_0 from the value of $E_{\text{eff}}(t)$ on its plateau. In practice, what we actually do is to fit the correlation function to an exponential in t over a finite interval $[t_1, t_2]$ such that

$$\langle \boldsymbol{\Phi}^{\dagger}(t)\boldsymbol{\Phi}(0)\rangle = A\left(e^{-Et} + e^{-E(T-t)}\right), \tag{2.23}$$

where T denotes the extent of the lattice in the time direction [3]. From the exponent we then obtain our estimate of the energy E_0 and from the amplitude of the exponential the normalized projection of our operator onto the lightest state, i.e. $|\langle \text{vac}|\boldsymbol{\Phi}^{(\text{R})}|0\rangle|^2$. Our choice of the fitting interval $[t_1, t_2]$ is guided by the plateaux observed in the effective mass and is constrained by the requirement that a reasonable $\chi^2/\text{d.o.f}$ should be obtained. Error estimates on the energy E and on the amplitude are obtained using a bootstrap procedure.

2.7 Numerical results

The elements of the correlator matrix given by eq. (2.19) were estimated using Monte Carlo methods. Different simulations were performed on the CMU Cluster [4]. The input parameters are summarized in Table 2.2.

The renormalized anisotropy is evaluated using the method described in Chapter 1, Sec. 1.7. In particular the torelon dispersion relation for a $12^2 \times 6 \times 48$ lattice has been evaluated from the correlation function of the simplest torelon (shape #1

---

[3] The second exponential has been included due to the periodic boundary conditions in the time direction for which we have $C(t) = C(T - t)$ as it is clear from eq. (2.19).

[4] The CPU resources of the Carnegie Mellon University Cluster were kindly made available by Prof. C. Morningstar.

β	ξ_0	u_s^4	Lattice	a_s/r_0	$a_s(\text{fm})$	# bins [1]
2.0^2	7.205	0.3817	$8 \times 8 \times 8 \times 48$	0.4332(11)	0.208(1)	2270
2.0^2	7.205	0.3817	$8 \times 8 \times 12 \times 48$	0.4332(11)	0.208(1)	2966
2.0^2	7.205	0.3817	$8 \times 8 \times 16 \times 48$	0.4332(11)	0.208(1)	6559
2.0^2	7.205	0.3817	$6 \times 6 \times 16 \times 48$	0.4332(11)	0.208(1)	6190
1.8^2	7.201	0.3436	$8 \times 8 \times 12 \times 48$	0.56306(75)	0.27	2966
2.0	7.205	0.3817	$8 \times 8 \times 8 \times 48$	0.4332(11)	0.208(1)	500
2.0	7.205	0.3817	$8 \times 8 \times 12 \times 48$	0.4332(11)	0.208(1)	2400
2.0	7.205	0.3817	$8 \times 8 \times 16 \times 48$	0.4332(11)	0.208(1)	2900
2.0	7.205	0.3817	$6 \times 6 \times 16 \times 48$	0.4332(11)	0.208(1)	2000
2.16	7.192	0.4080	$8 \times 8 \times 20 \times 48$	—	0.167	3200

[1]Each bin is the average of 10 measurements [2]Simulations done using only the first eight shapes

Table 2.2: Input parameters used in torelon simulations.

in Fig. 2-1) winding around the z direction. This torelon line is associated with a particular point in the (x, y)-plane and is constructed from links which are smeared in a manner described in Sec. 2.4. Recall, eq. (1.37)

$$L_z(p,t) = \sum_{x,y} L_z(x,y,t)e^{i(p_x x + p_y y)}, \qquad (2.24)$$

where

$$L_z(x,y,t) = \text{Tr } \Pi_{k=1}^{L_s} U_z(\vec{x} + k\hat{z}, t). \qquad (2.25)$$

Eight smearing levels have been applied for this purpose and the outcome is presented in Fig. 2-3. The highest momentum used in the fit is $(p_x, p_y) = (1, 1)$ to give the renormalized anisotropy of $\xi = 6.16(11)$ for the simulation with $\beta = 2.0$ and $\xi = 6.08(17)$ for $\beta = 2.16$.

In the simulations presented in Table 2.2 which have been used to evaluate the QCD flux spectrum, five sweeps were performed between measurements and the measurements were averaged into bins of 10 in order to reduce data storage requirements. In all simulations, the number of bins goes from 500 to 6500 depending on the size of the lattice used. The first five simulations were done using only the first eight

36

Torelon dispersion on 12^2x6x48
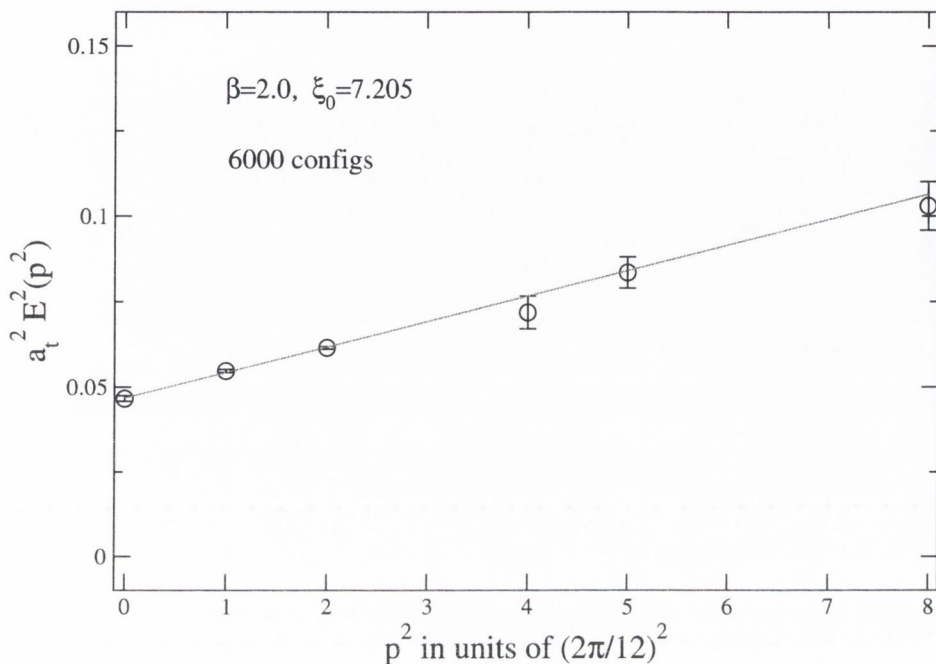
Figure 2-3: Plot of $E(\mathbf{p}^2)$ versus $\mathbf{p}^2$ on $12^2 \times 6 \times 48$ lattice. The line shows the fit to $E(\mathbf{p}^2) = A + B\mathbf{p}^2$.

shapes given in Fig. 2-1. The results were presented at the Lattice03 conference in Japan [43]. However, the decay into noise of the $A_2(1)$ plateau and the ambiguity in the determination of the energy of the $B_2(1)$, $B_{2g}(0)$, $A_{2u}(0)$ states made us think that the basis of operators could have been improved. In Fig 2-4 we display the overlaps $\langle \Phi^\dagger \phi_i \rangle$ (for the shorter simulation, with $\beta = 2.0$) for these states, in a way similar to Ref. [50]. These plots give information about the composition of the "best" operator Φ for these states and they clearly show that the use of the pool with 15 shapes will improve their energy determinations. For example, considering the A_{2u} state in Fig. 2-4, we see that the contributions of the basic operators ϕ_{11} and ϕ_{12} are more important than the contributions of the basic operators ϕ_6 and ϕ_7. This fact explains why the energy determination of this state is poor when using only the first eight shapes. In general, the energy determinations of all states using the whole pool of operators has improved in those cases where it was poor and agrees in the

cases where there was no ambiguity, already using eight shapes. The results of fitting the variationally-optimized correlators $C(t)$ to the function given in eq. (2.23) are summarized in Tables 2.5-2.8. We also included a two-exponential fit, according to the function,

$$\langle \mathbf{\Phi}^\dagger(t)\mathbf{\Phi}(0)\rangle = A\left(e^{-Et} + e^{-E(T-t)}\right) + B\left(e^{-E't} + e^{-E'(T-t)}\right), \qquad (2.26)$$

in order to check if there were contaminations to the ground-state from excited states[5]. We found that the results obtained using eq. (2.26) are consistent with the one-exponential fit, showing that our operators overlap well with the ground-states in each channel. Some examples of the effective energy plots are presented at the end of the chapter in Figs 2-5,..,2-12. For each channel in each simulation done using fifteen operators, it was possible to find a fit region $[t_1, t_2]$ in which the correlation function was well described by its asymptotic form as indicated by the quality of the fit. Convincing plateau, which span a minimum of three time-slices or more, were observed in all effective energies. The overlaps with the lowest-lying states were also found to be good, better than 90% in most cases. This clearly demonstrates the effectiveness of the link-smearing and variational techniques in diminishing excited-state contamination. Our best estimates for the torelon energies in terms of a_t^{-1} are summarized in each of the Tables 2.5-2.9.

---

[5]I would like to acknowledge Dr. Sinead Ryan for providing me with the analysis-code used to fit our data to eqs. (2.23) and (2.26)
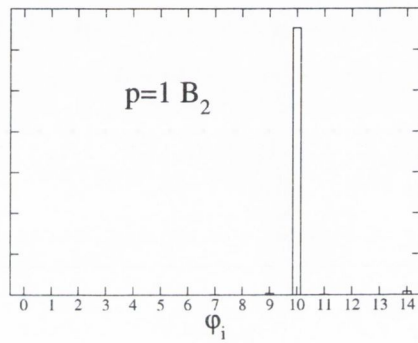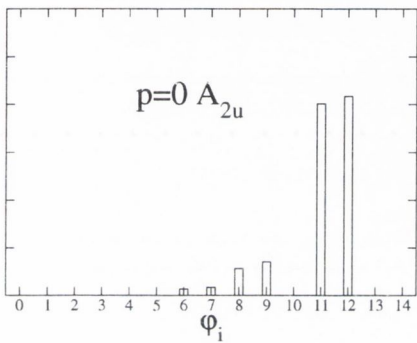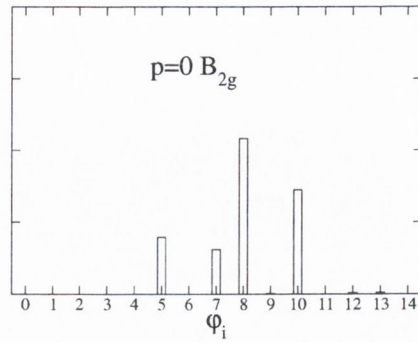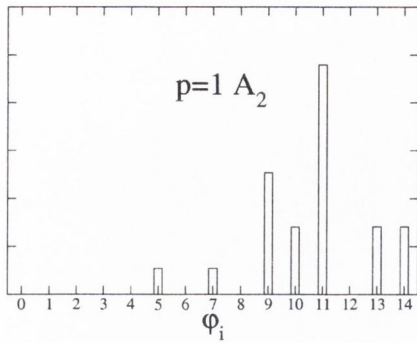
Figure 2-4: Overlaps $\langle \Phi^\dagger \phi_n \rangle = \sum_j C_{ij}(0) v_{nj}^{(R)}$ that show the relative contributions to the "best" operator in the variational method. (See Sec. 2.7 in the text for more details.)

2.8 Finite volume and spacing effects

In this section we want to evaluate the magnitude of the discretization errors in the torelon energy determinations. One source of uncertainty could be the finite volume. The energies of torelons confined in a finite box with periodic boundary conditions also in the directions perpendicular to the winding flux can differ appreciably from their infinite volume values. Finite volume effects can also induce a splitting in the B_1 and B_2 energies as pointed out in Section 2.3. In order to check the effects of simulating in a finite volume, we performed an extra simulation using a lattice of different spatial extent in the direction perpendicular to the winding axis. The temporal extent was held fixed at 48 grid points (2 fm). The results from the $6^2 \times 16$ lattice differ very little from the $8^2 \times 16$ in most cases, suggesting that our lattice volumes are sufficiently large to ensure that finite volume errors are negligible, at least for the QCD flux lengths considered in our studies. The results are presented in Table 2.3.

Channel	$L_{\parallel}/a_s = 6$	$L_{\parallel}/a_s = 8$
$p = 0$ A_{1g}	0.651(2)	0.649(4)
$p = 1$ E	0.733(1)	0.729(3)
$p = 0$ A_{1g}^*	0.794(4)	0.797(3)
$p = 0$ A_{2u}	0.788(4)	0.791(7)
$p = 0$ B_{1g}	0.801(4)	0.797(3)
$p = 0$ B_{2g}	0.780(9)	0.796(3)
$p = 2$ A_1	0.813(7)	0.804(6)
$p = 2$ B_1	0.813(7)	0.805(7)
$p = 2$ B_2	0.808(3)	0.805(6)
$p = 2$ E	0.807(2)	0.805(4)
$p = 1$ A_1	0.862(3)	0.864(3)
$p = 1$ A_2	0.826(8)	0.840(3)
$p = 1$ B_1	0.867(3)	0.869(3)
$p = 1$ B_2	0.863(9)	0.886(8)

Table 2.3: Energy estimates in terms of a_t^{-1} for $\beta = 2.0$ and various lattice volumes, where $L_{\parallel}$ is the lattice extent in the directions perpendicular to the flux tube.

In order to quantify finite lattice spacing artefacts we should evaluate the QCD flux spectrum at a fixed physical volume with different lattice spacings. The reason why we need to keep the physical volume fixed is clarified in the next Chapter, but for the moment it is enough to say that this is the only clean way to disentangle the spacing artefacts from the physical energy dependence on the length of the QCD flux tube, as predicted by an effective string theory. In particular, assuming that the $L_z = 16$ simulation at $\beta = 2.0$ and the $L_z = 20$ simulation at $\beta = 2.16$ have exactly the same physical volume, $a_s \times 16 = \tilde{a}_s \times 20$, we could compare the ratio of the energies in lattice units obtained in the two simulations (as shown in Table 2.4) to the expected value of

$$a_t E / \tilde{a}_t E = a_s \xi / \tilde{a}_s \tilde{\xi} = 20 \, \tilde{\xi} / 16 \, \xi, \tag{2.27}$$

where the ξ's are the renormalized anisotropies in the two simulations. In this way we could check whether finite spacing artefacts are present. It is, however, clear from eq. (2.27) that it is essential to tune the input parameters to get a perfect match in the physical volumes. Table 2.4 shows deviations of about 4% from the expected value. However the fact that this value is kept almost constant through all the channels made us think that there is a slight mismatch between the physical volumes in the two simulations.

Channel	$\beta = 2.16$	$\beta = 2.0$	ratio
$p = 0\ A_{1g}$	0.543(1)	0.649(4)	1.1952(76)
$p = 1\ E$	0.598(5)	0.729(3)	1.219(11)
$p = 0\ A_{1g}^*$	0.660(4)	0.797(3)	1.2076(86)
$p = 0\ A_{2u}$	0.656(5)	0.791(7)	1.205(14)
$p = 0\ B_{1g}$	0.657(4)	0.797(3)	1.2131(86)
$p = 0\ B_{2g}$	0.658(9)	0.796(3)	1.2097(86)
$p = 2\ A_1$	0.671(3)	0.804(6)	1.198(10)
$p = 2\ B_1$	0.668(3)	0.805(7)	1.205(11)
$p = 2\ B_2$	0.674(7)	0.805(6)	1.194(15)
$p = 2\ E$	0.663(3)	0.805(4)	1.2142(81)
$p = 1\ A_1$	0.713(4)	0.864(3)	1.2118(79)
$p = 1\ A_2$	0.695(4)	0.840(3)	1.2086(81)
$p = 1\ B_1$	0.710(4)	0.869(3)	1.2239(80)
$p = 1\ B_2$	0.720(4)	0.886(11)	1.230(16)

Table 2.4: Energy estimates in terms of a_t^{-1} for $\beta = 2.0$ and $\tilde{a}_t^{-1}$ for $\beta = 2.16$. The ratio should be compared with $a_t/\tilde{a}_t \approx 1.25$.

Channel	N_{exp}	fit range	$\chi^2/$dof	Q	energies	overlap
$p = 0\ A_{1g}$	1	2-7	1.9/4	0.77	**0.309(1)**	0.987(3)
	2	2-6	1.5/1	0.22	0.309(1)	0.987(2)
$p = 1\ E$	1	3-5	0.69/1	0.41	**0.454(2)**	0.963(5)
	2	1-11	4.9/7	0.68	0.446(9)	0.92(5)
$p = 0\ A_{1g}^*$	1	2-8	1.3/5	0.93	**0.524(3)**	0.967(5)
	2	1-11	1.8/7	0.97	0.524(5)	0.965(13)
$p = 0\ A_{2u}$	1	3-7	3.6/3	0.64	**0.459(4)**	0.95(1)
	2	1-11	7.1/7	0.41	0.455(12)	0.92(6)
$p = 0\ B_{1g}$	1	2-6	1.3/3	0.73	**0.534(3)**	0.967(6)
	2	1-8	4/4	0.41	0.533(6)	0.963(20)
$p = 0\ B_{2g}$	1	2-7	2.2/4	0.7	**0.539(3)**	0.954(6)
	2	1-10	5.8/6	0.45	0.532(9)	0.934(32)
$p = 2\ A_1$	1	2-5	0.052/2	0.97	**0.606(3)**	0.955(5)
$p = 2\ B_1$	1	2-5	3.5/2	0.17	**0.606(3)**	0.954(5)
	2	1-5	0.98/1	0.32	0.594(9)	0.907(43)
$p = 2\ B_2$	1	3-7	0.65/3	0.88	**0.604(6)**	0.92(1)
	2	1-7	0.67/3	0.88	0.601(14)	0.91(5)
$p = 2\ E$	1	3-8	7.4/4	0.12	0.595(3)	0.928(9)
	2	1-10	10/6	0.11	**0.595(8)**	0.92(3)
$p = 1\ A_1$	1	3-8	3.2/4	0.53	**0.612(6)**	0.87(1)
	2	1-11	2.3/7	0.94	0.584(29)	0.72(15)
$p = 1\ A_2$	1	2-5	1.3/2	0.53	**0.528(2)**	0.956(4)
	2	2-7	3.2/2	0.2	0.528(2)	0.956(4)
$p = 1\ B_1$	1	3-8	0.94/4	0.92	**0.641(6)**	0.91(1)
	2	1-11	2.2/7	0.95	0.627(21)	0.84(1)
$p = 1\ B_2$	1	3-6	0.057/2	0.97	**0.634(7)**	0.87(1)
	2	1-10	5.5/6	0.48	0.630(16)	0.87(1)
	2	2-8	0.47/2	0.79	0.631(9)	0.86(2)

Table 2.5: Results from fits to the $\beta = 2.0$, $L = 8^3 \times 48$ correlators using fifteen operators. Energies are given in units of a_t^{-1}.

Channel	$N_{\exp}$	fit range	χ^2/dof	Q	energies	overlap
$p = 0\ A_{1g}$	1	3-5	0.16/1	0.69	**0.480(2)**	0.970(5)
	2	1-5	0.12/1	0.73	0.475(9)	0.90(1)
$p = 1\ E$	1	3-6	1.7/2	0.43	0.579(1)	0.954(4)
	2	1-5	0.004/1	0.99	**0.575(5)**	0.954(4)
$p = 0\ A_{1g}^{*}$	1	3-6	4.5/2	0.11	0.643(4)	0.932(11)
	2	1-6	2.8/2	0.25	**0.636(13)**	0.89(5)
$p = 0\ A_{2u}$	1	2-5	2.5/3	0.74	**0.631(2)**	0.955(3)
	2	1-9	4.1/5	0.54	0.630(2)	0.954(5)
$p = 0\ B_{1g}$	1	2-6	0.5/3	0.92	**0.657(2)**	0.960(4)
	2	2-6	0.15/1	0.69	0.661(4)	0.97(2)
$p = 0\ B_{2g}$	1	2-4	0.12/1	0.73	**0.656(2)**	0.96(1)
	2	1-8	7.4/4	0.12	0.656(3)	0.963(6)
$p = 2\ A_{1}$	1	3-8	4.9/4	0.29	0.683(3)	0.94(1)
	2	1-5	1.1/1	0.31	**0.680(7)**	0.93(2)
$p = 2\ B_{1}$	1	3-8	1.7/4	0.79	**0.676(3)**	0.93(1)
	1	1-7	3.4/3	0.34	0.673(7)	0.90(1)
$p = 2\ B_{2}$	1	2-4	0.44/1	0.5	**0.679(1)**	0.951(3)
	2	1-5	2.4/1	0.12	0.672(8)	0.93(3)
$p = 2\ E$	1	3-6	0.97/2	0.62	**0.670(3)**	0.919(8)
	2	1-7	4.3/3	0.23	0.658(9)	0.85(5)
$p = 1\ A_{1}$	1	2-8	8.6/5	0.13	0.727(2)	0.937(3)
	2	1-10	8/6	0.24	**0.723(5)**	0.92(1)
$p = 1\ A_{2}$	1	2-8	2.6/5	0.76	0.673(1)	0.942(3)
	2	1-8	1.5/4	0.83	**0.670(4)**	0.93(1)
$p = 1\ B_{1}$	1	3-8	4.1/4	0.4	0.730(4)	0.92(1)
	2	1-8	3.1/4	0.54	**0.721(9)**	0.87(7)
$p = 1\ B_{2}$	1	3-8	5.1/4	0.28	0.743(4)	0.91(1)
	2	1-8	4.5/4	0.35	**0.738(13)**	0.89(4)

Table 2.6: Results from fits to the $\beta = 2.0$, $L = 8^2 \times 12 \times 48$ correlators using fifteen operators. Energies are given in units of a_t^{-1}.

Channel	N_{exp}	fit range	$\chi^2/$dof	Q	energies	overlap
$p=0\ A_{1g}$	1	3-7	1.4/3	0.71	**0.649(4)**	0.94(1)
	2	1-7	2.3/3	0.5	0.645(8)	0.91(4)
$p=1\ E$	1	3-6	0.81/2	0.67	0.729(3)	0.931(7)
	2	1-6	1.7/2	0.43	**0.725(7)**	0.91(3)
$p=0\ A_{1g}^{*}$	1	2-4	0.00042/1	0.98	**0.797(3)**	0.934(6)
	2	1-8	8.6/4	0.07	0.797(3)	0.934(6)
$p=0\ A_{2u}$	1	3-6	0.17/2	0.92	**0.791(7)**	0.94(2)
	1	2-6	0.2/3	0.98	0.789(3)	0.938(6)
	2	2-6	0.21/1	0.65	0.788(6)	0.931(6)
$p=0\ B_{1g}$	1	2-7	2.5/4	0.64	**0.797(3)**	0.931(6)
	1	3-7	1.7/3	0.63	0.791(7)	0.93(2)
	2	1-9	2.9/5	0.72	0.783(17)	0.88(6)
$p=0\ B_{2g}$	1	2-8	2.7/5	0.74	**0.796(3)**	0.943(6)
	1	3-8	2.4/4	0.67	0.791(8)	0.93(2)
	2	1-8	2.1/4	0.72	0.784(11)	0.90(4)
$p=2\ A_1$	1	3-8	0.24/3	0.97	**0.804(6)**	0.90(1)
	2	2-10	0.89/5	0.97	0.803(7)	0.89(2)
$p=2\ B_1$	1	3-7	1.5/3	0.67	0.809(5)	0.92(1)
	2	1-7	1.3/3	0.72	**0.805(7)**	0.90(4)
$p=2\ B_2$	1	3-5	0.025/1	0.87	**0.805(6)**	0.91(1)
	2	1-8	7.3/5	0.23	0.800(11)	0.87(5)
$p=2\ E$	1	3-8	2.6/4	0.62	**0.805(4)**	0.92(1)
	2	1-8	1.6/4	0.81	0.797(8)	0.88(3)
$p=1\ A_1$	1	2-8	2.2/5	0.82	**0.864(3)**	0.932(5)
	2	2-10	3.5/5	0.62	0.860(6)	0.91
$p=1\ A_2$	1	2-7	2.6/4	0.62	**0.840(3)**	0.915(5)
	1	1-10	7.8/6	0.25	0.836(5)	0.90(1)
$p=1\ B_1$	1	2-4	0.44/1	0.51	**0.869(3)**	0.933(5)
$p=1\ B_2$	1	3-5	0.44/1	0.51	0.886(8)	0.92(2)
	1	2-6	1.8/3	0.62	0.890(3)	0.933(6)
	2	1-8	3.9/4	0.42	**0.886(11)**	0.933(6)

Table 2.7: Results from fits to the $\beta = 2.0$, $L = 8^2 \times 16 \times 48$ correlators using fifteen operators. Energies are given in units of a_t^{-1}.

Channel	N_{exp}	fit range	χ^2/dof	Q	energies	overlap
$p = 0\ A_{1g}$	1	2-5	2.3/2	0.32	**0.651(2)**	0.963(4)
	2	1-8	5.9/4	0.21	0.647(6)	0.95(2)
$p = 1\ E$	1	2-5	1/2	0.6	**0.733(1)**	0.947(3)
	2	1-6	1.7/2	0.42	0.732(1)	0.944(4)
$p = 0\ A_{1g}^*$	1	2-5	4.3/2	0.12	**0.794(4)**	0.926(7)
$p = 0\ A_{2u}$	1	2-5	0.65/2	0.72	**0.788(4)**	0.930(7)
	2	2-11	9.9/6	0.13	0.788(4)	0.931(5)
$p = 0\ B_{1g}$	1	2-8	2.1/5	0.83	**0.801(4)**	0.942(8)
	1	3-8	2.1/4	0.72	0.799(9)	0.93(2)
	2	1-9	2.2/5	0.82	0.800(6)	0.93(1)
$p = 0\ B_{2g}$	1	2-8	9.5/5	0.09	0.800(4)	0.946(7)
	1	3-7	2.5/3	0.48	**0.780(9)**	0.88(2)
	2	1-7	5.2/3	0.16	0.782(15)	0.87(6)
$p = 2\ A_1$	1	3-6	1.4/2	0.49	**0.813(7)**	0.91(1)
	2	1-7	4.2/3	0.24	0.810(19)	0.89(9)
$p = 2\ B_1$	1	3-7	5.9/3	0.12	**0.813(7)**	0.92(1)
	2	1-7	6.2/3	0.1	0.815(8)	0.93(2)
$p = 2\ B_2$	1	2-7	5.3/4	0.26	**0.808(3)**	0.935(5)
	2	1-7	6.2/3	0.1	0.815(8)	0.93(2)
$p = 2\ E$	1	2-8	3.6/5	0.61	**0.807(2)**	0.935(3)
	1	1-9	3.9/5	0.56	0.806(3)	0.935(3)
$p = 1\ A_1$	1	2-5	1.6/2	0.44	**0.862(3)**	0.929(6)
	2	1-5	0.81/1	0.37	0.853(12)	0.89(4)
$p = 1\ A_2$	1	2-6	4.7/3	0.2	0.841(3)	0.921(6)
	1	3-6	0.88/2	0.64	**0.826(8)**	0.921(6)
	2	1-6	0.77/2	0.68	0.817(15)	0.83(6)
$p = 1\ B_1$	1	2-6	0.12/3	0.99	**0.867(3)**	0.932(6)
	2	2-6	0.13/1	0.72	0.865(5)	0.92
$p = 1\ B_2$	1	3-6	2.2/2	0.33	**0.863(9)**	0.86(2)
	2	1-6	2.3/2	0.32	0.855(18)	0.82(7)

Table 2.8: Results from fits to the $\beta = 2.0$, $L = 6^2 \times 16 \times 48$ correlators using fifteen operators. Energies are given in units of a_t^{-1}.

Channel	N_{exp}	fit range	χ^2/dof	Q	energies	overlap
$p = 0 \; A_{1g}$	1	3-7	0.74/3	0.86	0.839(8)	0.99(2)
	1	2-7	5/4	0.29	**0.823(3)**	0.946(6)
	2	1-10	21/6	0.002	0.836(1)	0.971(4)
$p = 1 \; E$	1	3-8	4.4/4	0.35	0.887(5)	0.90(1)
	2	1-9	4/5	0.55	**0.880(10)**	0.90(1)
$p = 0 \; A_{1g}^*$	1	3-7	0.64/3	0.89	0.945(15)	0.87(3)
	1	2-7	3.1/4	0.54	0.967(5)	0.93(1)
	2	1-9	2.4/5	0.79	**0.956(15)**	0.89(5)
$p = 0 \; A_{2u}$	1	2-7	5.1/4	0.28	**0.952(5)**	0.927(9)
	2	1-9	4.6/5	0.46	0.932(16)	0.85(6)
$p = 0 \; B_{1g}$	1	2-7	1.2/4	0.87	**0.962(5)**	0.93(1)
	2	1-7	1.2/3	0.75	0.961(8)	0.92(1)
$p = 0 \; B_{2g}$	1	2-6	0.9/3	0.82	**0.955(5)**	0.94(1)
	2	1-6	0.9/2	0.64	0.955(7)	0.94(1)
$p = 2 \; A_1$	1	2-5	2.8/2	0.25	**0.972(4)**	0.921(7)
	2	1-7	4.9/3	0.18	0.960(13)	0.88(4)
$p = 2 \; B_1$	1	2-5	1.9/2	0.39	**0.965(4)**	0.920(7)
	2	1-9	4.7/5	0.45	0.954(13)	0.88(4)
$p = 2 \; B_2$	1	3-8	4/4	0.41	0.939(10)	0.85(2)
	2	1-10	5.7/6	0.45	**0.936(18)**	0.85(2)
$p = 2 \; E$	1	2-5	1.7/2	0.43	0.960(2)	0.922(5)
	2	1-9	4.7/5	0.46	**0.955(9)**	0.922(5)
$p = 1 \; A_1$	1	3-6	0.23/2	0.89	**0.998(13)**	0.87(3)
	1	2-6	1.6/3	0.67	1.013(4)	0.913(8)
	2	1-6	0.52/2	0.77	0.993(10)	0.87(3)
$p = 1 \; A_2$	1	3-5	0.86/1	0.35	**0.976(13)**	0.79(3)
	1	2-5	13/2	0.001	1.021(5)	0.907(8)
	2	1-10	12/6	0.05	0.987(29)	0.7(1)
$p = 1 \; B_1$	1	3-5	2.6/1	0.1	**0.991(13)**	0.85(3)
	1	2-4	2.4/1	0.12	1.011(5)	0.908(8)
	2	1-9	8.2/5	0.15	0.985(28)	0.8(1)
$p = 1 \; B_2$	1	3-6	2.3/2	0.31	**1.011(14)**	0.85(3)
	1	2-5	1.6/2	0.45	1.028(5)	0.899(8)
	2	1-7	4.8/3	0.19	1.010(15)	0.83(8)

Table 2.9: Results from fits to the $\beta = 2.0$, $L = 8^2 \times 20 \times 48$ correlators using fifteen operators. Energies are given in units of a_t^{-1}.

Channel	N_{exp}	fit range	$\chi^2/$dof	Q	energies	overlap
$p=0\ A_{1g}$	1	2-5	0.17/2	0.92	**0.543(1)**	0.973(3)
	2	2-7	2.6/2	0.28	0.543(1)	0.973(4)
$p=1\ E$	2	2-11	9.7/6	0.14	**0.598(5)**	0.91(2)
$p=0\ A_{1g}^*$	1	3-8	7.6/4	0.11	**0.660(4)**	0.92(1)
	2	1-8	5.9/4	0.21	0.644(16)	0.84(9)
$p=0\ A_{2u}$	1	3-8	6/4	0.2	**0.656(5)**	0.91(1)
	2	1-8	4.1/4	0.39	0.637(16)	0.80(8)
$p=0\ B_{1g}$	1	3-8	2.2/4	0.7	**0.657(4)**	0.93(1)
	2	1-11	4.1/7	0.77	0.652(10)	0.90(4)
$p=0\ B_{2g}$	1	3-8	1/4	0.91	**0.658(4)**	0.91(1)
	2	1-9	3.4/5	0.63	0.644(15)	0.82(8)
$p=2\ A_1$	1	3-8	2.8/4	0.59	**0.671(3)**	0.922(9)
	2	2-9	1.9/4	0.76	0.659(15)	0.86(8)
$p=2\ B_1$	1	3-6	0.11/2	0.95	**0.668(3)**	0.917(9)
	2	1-6	0.91/2	0.63	0.652(12)	0.83(6)
$p=2\ B_2$	1	4-8	2.5/3	0.48	0.676(7)	0.92(3)
	2	1-9	2.4/5	0.79	**0.674(7)**	0.92(2)
$p=2\ E$	1	3-7	4.3/3	0.23	**0.663(3)**	0.929(6)
	2	2-7	0.34/2	0.85	0.644(16)	0.83(9)
$p=1\ A_1$	1	3-5	0.84/1	0.36	**0.713(4)**	0.918(11)
	2	1-9	8.4/5	0.13	0.707(12)	0.89(5)
$p=1\ A_2$	1	3-5	1.3/1	0.26	**0.695(4)**	0.92(1)
	2	1-5	0.19/1	0.66	0.680(20)	0.84(10)
$p=1\ B_1$	1	3-8	1.9/4	0.76	**0.710(4)**	0.906(10)
	2	1-9	7.4/5	0.19	0.703(14)	0.86(7)
$p=1\ B_2$	1	3-5	0.47/1	0.49	**0.720(4)**	0.90(1)
	2	1-9	7.1/5	0.21	0.709(13)	0.84(6)

Table 2.10: Results from fits to the $\beta = 2.16$, $L = 8^2 \times 20 \times 48$ correlators using fifteen operators. Energies are given in units of a_t^{-1}.
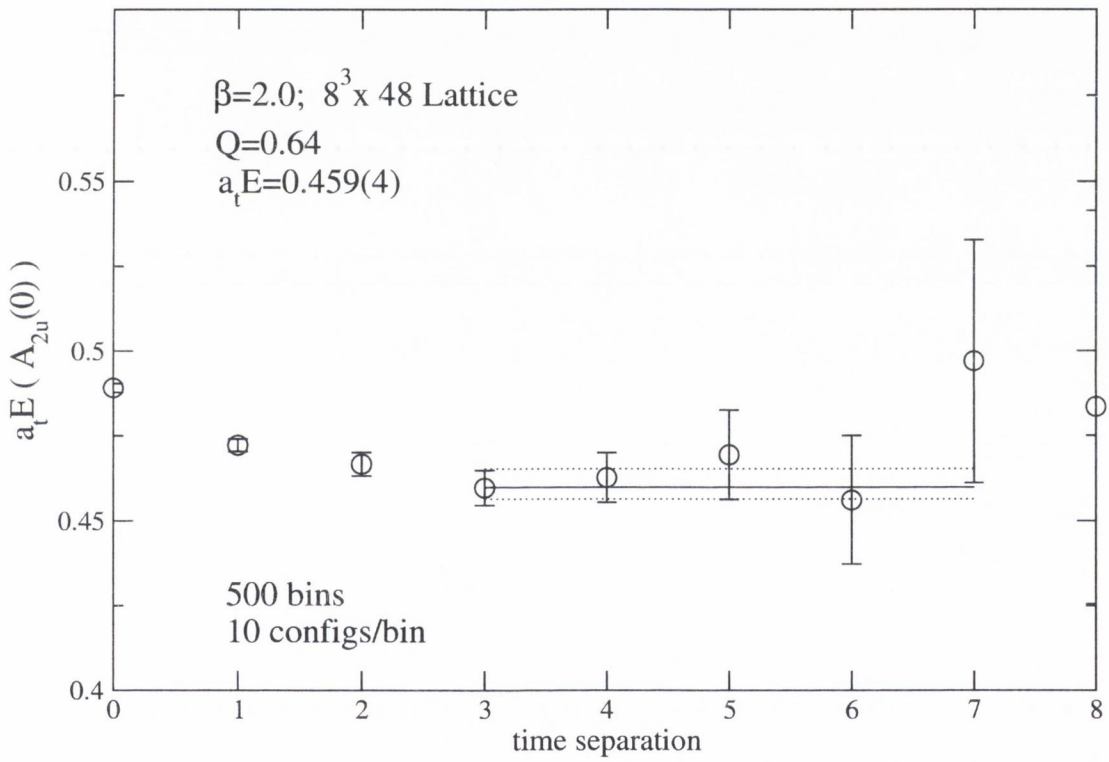
Figure 2-5: Effective energy plot showing the results of a single-exponential fit to the torelon correlation function for the $A_{2u}(0)$ channel.
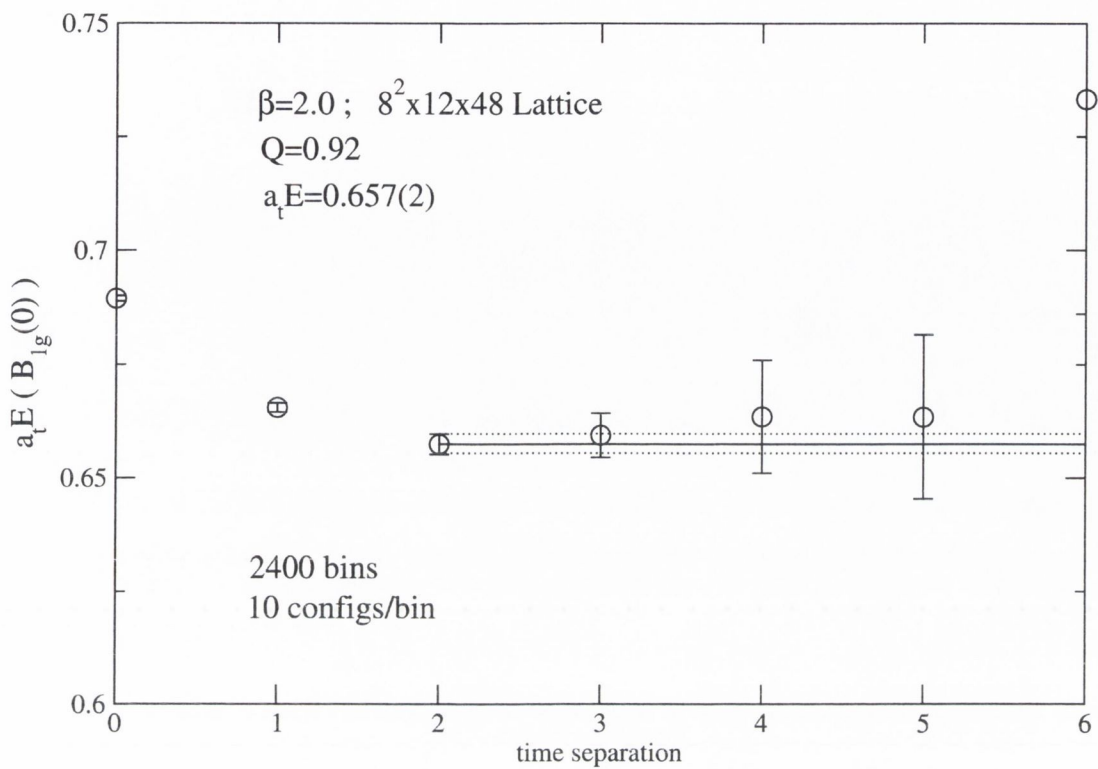
Figure 2-6: Effective energy plot showing the results of a single-exponential fit to the torelon correlation function for the $B_{1g}(0)$ channel.

Figure 2-7: Effective energy plot showing the results of a single-exponential fit to the torelon correlation function for the $B_{2g}(0)$ channel.

Figure 2-8: Effective energy plot showing the results of a single-exponential fit to the torelon correlation function for the $A_1(1)$ channel.

Figure 2-9: Effective energy plot showing the results of a single-exponential fit to the torelon correlation function for the $A_2(1)$ channel.

Figure 2-10: Effective energy plot showing the results of a single-exponential fit to the torelon correlation function for the $B_1(1)$ channel.
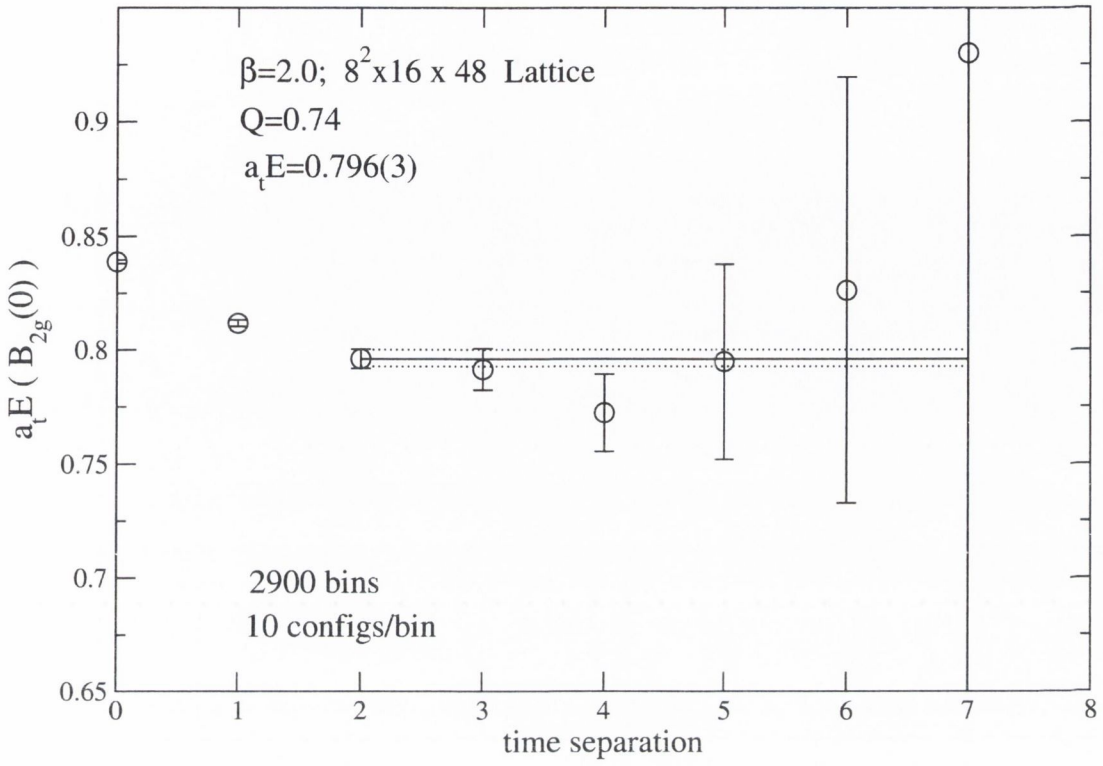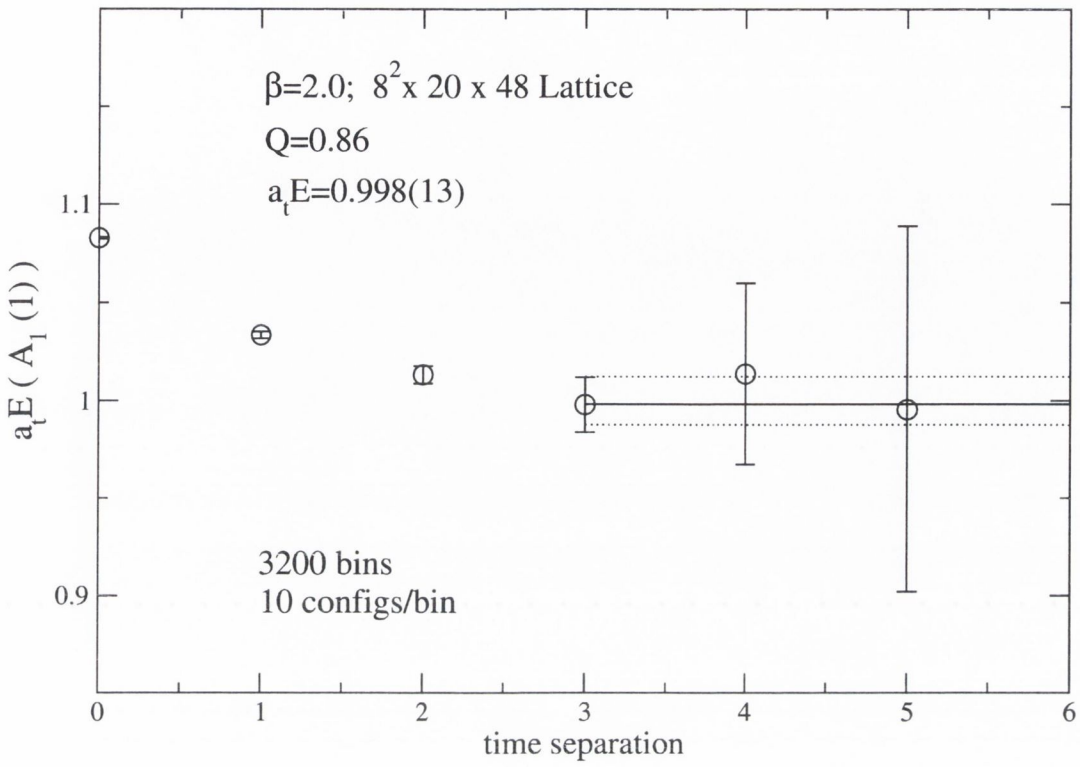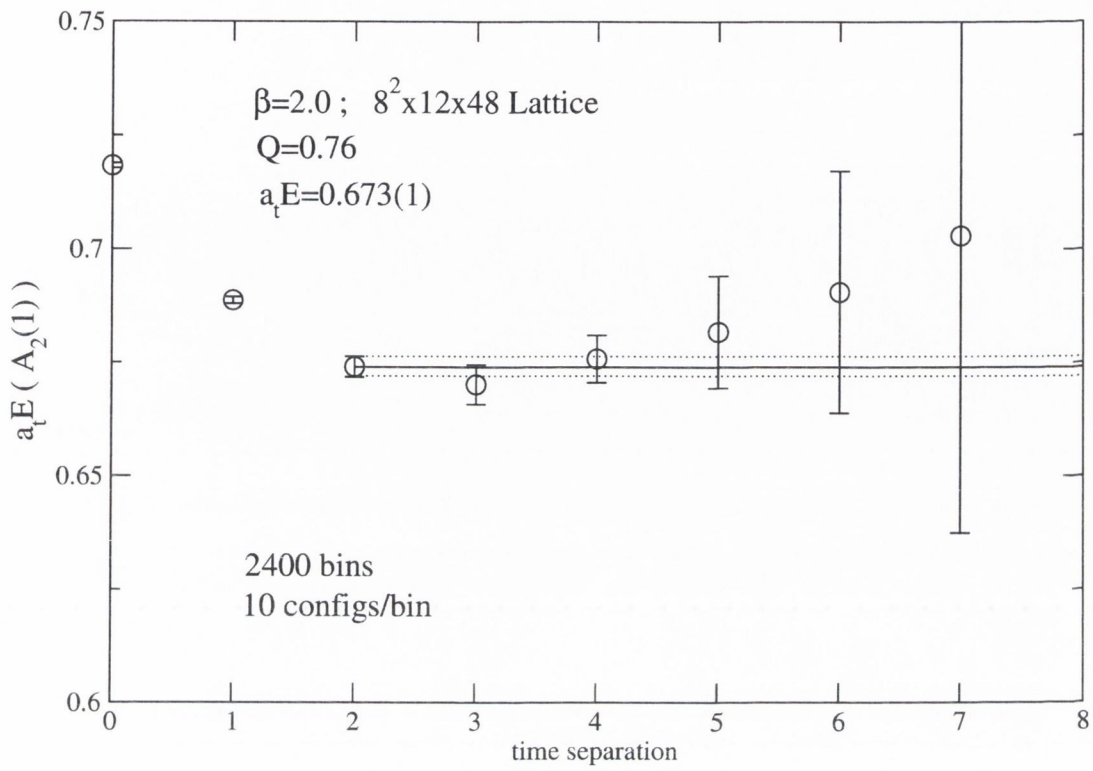
Figure 2-11: Effective energy plot showing the results of a single-exponential fit to the torelon correlation function for the $A_1(2)$ channel.
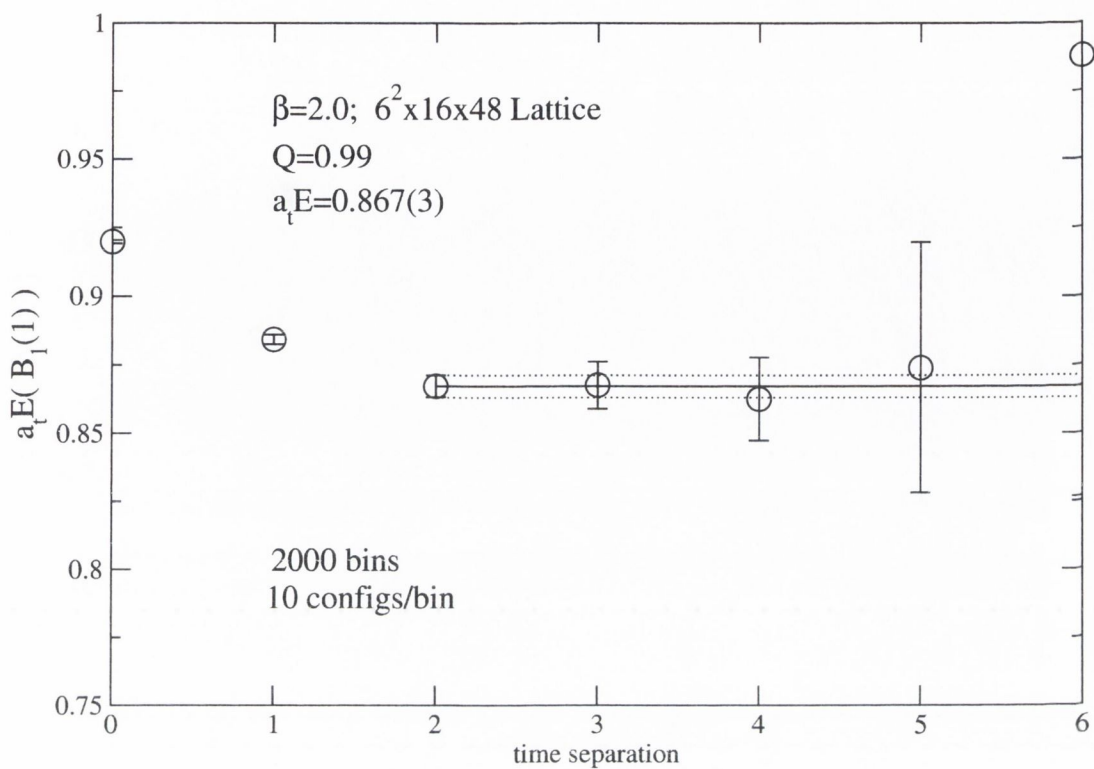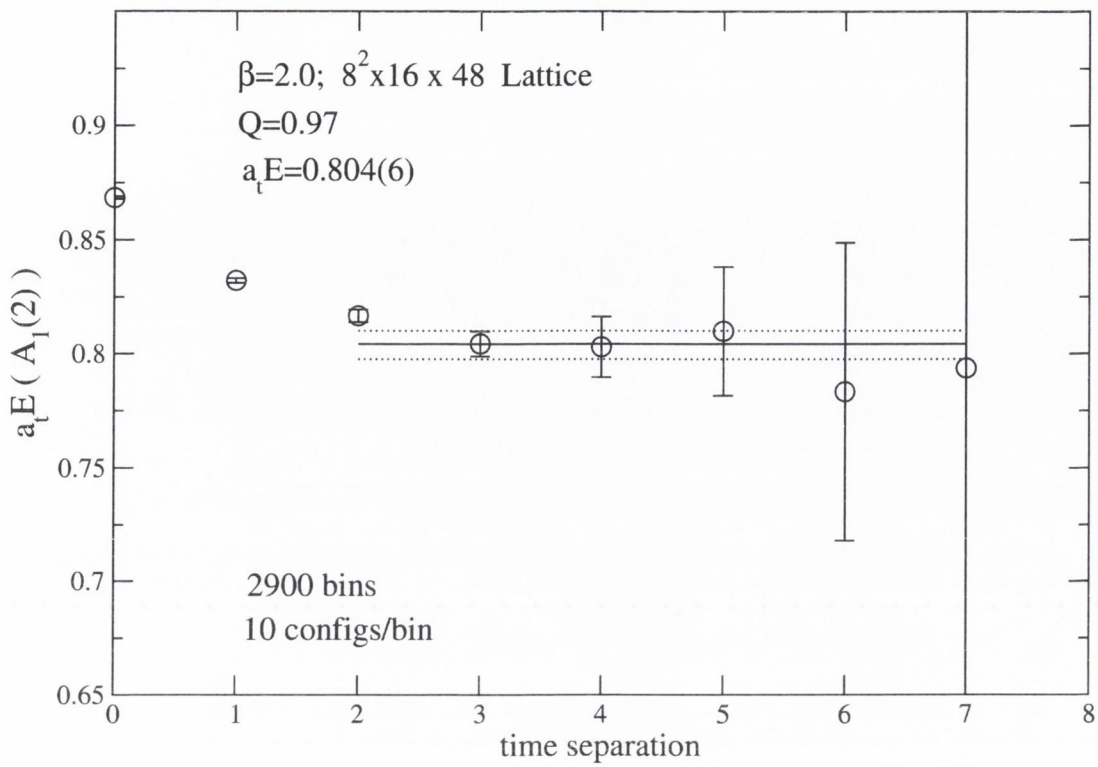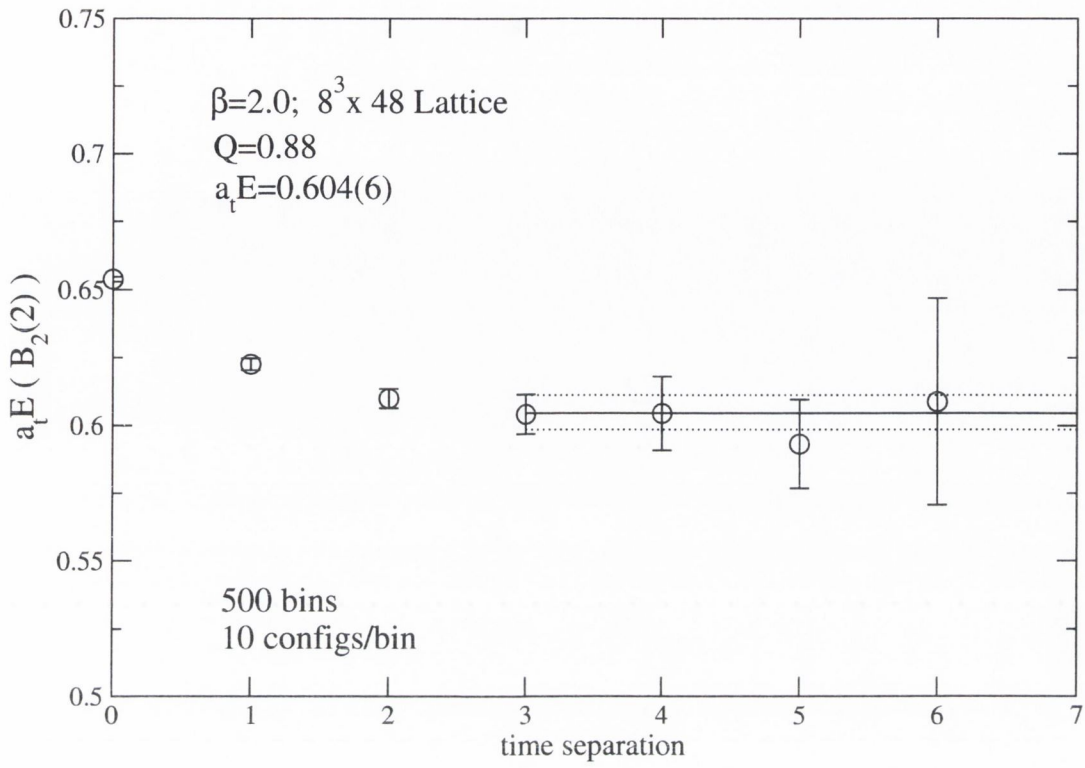
Figure 2-12: Effective energy plot showing the results of a single-exponential fit to the torelon correlation function for the $B_2(2)$ channel.
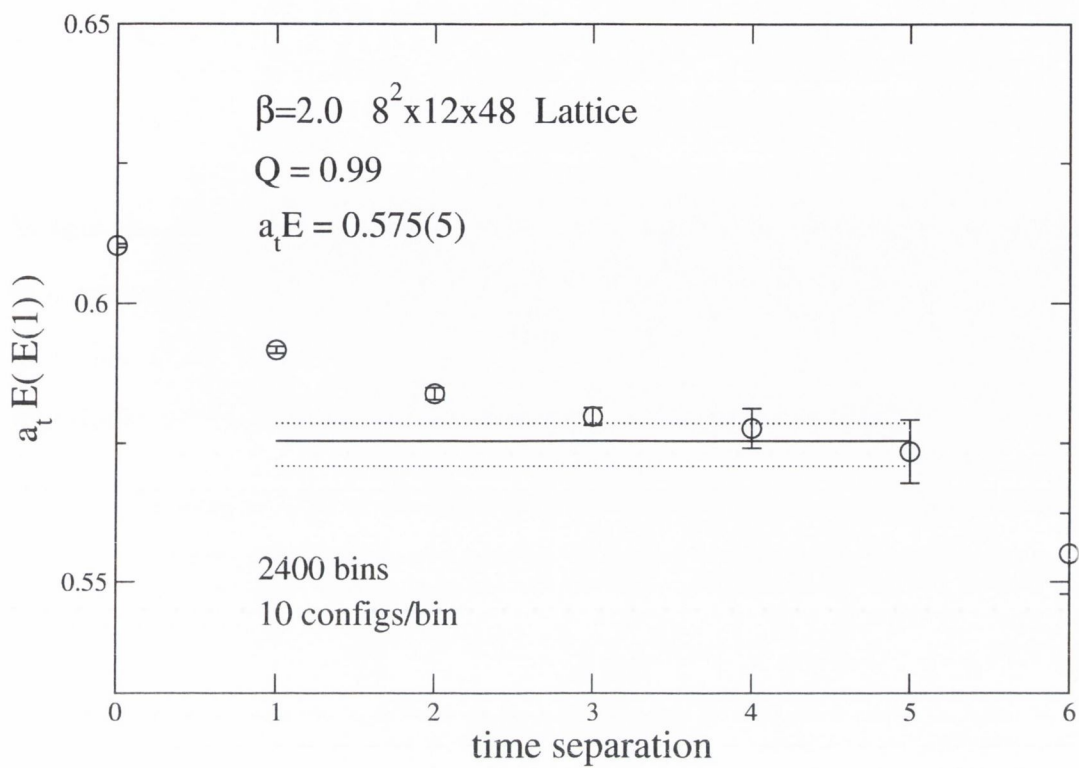
Figure 2-13: Effective energy plot showing the results of a two-exponential fit to the torelon correlation function for the $E(1)$ channel.

2.9 Comments and comparisons with the literature

In this chapter we described the technology used in order to evaluate the spectrum of a periodic QCD flux tube. Considerations of the center symmetry only, allowed us to identify (see Sec. 2.3) the relevant symmetries of a closed flux tube encircling a periodic boundary with one unit net winding number: the "torelon". The torelon state, in its simplest form can be written

$$L_i(t) = \text{Tr } \Pi_{k=1}^{L_s} U_i(\vec{x} + k\hat{i}, t), \tag{2.28}$$

(using a combination of smeared and blocked links), and has been widely used previously in literature to evaluate the string tension (see Refs. [47, 49, 48, 52]).

To my knowledge, the work presented here is the first that tries to create systematically torelon operators that overlap states with all the quantum numbers allowed by the center symmetry. For completeness, therefore, we decided to describe briefly in Sec. 2.5 the technology adopted to this aim. These operators were also improved using the usual smearing method, as described in Sec. 2.4. The method adopted here is the analytic smearing proposed by C. Morningstar and M. Peardon in Ref. [53], whose implementation is very efficient. The standard variational method is then applied in order to obtain the operator that "best" overlaps the lightest state of each particular channel as described in Sec 2.6. In this section, details of the analysis are also given. In Sec. 2.8 we tried to give a flavor of the finite volume effects and lattice spacing artefacts. We tried to convince the reader of the difficulties encountered in doing a systematic continuum limit extrapolation. For instance, we described that two ingredients are strictly necessary:

1. we need to keep the physical volume fixed: $L = a_s L_s$ in the z-direction,

2. we need to calculate the renormalized anisotropy ξ_R,

and both must be obtained with high precision.

Juge et al. in Refs. [36, 37, 38] studied previously the spectrum of a flux tube between static sources and they seemed to avoid a clean continuum extrapolation as described in Sec. 2.8. However, by simulating the energy spectrum for different quark separations with different lattice spacings they showed a good scaling behavior.

Chapter 3

Quark confinement and the string picture

3.1 Introduction

Today almost no one seriously doubts that quantum chromodynamics confines quarks, but despite efforts stretching over thirty years there exists no derivation of quark confinement starting from first principles. It is however widely believed that the confining regime of QCD is described by some kind of effective string model [30, 31]. This conjecture originates from the phenomenological observation that meson states in QCD fall on linear, nearly parallel, Regge trajectories. In fact when the spin, J of mesons is plotted as a function of squared meson masses m^2, it turns out that the resulting points can be sorted into groups which lie on straight lines, and that the slopes of these lines are nearly the same. This remarkable feature of hadron physics can be reproduced by a very simple model that supposes that the meson consists of a straight line-like object of constant energy density running between a massless quark and antiquark. A way of making this model more realistic would be to allow for quantum fluctuations of the line-like object in directions transverse to the line. These considerations led to the development of string theory and in particular to the

Nambu-Goto action

$$S_N = \frac{1}{2\pi\alpha'} \int d\tau d\sigma \sqrt{\det g}, \tag{3.1}$$

where $x^\mu(\tau, \sigma)$ are coordinates of the world-sheet swept out by the line running between the quark and antiquark as it propagates and g is the induced metric on the world-sheet. The Nambu-Goto action, although inspired from hadronic physics, is not an adequate fundamental theory of mesons. In particular, for the long QCD flux tubes that we have considered in the previous chapter most degrees of freedom are frozen out. The only degrees of freedom required by the symmetries of the low-energy theory are the two transverse oscillations of the flux tube. Comparing this feature with the properties of the standard string quantization we arrive at a paradox. In fact the covariant (Virasoro) quantization leads to longitudinal oscillations outside the critical dimension $d = 26$, giving a total of $d - 1$ oscillators, while the light-cone quantization spoils Lorentz invariance outside the critical dimension. Thus, for the purpose of describing the quantum states of a QCD flux tube, none of the standard string quantizations are correct and the string action adopted in order to explain the dynamics of a QCD flux tube should be treated as an effective, rather than a fundamental one. A promising effective string theory was derived by Polchinski and Strominger [55]. This model is valid only for a string whose length is greater compared to the fundamental scale a. In particular in their work they presented a conformal field theory with central charge not equal to d and the resulting covariant quantization with $d - 2$ oscillators. However, the Polchinski and Strominger action, as presented in Ref. [55] does not seem to deviate from the Nambu-Goto action for long strings as will be explained in the following sections. In Sec. 3.2 we present a summary of the study of Polchinski and Strominger. We caution the reader that this section does not intend to add anything to their work presented in Ref. [55], but serves only as a background for the derivation of the string spectrum, presented in

3.2 Effective bosonic string

As with other effective theories, the action proposed by Polchinski and Strominger contains an infinite number of terms, suppressed by powers of the fundamental scale a and the theory breaks down when extrapolated to short strings. They started by considering strings that wind once around the x^3 direction:

$$x^\mu(\tau, \sigma + 2\pi) = x^\mu(\tau, \sigma) + 2\pi R \delta_3^\mu, \tag{3.2}$$

and wrote a general Lagrangian as an expansion in powers of R^{-1} where each first derivative of x^μ is of order R. They excluded terms proportional to the leading-order equation of motion $\partial_+ \partial_- x^\mu$ (using light-cone coordinates $\tau^\pm = \tau \pm \sigma$) which can be removed by a field redefinition, and terms proportional to the leading-order constraints $\partial_\pm x \cdot \partial_\pm x$, which vanish. Then through order R^{-2} the only possible terms give the action

$$S = \frac{1}{4\pi} \int d\tau^+ d\tau^- \left[\frac{1}{a^2} \partial_+ x^\mu \partial_- x_\mu + \beta \frac{\partial_+^2 x \cdot \partial_- x \partial_+ x \cdot \partial_-^2 x}{(\partial_+ x \cdot \partial_- x)^2} + O(R^{-3}) \right]. \tag{3.3}$$

The expansion around the classical ground state to the leading-order of the action of eq. (3.3) takes the form

$$x_{cl}^\mu = e_+^\mu R \tau^+ + e_-^\mu R \tau^-, \tag{3.4}$$

where the $e_\pm^\mu$ must satisfy the following conditions in order to guarantee the periodicity of eq (3.2) and the Virasoro constraints $T_{\pm\pm} = 0$:

$$e_+^\mu - e_-^\mu = \delta_3^\mu, \tag{3.5}$$

$$e_\pm \cdot e_\pm = 0. \tag{3.6}$$

Also combining eq (3.5) and eq (3.6) in $(e_+ - e_-) \cdot (e_+ - e_-) = 1$ we get the additional condition

$$e_\pm \cdot e_\mp = -\frac{1}{2}. \tag{3.7}$$

The action in eq. (3.3) is invariant $[\delta S \leq O(R^{-2})]$ under the modified conformal transformation

$$\delta x^\mu = \epsilon^-(\tau^-)\partial_- x^\mu - \frac{\beta a^2}{2}\partial_-^2 \epsilon^-(\tau^-)\frac{\partial_+ x^\mu}{\partial_+ x \cdot \partial_- x}. \tag{3.8}$$

The Noether procedure gives the leading correction to the energy momentum tensor, that reads in the work of Polchinski and Strominger [55] as

$$T_{--} = -\frac{1}{2a^2}\partial_- x \cdot \partial_- x + \frac{\beta}{2}\frac{\partial_+ x \cdot \partial_-^3 x}{\partial_+ x \cdot \partial_- x} + O(R^{-2}), \tag{3.9}$$

which obeys $\partial_- T_{--} \leq O(R^{-2})$ (and similarly for $(+ \leftrightarrow -)$).
Introducing the fluctuation y^μ defined as

$$x^\mu = x_{cl}^\mu + y^\mu, \tag{3.10}$$

the Lagrangian and the energy-momentum tensor become

$$L = -\frac{R^2}{8\pi a^2} + \frac{1}{4\pi a^2}\partial_+ y \cdot \partial_- y + \frac{\beta}{\pi R^2}(\partial_+^2 y \cdot e_-)(e_+ \cdot \partial_-^2 y) + O(R^{-3}), \tag{3.11}$$

and

$$T_{--} = -\frac{R}{a^2}e_- \cdot \partial_- y - \frac{1}{2a^2}\partial_- y \cdot \partial_- y - \frac{\beta}{R}e_+ \cdot \partial_-^3 y + O(R^{-2}), \qquad (3.12)$$

respectively.

The general solution compatible with the periodicity requirement is

$$x^\mu = x_{cl}^\mu + aa_0\tau_- + ia\sum_{n\neq 0}\frac{1}{n}a_n e^{-in\tau_-} + a\tilde{a}_0\tau_+ + ia\sum_{n\neq 0}\frac{1}{n}\tilde{a}_n e^{-in\tau_+}, \qquad (3.13)$$

with $a_0 = \tilde{a}_0$ and

$$\partial_- y^\mu = a\sum_{n=-\infty}^{\infty} a_n e^{-in\tau_-}, \quad \partial_+ y^\mu = a\sum_{n=-\infty}^{\infty} \tilde{a}_n e^{-in\tau_+}. \qquad (3.14)$$

Thus in order to obtain the Fourier modes of the energy momentum tensor, L_m and $\tilde{L}_m$ simply insert the expansion (3.14) into the Virasoro constraints $T_{--} = 0$ and $T_{++} = 0$

$$\begin{aligned}
T_{++} &= -\frac{1}{2}\sum_{n,m}\tilde{a}_n \cdot \tilde{a}_m e^{-i(n+m)\tau_+} - \frac{R}{a}e_+ \cdot \sum_n \tilde{a}_n e^{-in\tau_+} \\
&\quad + \frac{a\beta}{R}e_- \cdot \sum_n n^2 \tilde{a}_n e^{-in\tau_+} + O(R^{-2}) \\
&= \sum_n \tilde{L}_n e^{-in\tau_+} = 0,
\end{aligned}$$

where the Virasoro operator reads

$$\tilde{L}_n = \frac{1}{2}\sum_m :\tilde{a}_{n-m} \cdot \tilde{a}_m: + \frac{R}{a}e_+ \cdot \tilde{a}_n + \frac{\beta}{2}\delta_{n,0} - \frac{an^2\beta}{R}e_- \cdot \tilde{a}_n + O(R^{-2}). \qquad (3.15)$$

In a similar way, from T_{--} we obtain L_n

$$L_n = \frac{1}{2} \sum_m : a_{n-m} \cdot a_m : + \frac{R}{a} e_- \cdot a_n + \frac{\beta}{2} \delta_{n,0} - \frac{an^2\beta}{R} e_+ \cdot a_n + O(R^{-2}). \qquad (3.16)$$

The normal ordering constant $\frac{\beta}{2}$ in (3.16) can be obtained by the algebra of the Virasoro generators. In particular from the $T_{--}T_{--}$ operator product Polchinski and Strominger showed that the central charge and the Virasoro algebra are given by

$$c = d + 12\beta, \qquad\qquad c = 26, \qquad\qquad (3.17)$$

and

$$[L_m, L_n] = (m - n)L_{m+n} + \frac{c}{12}(m^3 - m)\delta_{m+n}. \qquad (3.18)$$

The physical states of the full Hilbert space are then those which satisfy the Virasoro conditions:

$$L_0 = \tilde{L}_0 = 1, \qquad\qquad (3.19)$$

$$L_m = m \;\; \forall m > 0. \qquad\qquad (3.20)$$

3.3   Symmetries

Since we are interested in comparing the energy spectrum of a QCD flux tube as described in the previous chapter to an effective string theory, we need to classify the string states by their quantum numbers with respect to total momentum, angular momentum and parity and therefore we need to find the corresponding operators. To obtain the total momentum of the string, consider the symmetry $x^\mu \to x^\mu + a^\mu$ and apply the Noether procedure to get the conserved current $\partial_a P^a_\mu = 0$ where

$$P_a^\mu = \frac{1}{4\pi a^2} \partial_a x^\mu. \tag{3.21}$$

The total conserved momentum of the string is then found by integrating the current over σ at $\tau = 0$ [57]. This gives

$$
\begin{aligned}
p^\mu &= \frac{1}{4\pi a^2} \int_0^{2\pi} d\sigma \left[\frac{dx^\mu}{d\tau} \right]_{\tau=0} \\
&= \frac{1}{4\pi a^2} \int_0^{2\pi} d\sigma \left[(e_+^\mu R + e_-^\mu R) + a \sum_n a_n^\mu e^{in\sigma} + a \sum_n \tilde{a}_n^\mu e^{-in\sigma} \right] \\
&= \frac{R}{2a^2} (e_+^\mu + e_-^\mu) + \frac{1}{2a} (a_0^\mu + \tilde{a}_0^\mu) .
\end{aligned} \tag{3.22}
$$

Thus using eq. (3.7) one obtains

$$p^\mu p_\mu = -\frac{R^2}{4a^4} + \frac{R}{a^3} e_+ \cdot \tilde{a}_0 + \frac{R}{a^3} e_- \cdot a_0 + \frac{1}{2a^2} a_0^2 + \frac{1}{2a^2} \tilde{a}_0^2. \tag{3.23}$$

A similar statement applies to the current of the angular momentum $J_a^{\mu\nu}$. For instance, considering only the angular momentum on the plane perpendicular to the x^3 direction we have for $\mu, \nu \neq 3$:

$$\left[\frac{dx^\nu}{d\tau} \right]_{\tau=0} = 2a^2 p^\nu + a \sum_{n\neq 0} a_n^\nu e^{in\sigma} + a \sum_{n\neq 0} \tilde{a}_n^\nu e^{-in\sigma}, \tag{3.24}$$

(where we used eq. (3.22)) and thus

$$
\begin{aligned}
J^{\mu\nu} &= \frac{1}{4\pi a^2} \int_0^{2\pi} d\sigma \left[x^\mu \frac{dx^\nu}{d\tau} - x^\nu \frac{dx^\mu}{d\tau} \right]_{\tau=0} \\
&= \frac{1}{4\pi a^2} \int_0^{2\pi} d\sigma [2ia^3 p^\nu \left(\sum_{n\neq 0} \frac{1}{n} a_n^\mu e^{in\sigma} + \sum_{n\neq 0} \frac{1}{n} \tilde{a}_n^\mu e^{-in\sigma} \right) \\
&\quad + ia^2 \sum_{n,m\neq 0} \frac{1}{n} a_n^\mu a_m^\nu e^{i(n+m)\sigma} + ia^2 \sum_{n,m\neq 0} \tilde{a}_n^\mu \tilde{a}_m^\nu e^{-i(n+m)\sigma} - (\mu \leftrightarrow \nu)],
\end{aligned}
$$

66

where other terms like $[a_n^\mu, \tilde{a}_m^\nu]$ vanish from the Poisson brackets. We therefore obtain

$$J^{\mu\nu} = E^{\mu\nu} + \tilde{E}^{\mu\nu} \quad \text{for } \mu, \nu \neq 3, \tag{3.25}$$

where

$$E^{\mu\nu} = -\frac{i}{2} \sum_{n \neq 0} \frac{1}{n} \left(a_{-n}^\mu a_n^\nu - a_{-n}^\nu a_n^\mu \right), \tag{3.26}$$

with an identical expression for $\tilde{E}_{\mu\nu}$ in terms of $\tilde{a}_n^\mu$.

We conclude this section by introducing two more symmetries that we will call $\mathcal{R}$-parity and $\mathcal{P}$-parity. The coordinate transformation

$$\sigma' = 2\pi - \sigma, \tag{3.27}$$

which changes the orientation (handedness) of the world-sheet is the symmetry generated by the $\mathcal{R}$-parity operator. Applying eq. (3.27) twice gives the identity, so $\mathcal{R}^2 = 1$ and the eigenvalues of $\mathcal{R}$ are ± 1. From the mode expansion of $x^\mu = x_{cl}^\mu + y^\mu$ given by eq. (3.13) one obtains

$$
\begin{aligned}
\mathcal{R} x^\mu \mathcal{R}^{-1} &= (2\pi - \sigma) R \delta_3^\mu + (Re_+^\mu + a\tilde{a}_0^\mu + Re_-^\mu + a a_0^\mu)\tau \\
&+ ia \sum_{n \neq 0} \frac{1}{n} a_n^\mu e^{-in\tau_+} + ia \sum_{n \neq 0} \frac{1}{n} \tilde{a}_n^\mu e^{-in\tau_-} \\
&= \mathcal{R} \left(R\delta_3^\mu \sigma \right) \mathcal{R}^{-1} + (Re_+^\mu + a\tilde{a}_0^\mu + Re_-^\mu + a a_0^\mu)\tau \\
&+ ia \sum_{n \neq 0} \frac{1}{n} \mathcal{R} a_n^\mu \mathcal{R}^{-1} e^{-in\tau_-} + ia \sum_{n \neq 0} \frac{1}{n} \mathcal{R} \tilde{a}_n^\mu \mathcal{R}^{-1} e^{-in\tau_+},
\end{aligned}
\tag{3.28}
$$

which, comparing the Fourier modes, gives:

$$\mathcal{R} a_n^\mu \mathcal{R}^{-1} = \tilde{a}_n^\mu, \tag{3.29}$$

$$\mathcal{R} \tilde{a}_n^\mu \mathcal{R}^{-1} = a_n^\mu. \tag{3.30}$$

The $\mathcal{P}$-parity operator reflects the string in one coordinate axis:

$$\mathcal{P} : (x^1, x^2) \to (-x^1, x^2). \tag{3.31}$$

From the mode expansion of $x^\mu = x_{cl}^\mu + y^\mu$ given by eq. (3.13) one obtains

$$\mathcal{P} a_n^1 \mathcal{P}^{-1} = -a_n^1, \tag{3.32}$$

$$\mathcal{P} a_n^2 \mathcal{P}^{-1} = a_n^2, \tag{3.33}$$

with equivalent relations for the $\tilde{a}$'s.

3.4   Construction of the spectrum

As already said, the "physical states", $|\text{phys} >$ of the full Hilbert space are those which obey the Virasoro constraints:

$$(L_0 + \tilde{L}_0 - 2)|\text{phys} >= 0, \tag{3.34}$$

$$(L_0 - \tilde{L}_0)|\text{phys} >= 0, \tag{3.35}$$

$$L_n|\text{phys} >= 0 \quad \forall m > 0. \tag{3.36}$$

The first condition (3.34) is equivalent to a mass-shell condition since, using eq. (3.16), it implies

$$\frac{1}{2}(a_0^2 + \tilde{a}_0^2) + \frac{R}{a}(e_- \cdot a_0 + e_+ \cdot \tilde{a}_0) + \sum_{n=1}^{\infty}(: a_{-n} \cdot a_n : + : \tilde{a}_{-n} \cdot \tilde{a}_n :) + \beta - 2 + O(R^{-2}) = 0.$$

$$(3.37)$$

With the use of eq. (3.23) this expression becomes

$$-p^2 = \frac{R^2}{4a^4} + \frac{\beta - 2}{a^2} + \frac{N + \tilde{N}}{a^2} + O(R^{-2}), \quad (3.38)$$

where

$$N = \sum_{n=1}^{\infty} a_{-n} \cdot a_n, \quad (3.39)$$

with a similar expression for $\tilde{N}$ in terms of $\tilde{a}_n$. In a similar way the second condition (3.35) takes the form

$$P = \frac{\tilde{a}_0^2}{2} - \frac{a_0^2}{2} + \frac{R}{a}e_+ \cdot \tilde{a}_0 - \frac{R}{a}e_- \cdot a_0 + O(R^{-2}), \quad (3.40)$$

where P can be understood as the operator that generates translations on the string and is given by

$$P = N - \tilde{N}. \quad (3.41)$$

The third condition (3.36) leaves $d - 2$ allowed polarizations for each physical state. In fact, considering the first excited states $\zeta \cdot a_{-1}|0, k, k >$, where the ground state $|0, k, k >$ is an eigenstate of a_0^μ and $\tilde{a}_0^\mu$ with common eigenvalue ak^μ, the L_1 subsidiary condition implies that $\zeta \cdot v = 0$ where

$$v^\mu = \frac{R}{a}e_-^\mu + ak^\mu - \frac{\beta a}{R}e_+^\mu. \quad (3.42)$$

This has $d - 1$ solutions, but v^μ is null, so the solution $\zeta^\mu = v^\mu$ is null and leaves

$d - 2$ oscillations.

The operators N and $\tilde{N}$ in eqs. (3.39) and (3.41) are then to be understood in terms of the transverse oscillations only. It is worth noticing that the conditions in eqs. (3.38) and (3.40) do not differ up to the correction given by Polchinski and Strominger from the physical conditions derived from the simpler Nambu-Goto action. In the rest of this section all formulae obtained for the string spectrum can be regarded as derived from Nambu-Goto theory or equally from Polchinski and Strominger theory (up to the order given in Ref. [55]).

We need now to compare the spectrum of the bosonic string considered above with the gluon excitation spectrum of the QCD flux tube. The first step is to relate the length L of the QCD flux tube to the radius R of the closed string

$$L = 2\pi R. \tag{3.43}$$

Also, the parameter $1/4\pi a^2$ containing the fundamental scale a has dimensions of $(\text{length})^{-2}$ or $(\text{mass})^2$ (see eq. (3.3)) and therefore can be identified as the string tension σ

$$\sigma = \frac{1}{4\pi a^2}. \tag{3.44}$$

Recalling also the value of β, eq. (3.38) can be rewritten as

$$-p^2 = \sigma^2 L^2 - \frac{2}{3}\pi\sigma + 4\pi\sigma\,(N + \tilde{N}). \tag{3.45}$$

The problem is then reduced to finding the excitation modes of the bosonic string with exact momentum P, angular momentum J, $\mathcal{R}$-parity and $\mathcal{P}$-parity for each energy level, i.e. the eigenstates common to the operators P, N,$J = E_{12} + \tilde{E}_{12}$, $\mathcal{R}$ and $\mathcal{P}$. As already noted, after imposition of the physical constraints there are only 2 independent transverse oscillators and this suggests adopting the 2-dimensional

harmonic oscillator algebra.

Noting that the a_m are related to the conventionally normalized harmonic oscillator operators by

$$a_n^\mu = \sqrt{n}a_n^{\mu H}, \tag{3.46}$$

$$a_{-n}^\mu = \sqrt{n}a_n^{\mu\dagger H}, \tag{3.47}$$

where the superscript H denotes the harmonic oscillator operators, we can define the 2-dimensional harmonic oscillator algebra by

$$a_n^d = \frac{1}{\sqrt{2}}(a_n^{1H} - ia_n^{2H}), \quad a_n^{d\dagger} = \frac{1}{\sqrt{2}}(a_n^{1\dagger H} + ia_n^{2\dagger H}), \tag{3.48}$$

$$a_n^s = \frac{1}{\sqrt{2}}(a_n^{1H} + ia_n^{2H}), \quad a_n^{\dagger s} = \frac{1}{\sqrt{2}}(a_n^{1\dagger H} - ia_n^{2\dagger H}). \tag{3.49}$$

Also, from the commutators of a_n^i we get

$$[a_m^d, a_n^d] = 0, \quad [a_m^d, a_n^{d\dagger}] = \delta_{m,n}, \tag{3.50}$$

$$[a_m^s, a_n^s] = 0, \quad [a_m^s, a_n^{s\dagger}] = \delta_{m,n}. \tag{3.51}$$

Similar algebra can be obtained for $\tilde{a}_n^i$. In terms of this algebra the energy, angular momentum and momentum operators in eq. (3.39), eq. (3.26) and eq. (3.41) take the form

$$H = N + \tilde{N} = \sum_i i\,(N_i^d + N_i^s + \tilde{N}_i^d + \tilde{N}_i^s), \tag{3.52}$$

71

$$J = E_{12} + \tilde{E}_{12} = \sum_i (-N_i^s + N_i^d - \tilde{N}_i^s + \tilde{N}_i^d), \tag{3.53}$$

$$P = \sum_i i \, (N_i^s + N_i^d - \tilde{N}_i^s - \tilde{N}_i^d), \tag{3.54}$$

where the N_i's are the number operators $N = a_i^\dagger a_i$. Similarly the $\mathcal{R}$-parity and $\mathcal{P}$-parity operators will act on this new system of oscillators as

$$\mathcal{R} a_n^s \mathcal{R}^{-1} = \tilde{a}_n^s, \quad \mathcal{R} a_n^d \mathcal{R}^{-1} = \tilde{a}_n^d, \tag{3.55}$$

$$\mathcal{P} a_n^s \mathcal{P}^{-1} = -a_n^d, \quad \mathcal{P} a_n^d \mathcal{P}^{-1} = -a_n^s. \tag{3.56}$$

The general eigenstate common to H, J and P is of the form

$$|\phi> = \prod_{jklm} (a_i^{s\dagger})^{n_i^s} (a_j^{d\dagger})^{n_j^d} (\tilde{a}_k^{s\dagger})^{\tilde{n}_k^s} (\tilde{a}_l^{d\dagger})^{\tilde{n}_l^d} |0>, \tag{3.57}$$

with eigenvalues

$$E = \sum_i i n_i^s + \sum_j j n_j^d + \sum_k k \tilde{n}_k^s + \sum_l l \tilde{n}_l^d, \tag{3.58}$$

$$j = -\sum_i n_i^s + \sum_j n_j^d - \sum_k \tilde{n}_k^s + \sum_l \tilde{n}_l^d, \tag{3.59}$$

and

$$p = \sum_i i n_i^s + \sum_j j n_j^d - \sum_k k \tilde{n}_k^s - \sum_l l \tilde{n}_l^d. \tag{3.60}$$

As already said, the quantum ground state $|0; k, k>$ is an eigenvector of a_0^μ and $\tilde{a}_0^\mu$ with common eigenvalue ak^μ and is annihilated by the lowering operators, i.e. $j = 0$, $p = 0$ and $N = \tilde{N} = 0$. If we choose $k = (k_0, 0, 0, k_3)$ and impose the physical

condition (3.40) we obtain, with the aid of eq. (3.5), $k_3 = 0$ and for the total energy

$$E_0^2 = \sigma^2 L^2 - \frac{2}{3}\pi\sigma. \tag{3.61}$$

Also this state is an eigenvector of $\mathcal{R}$ and $\mathcal{P}$ with eigenvalue $+1$ and thus can be identified with the gluonic flux tube ground state $A_{1g}(0)$.

Let us now analyze in detail the first three energy levels, where most of the gluon states we are interested in, will lie. Denoting with a common notation t_i the four harmonic operators as

$$t_i = (a_i^{d\dagger}, a_i^{s\dagger}, \tilde{a}_i^{d\dagger}, \tilde{a}_i^{s\dagger}), \tag{3.62}$$

we can list all the possible ways of building an eigenstate of H and P with eigenvalues $E = 1, 2, 3$ and $p = 0, \pm 2$ respectively.

The complete list is presented below, where, for example, the notation $n \times t_m$ denotes the possible ways to build an operator that creates n types of an m string mode of right/left chirality.

	$E = 1$	$E = 2$	$E = 3$
$p = 0$		$2 \times t_1$	
$p = \pm 1$	$1 \times t_1$		$3 \times t_1$
			$1 \times t_1 + 1 \times t_2$
			$1 \times t_1^2 + 1 \times t_1$
$p = \pm 2$		$1 \times t_1^2$	
		$1 \times t_2$	
		$2 \times t_1$	

In the first energy level there are only the states denoted by the notation $1 \times t_1$, that is states created by the string operators $a_1^{d(s)}$. From eq. (3.54) there are just two states with positive momentum that can be built in this way: $a_1^{s\dagger}$ and $a_1^{d\dagger}$ with angular momentum $j = -1$ and $j = 1$ respectively. Also these two states are related

to each other by the $\mathcal{P}$-parity operator and they are not eigenstates of the $\mathcal{R}$-parity operator, as expected. Thus we can identify $(a_1^{d\dagger} + a_1^{s\dagger}, a_1^{d\dagger} - a_1^{s\dagger})|0; k, k >$ with the gluon state $E(1)$ with total energy given by:

$$E_1^2 = E_0^2 + 4\pi\sigma + p_3^2, \tag{3.63}$$

where, from eq. (3.40), $p_3 = \frac{2\pi}{L}$. Applying the same analysis to the rest of the energy levels we can summarize the outcome in Table 3.1.

Level	Type	State	QCD $R(p_z)$
E=0	t_0	$|0\rangle$	$A_{1g}(0)$
E=1	$1 \times t_1$	$(a_1^{d\dagger} + a_1^{s\dagger}, a_1^{d\dagger} - a_1^{s\dagger})|0\rangle$	$E(1)$
E=2	$2 \times t_1$	$(a_1^{d\dagger}\tilde{a}_1^{d\dagger} + a_1^{s\dagger}\tilde{a}_1^{s\dagger})|0\rangle$	$B_{1g}(0)$
		$(a_1^{d\dagger}\tilde{a}_1^{d\dagger} - a_1^{s\dagger}\tilde{a}_1^{s\dagger})|0\rangle$	$B_{2g}(0)$
		$(a_1^{s\dagger}\tilde{a}_1^{d\dagger} - a_1^{d\dagger}\tilde{a}_1^{s\dagger})|0\rangle$	$A_{2u}(0)$
		$(a_1^{s\dagger}\tilde{a}_1^{d\dagger} + a_1^{d\dagger}\tilde{a}_1^{s\dagger})|0\rangle$	$A_{1g}^*(0)$
		$a_1^{s\dagger}a_1^{d\dagger}|0\rangle$	$A_1(2)$
	$1 \times t_1^2$	$((a_1^{d\dagger})^2 + (a_1^{s\dagger})^2)|0\rangle$	$B_1(2)$
		$((a_1^{d\dagger})^2 - (a_1^{s\dagger})^2)|0\rangle$	$B_2(2)$
	$1 \times t_2$	$(a_2^{d\dagger} + a_2^{s\dagger}, a_2^{d\dagger} - a_2^{s\dagger})|0\rangle$	$E(2)$
E=3[1]	$1 \times t_1 + 1 \times t_2$	$(\tilde{a}_1^{d\dagger}a_2^{d\dagger} + \tilde{a}_1^{s\dagger}a_2^{s\dagger})|0\rangle$	$B_1(1)$
		$(\tilde{a}_1^{d\dagger}a_2^{d\dagger} - \tilde{a}_1^{s\dagger}a_2^{s\dagger})|0\rangle$	$B_1(1)$
		$(\tilde{a}_1^{s\dagger}a_2^{d\dagger} + \tilde{a}_1^{d\dagger}a_2^{s\dagger})|0\rangle$	$A_1(1)$
		$(\tilde{a}_1^{s\dagger}a_2^{d\dagger} - \tilde{a}_1^{d\dagger}a_2^{s\dagger})|0\rangle$	$A_2(1)$

[1]This level also includes the states 1* with p=1 and states with p=3 not considered in our calculations

Table 3.1: Lowest string energy levels and their corresponding string and QCD states. The operator $a_m^{d(s)\dagger}$ creates an m string mode of right(left) chirality.

It is worth considering the states that lie on the second level as listed in Table 3.1:

- The two states $(a_1^{d\dagger})^2$ and $(a_1^{s\dagger})^2$ have angular momentum $j = 2$ and $j = -2$ respectively. They are not eigenstates of the $\mathcal{R}$-parity operator and they are related to each other by $\mathcal{P}$-parity. Recalling how the C_{4v} states were built in Appendix A we can identify the corresponding linear combinations with the

74

gluon states $B_1(2)$ and $B_2(2)$. Similar considerations apply to the states $a_2^{d\dagger}$ and $a_2^{s\dagger}$ whose linear combination we can identify with the gluon state $E(2)$. The total energy for these four states is given by

$$E_2^2 = E_0^2 + 8\pi\sigma + p_3^2, \qquad (3.64)$$

where, using eq. (3.40), $p_3 = \frac{4\pi}{L}$.

- The state $a_1^{s\dagger}\tilde{a}_1^{d\dagger} - a_1^{d\dagger}\tilde{a}_1^{s\dagger}$ is an eigenstate of both the $\mathcal{R}$-parity operator and $\mathcal{P}$-parity operator with eigenvalues -1, in agreement with our identification with the gluon state $A_{2u}(0)$. Similar considerations apply to the other states with momentum $p = 0$. Their total energy is

$$E_2^2 = E_0^2 + 8\pi\sigma. \qquad (3.65)$$

Therefore, in the second level there is a fine structure predicted by this string model between the states with momentum $p = 0$ and momentum $p = 2$.

3.5 Comparison with the QCD flux tube

The spectrum shown in Fig. 3-1 provides clear evidence that the gluon field as obtained in the previous chapter, can be well approximated by an effective string theory for large flux length L. In order to systematically compare the spectrum of gluonic excitations of a periodic QCD flux tube with the spectrum predicted by an effective string theory, such as the one derived by Polchinski and Strominger, we need to address three issues: the Lüscher term, level ordering and level degeneracy and the energy gap between levels.

Lüscher term

The transverse size of the hadronic flux tube is expected to be larger than 0.5 fm [52]. This corresponds, with our lattice spacing set at ≈ 0.21 fm , to about 2-3 lattice spacings. Thus any effective string theory should only apply for lengths greater than this transverse size [1]. In our studies we are considering a string of length greater than 1.6 fm thus we are far from the critical value of 0.5 fm. The ground state energy, given in eq. (3.61), at large L gives the usual formula

$$E(L) = \sigma L - \pi/(3L). \tag{3.67}$$

Fitting L from 8 to 20, using the data presented in the last chapter, to the function $f(L) = AL + B/L$ we obtain an acceptable fit with

$$A = 0.04145(17), \quad B = -0.183(16), \quad \chi^2/\text{dof} = 1.4, \tag{3.68}$$

where the parameter B is close to the expected value $\pi/3\xi = 0.170(3)$ (the value of the renormalized anisotropy is taken to be $\xi = 6.16(11)$). Attempts to fit to the function $f(L) = AL$ gave an unacceptable value for χ^2/dof.[2]

The plot of

---

[1]Various authors tried to give an answer to the question: when is a string "long"?
G. Bali in Ref. [7] suggested that, because of the form of the ground state energy, given by

$$E(L) = \sigma L \sqrt{1 - \frac{2\pi}{3\sigma L^2}} \tag{3.66}$$

the string picture at best applies to distance $L \gg L_c = \sqrt{\frac{2\pi}{3\sigma}} \approx 0.65$ fm, since $1/\sqrt{\sigma} \approx 0.45$ fm.
B. Lucini and M. Teper in Ref. [45] suggested that $\xi_\sigma \equiv 1/\sqrt{\sigma}$ provides the natural length scale for the physics of the confining flux tube and therefore a string of length $L/\xi_\sigma = L\sqrt{\sigma} \gg 1$ (thus $L \gg 0.45$ fm) can be considered long.

[2]We also fit the ground state in its form $E^2 = \sigma^2 L^2 - \frac{2}{3}\pi\sigma$ to the function $f(x) = A^2 x + BA$ obtaining

$$A = 0.04142(17), \quad B = -0.351(31), \quad \chi^2/\text{dof} = 1.5, \tag{3.69}$$

where the parameter B is close to the expected value $\frac{2}{3}\frac{\pi}{\xi} = 0.340(6)$.

$$E(L)/L = \sigma - \frac{\pi}{3L^2}, \tag{3.70}$$

in Fig 3-2 best illustrates the presence of the Lüscher term in our results. The correction L^{-1} in eq. (3.67) expected by an effective string theory is slowly decreasing and it is not obvious when it can be considered negligible. From our fit data, it is an empirical observation that this term could be considered negligible when it is of the same order as the error estimate for A as given by eq. (3.68), i.e.

$$\frac{\pi}{3\xi L} \approx O(\sigma_A)L, \tag{3.71}$$

which implies $L > 3$ fm. In the case of a string with fixed ends one has to take into account the self energy of the static ends. The ground state energy

$$E(L) = V_0 + \sigma L - \pi/(12L), \tag{3.72}$$

shows that the constant V_0 tends to obscure the contribution $\pi/(12L)$ coming from the self energy of the quantum fluctuations of the string. A torelon has no such "end effects" and also its contribution to the L^{-1} term is four times bigger than for a fixed end string. These observations suggest that it could be easier to detect the presence of the Lüscher term using closed strings.

Level orderings

For $1.5 < L < 2$ fm the level orderings of some states are not consistent with the expectations from an effective string theory. In particular the $A_{2u}(0)$ and $A_2(1)$ states, in the second and third level respectively, seem to undergo a crossover above 2 fm as shown in Fig. 3-1. It is worth noting that the quark-antiquark spectrum as reported by Juge et al. [37] exhibits a similar behavior

(even though for earlier L) exactly for these same states that according to their notation are to be identified with Σ_u^- and Σ^-. For $L > 2$ fm the levels agree without exception with the orderings expected from an effective string theory.

Level degeneracy

For $1.5 < L < 2$ fm the level degeneracy of the $A_{2u}(0)$ and $A_2(1)$ states, as expected from an effective string theory, is lost, and for the other states is approximate. For $L > 2$ fm we see that the $A_{2u}(0)$ state seems to slowly reach the right degeneracy with the states belonging to its level group. The degeneracy of the second level, approximated at around 2.5 fm, is perfect for flux length up to 4 fm as shown in Fig. 3-4[3]. In order to check this striking behavior of the periodic flux tube we tested these degeneracies using two different values of the lattice spacings $a_s = 0.21$ fm and $a_s = 0.17$ fm for the flux tube with $L = 3.3$ fm. The results are shown in Figs 3-7 and 3-8. It is worth stressing that in the second level the split between the two groups of states with different momenta ($p = 0$ and $p = 2$) and its decrease with L is expected by any effective string theory, as described in the previous section. It could be interesting to check the L^{-3} dependence, however, even if our data qualitatively agree with this expectation, we need more simulations above 2 fm in order to prove it quantitatively.

In the third level the problematic state $A_2(1)$ never reaches the degeneracy with the other three states belonging to its level group, at least for the lengths L considered here.

Energy gap

For $1.5 < L < 2.5$ fm the energy gaps agree surprisingly well with the string expectation for all levels $N = 0, 1, 2, 3$ as shown in Figs. 3-2,..,3-6. Polchinski

---

[3]For the simulation at 4 fm the error-bars are slightly bigger. This last simulation was performed in order to confirm that the perfect degeneracy seen at 3 fm was conserved for $L > 3$ fm. We therefore did not consider it necessary to reduce further the error-bars by increasing the statistics.

and Strominger claim in Ref. [55] that their procedure, briefly summarized in the previous sections, can be continued to find higher order corrections to the action in eq. (3.3) and in particular they give hints for corrections of order L^{-4}. However, it is our opinion that, at least in the range of flux lengths we are considering, these terms would probably not add any useful information to our numerical studies. However the most tantalizing behavior is the deviation for flux of length $L > 2.5$ fm from the effective string theory of Polchinski and Strominger and from Nambu-Goto. These deviations make the applicability of an effective string theory problematic. The spectrum of the static quark-antiquark system studied by Juge et al. in Ref [36] presents a similar behavior for long separations [4] .
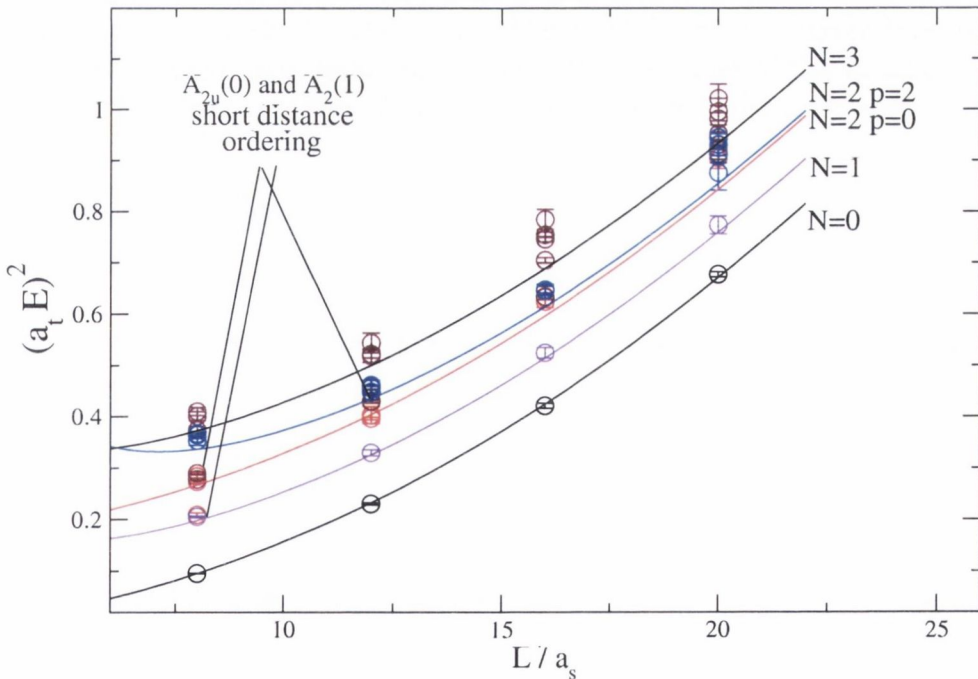

Figure 3-1: The spectrum of gluonic excitations for a periodic flux tube of length L. The crossover of the two states $A_{2u}(0)$ and $A_2(1)$ is shown. The lines represent the Nambu-Goto formula in lattice units.

---

[4] I would like to acknowledge my debt to Prof. Kuti for the advice he gave me to plot the energy gaps for all levels as $E^2(L)$ against the length L. This makes the equivalence between the Nambu-Goto and Polchinski-Strominger spectrum clear up to the order presented in Ref. [55].

and Strominger claim in Ref. [55] that their procedure, briefly summarized in the previous sections, can be continued to find higher order corrections to the action in eq. (3.3) and in particular they give hints for corrections of order L^{-4}. However, it is our opinion that, at least in the range of flux lengths we are considering, these terms would probably not add any useful information to our numerical studies. However the most tantalizing behavior is the deviation for flux of length $L > 2.5$ fm from the effective string theory of Polchinski and Strominger and from Nambu-Goto. These deviations make the applicability of an effective string theory problematic. The spectrum of the static quark-antiquark system studied by Juge et al. in Ref [36] presents a similar behavior for long separations [4].
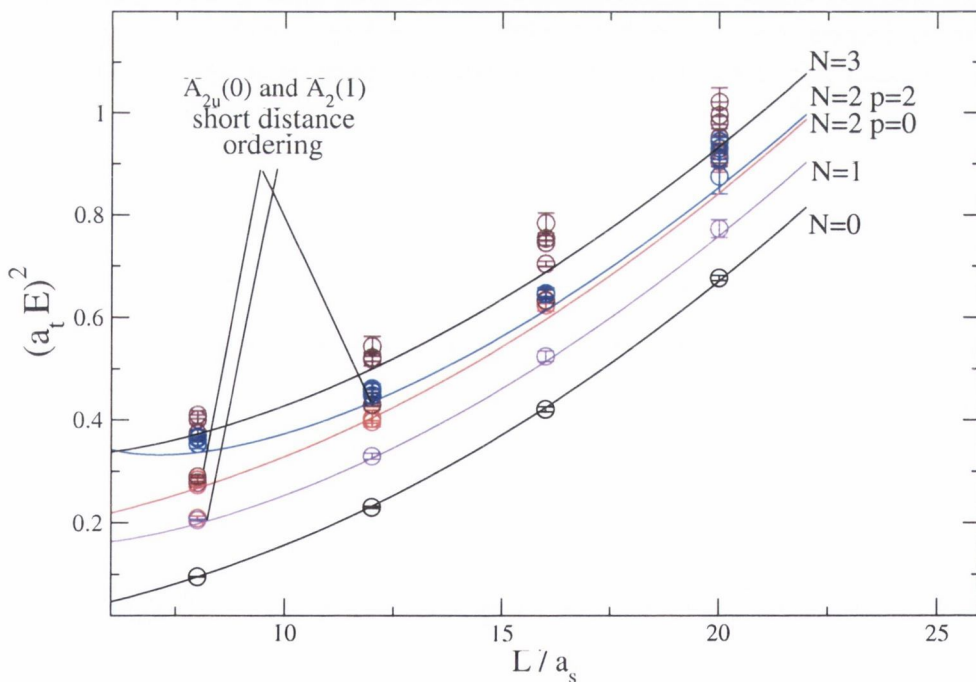
Torelon excitations

Figure 3-1: The spectrum of gluonic excitations for a periodic flux tube of length L. The crossover of the two states $A_{2u}(0)$ and $A_2(1)$ is shown. The lines represent the Nambu-Goto formula in lattice units.

---

[4]I would like to acknowledge my debt to Prof. Kuti for the advice he gave me to plot the energy gaps for all levels as $E^2(L)$ against the length L. This makes the equivalence between the Nambu-Goto and Polchinski-Strominger spectrum clear up to the order presented in Ref. [55].
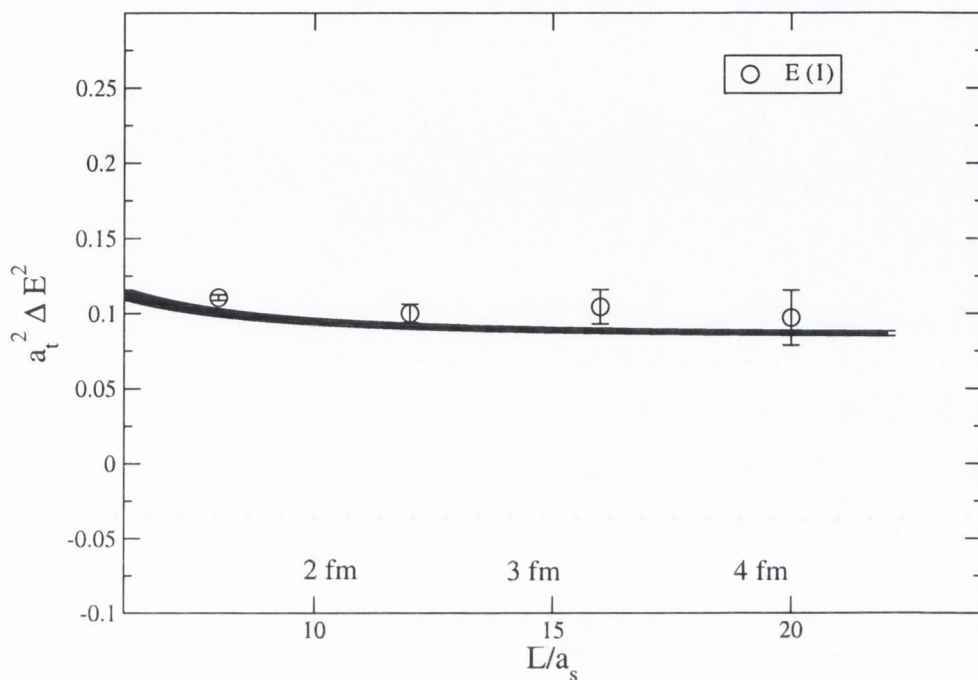
Figure 3-3: The first energy gap above the ground state $E_1^2 = E_0^2 + 4\pi\sigma + p_3^2$. The results are shown against the length of the periodic flux tube L. The line represents the Nambu-Goto formula in lattice units and its width takes into account the errors in the estimation of the string tension and the anisotropy.
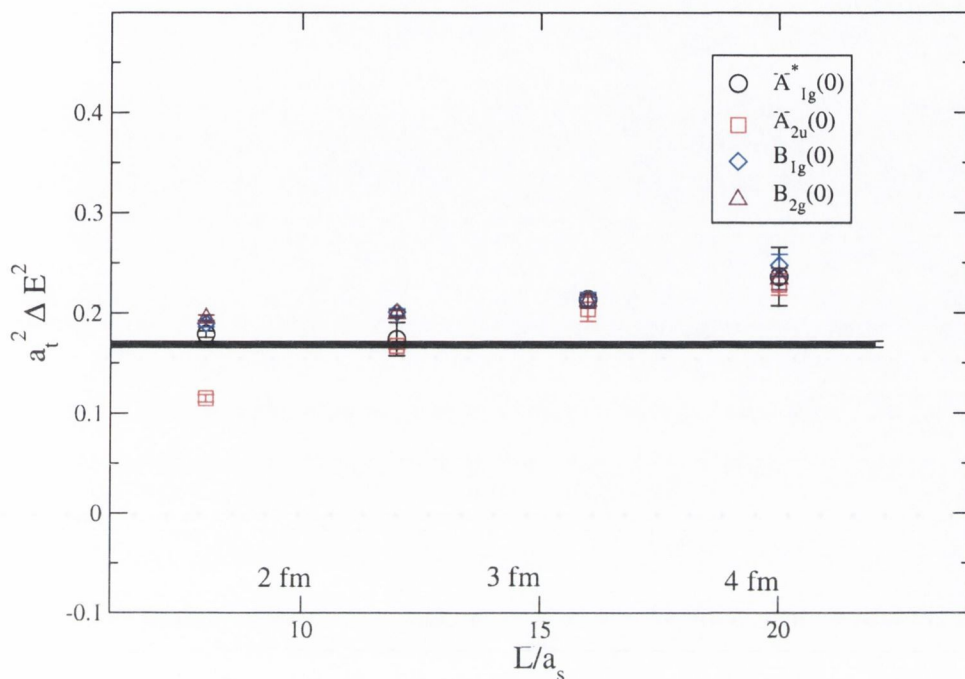
Figure 3-4: The second energy gap above the ground state $E_2^2 = E_0^2 + 8\pi\sigma$. The results are shown against the length of the periodic flux tube L. The line represents the Nambu-Goto formula in lattice units and its width takes into account the errors in the estimation of the string tension and the anisotropy.
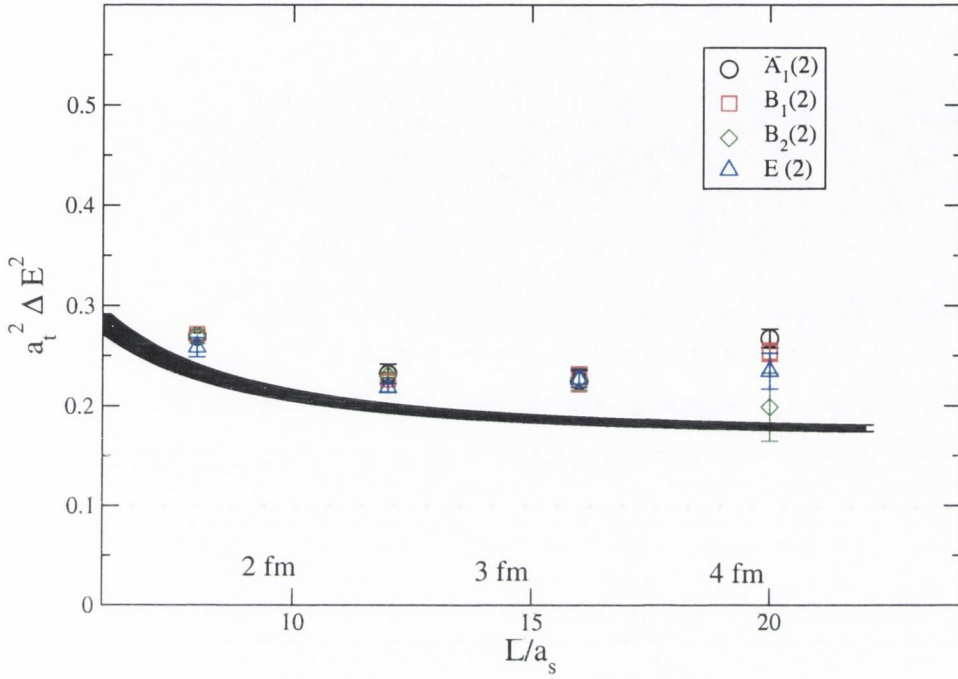
Figure 3-5: The second energy gap above the ground state $E_2^2 = E_0^2 + 8\pi\sigma + p_3^2$. The results are shown against the length of the periodic flux tube L. The line represents the Nambu-Goto formula in lattice units and its width takes into account the errors in the estimation of the string tension and the anisotropy.

N=3 string level

Figure 3-6: The third energy gap above the ground state $E_3^2 = E_0^2 + 12\pi\sigma + p_3^2$. The results are shown against the length of the periodic flux tube L. The line represents the Nambu-Goto formula in lattice units and its width takes into account the errors in the estimation of the string tension and the anisotropy.

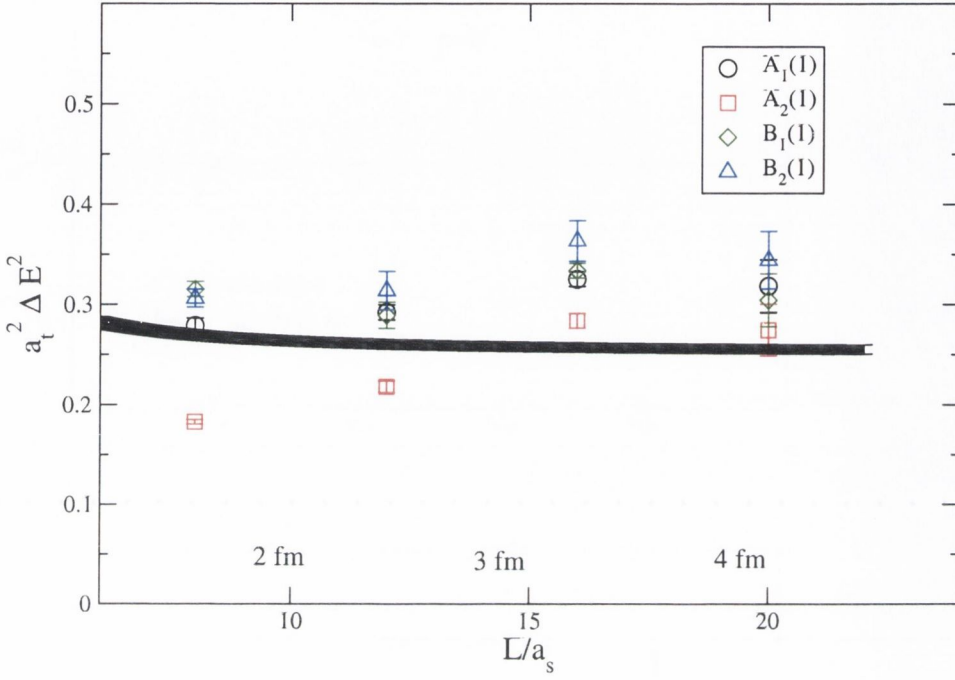Figure 3-7: Degeneracies for the string level N=2 for the states with p=0 obtained in two simulations with different lattice spacings and same physical volume of 3.3 fm.
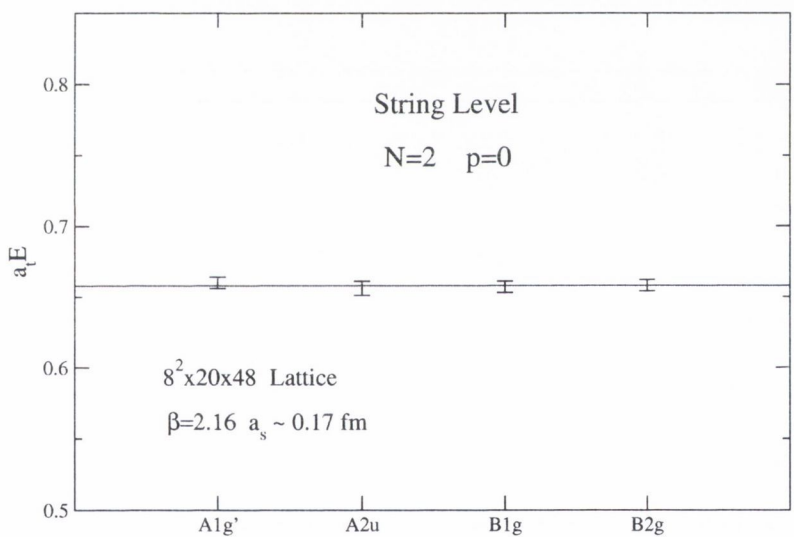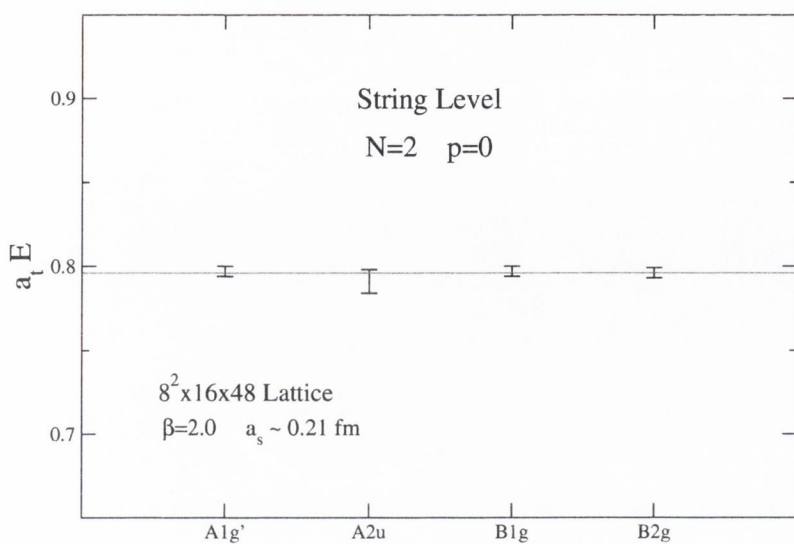
Figure 3-8: Degeneracies for the string level N=2 for the states with p=2 obtained in two simulations with different lattice spacings and same physical volume of 3.3 fm.
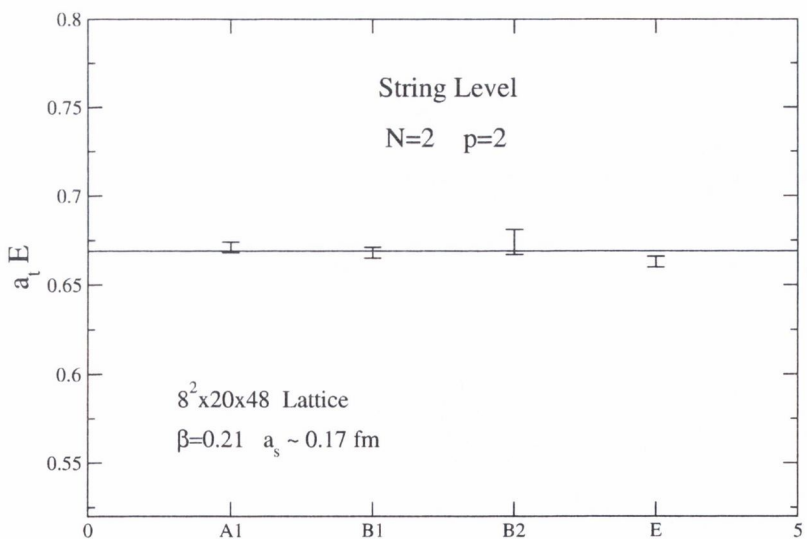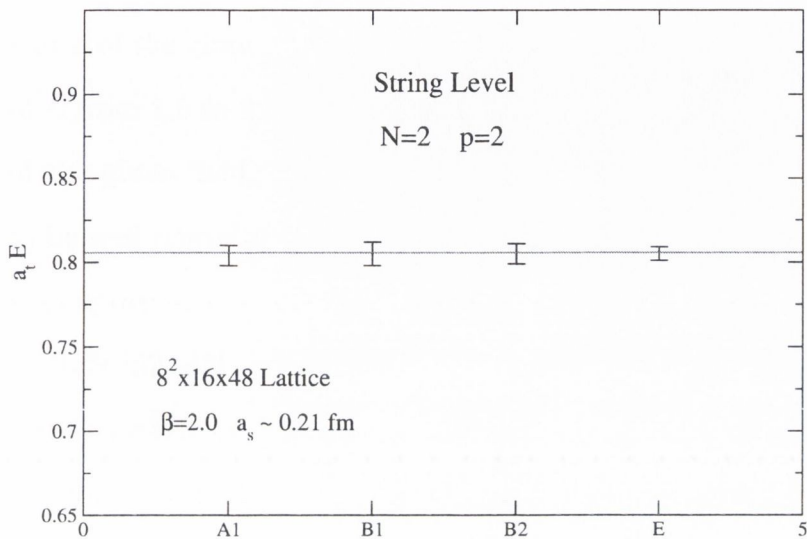
3.6 Comments and comparison with the literature

In this chapter, Monte Carlo computations of the energies of fourteen stationary states of the gluon field of a periodic flux tube of length L were presented for a range of L from 1.5 to 4 fm. We found a striking confirmation of string-like flux formation of the gluon field. In particular the Lüscher term predicted by string theory seems to be well reproduced by our numerical calculations of the ground state energy. This is in agreement with previous numerical studies of a periodic flux tube as presented in Refs [52, 45]. In order to compare our numerical results to an effective string theory we also addressed three important issues: level ordering, level degeneracy and the energy gaps between levels. The string-like level ordering is soon reached at 1.6 fm for all the states apart from the two problematic $A_{2u}(0)$ and $A_2(1)$ states. The $A_{2u}(0)$ state reaches the level order expected by string theory between 1.5 and 2.5 fm while the $A_2(1)$ state surprisingly a bit later. The string-like degeneracies of the states considered in this study are also well established for length L greater than 2 fm, apart from the problematic $A_2(1)$ state. An interesting observation on the $A_{2u}(0)$ state is that its energy with respect to the ground state is kept constant, $\Delta E = E(A_{2u}) - E(A_{1g}) \approx 855$ MeV for intermediate distances. An ongoing study on its excited state could reveal a new interesting physical interpretation for this state for lengths $1.5 < L < 2.5$ fm. The energy gap of the first excited state of the spectrum of a periodic flux tube seems to follow the Nambu-Goto expectation for all lengths $L > 1.5$ fm, while the higher energy gaps (N=2 and N=3) seem to deviate from the string expectation for lengths $L > 2.5$ fm. These deviations challenge an effective string theory and they are also present in the spectrum of a static quark-antiquark potential [36].

Conclusions

The main object of the first part of this work was the description of the lattice technology and methodology used to evaluate the spectrum of a periodic flux tube. The first step was to describe an improved anisotropic lattice action that C. Morningstar and M. Peardon proved, in their calculations of the glueball spectrum, to have good scaling behavior. We then described the methodology we adopted in order to identify the symmetries of a periodic flux tube that winds around one direction. In fact an extensive use of the properties of the center symmetry allowed us to reduce the symmetries we have to consider when studying a periodic flux tube. A large number of torelon operators were then systematically constructed. Details on the implementation and on the form of these operators are also given, since there was no previous description in the literature to date. Smearing and variational methods were then applied. We performed several long numerical Monte Carlo simulations for different flux lengths in order to evaluate the energy of each operator with the quantum numbers desired. Convincing plateau were observed in all effective energies confirming the quality of the torelon operators we built. Simulations with different volumes and different values of β were also performed in order to study finite volume and lattice spacing artefacts. However a clean extrapolation to the continuum seems problematic since it is required to fix the physical volume exactly at the same size while varying the value of β. It is also important to evaluate with higher precision the renormalization in the anisotropy ξ_R. In order to evaluate the renormalized anisotropy ξ_R, the calculation of the torelon dispersion relation seems to be cleaner

than the sideways potential method, however we still need to reduce further the errors we obtained. The second part of this work is dedicated to the description of an effective string theory with central charge not equal to the dimension d and the resulting covariant quantization with $d - 2$ oscillators presented by Polchinski and Strominger in 1991. However, as it is also clear from their article, the spectrum, derived from it, does not deviate from the Nambu-Goto spectrum at least for the corrections they introduced. We then proceeded in comparing the spectrum of the QCD periodic flux tube with the string expectations. Our numerical results confirm the string-like flux formation and details are given regarding the Lüscher term in the ground state, the level ordering, degeneracy and energy gaps between levels. The agreement with a string theory is striking in the level ordering and in the degeneracy of all of the fourteen states we considered, apart from the $A_{2u}(0)$ state that reaches a perfect degeneracy only at $L > 2.5$ fm and the problematic $A_2(1)$ state which seems to have a string-like behavior for bigger L. Further investigations on the nature of these problematic states for intermediate lengths are still ongoing. The deviations from the string energy gap for lengths $L > 2.5$ fm is problematic and already seen in the spectrum of a quark-antiquark system. It is not clear what the source of these deviations is.

Appendix A

Group theory

It is convenient to begin this section with a brief discussion of the background group theory that is necessary for building irreducible representations of the point-symmetry group $C_{4\nu} \otimes \mathbb{Z}_2(R)$. The simplest procedure for finding the representations of $C_{4\nu} \otimes \mathbb{Z}_2(R)$ is to consider first the abelian subgroup C_4, which has only four elements: the identity E and the rotations by $\frac{\pi}{2}$, π and $\frac{3\pi}{2}$, named C_{4z}, C_{2z} and C_{4z}^{-1} respectively. Since the number of classes in an abelian group is equal to the order of the group we have four irreducible representations, all of them one dimensional. From the fact that $C_{2z}^2 = E$, $C_{2z} = C_{4z}^2$ and $C_{2z}C_{4z} = C_{4z}^{-1}$ it is easy to build the character table of the group.

C_4	E	C_{4z}	C_{2z}	C_{4z}^{-1}
$A; z$	1	1	1	1
B	1	-1	1	-1
$E; x \pm iy$	1	i	-1	-i
	1	-i	-1	i

Here we follow the usual notation for the representations: one dimensional representations are denoted by A or B, depending on whether the basis function is symmetric or antisymmetric with respect to rotation about the principal axis (that has been

chosen to be z), while the two one-dimensional representations denoted by E are complex conjugate. This will be more apparent later, once a basis for each representation has been found. In order to do so, let us consider the general element v, which in our problem of finding gluonic operators that transform irreducibly under C_4 will correspond to a general shape of torelon, but could, in general, be a three dimensional vector or a function $f(x, y, z)$. Recalling that the character projection operator for each irreducible representation is defined as

$$P = \frac{1}{g} \sum_{T \in G} \chi(T)^\star O(T), \tag{A.1}$$

where $\chi(T)$ is the character of the operation $O(T)$ and $g = 4$ is the order of the group, we can build a basis for each irreps $\Gamma(T)$

$$v_A = P^A v = \frac{1}{4}(O(E)v + O(C_{4z})v + O(C_{2z})v + O(C_{4z}^{-1})v), \tag{A.2}$$

$$v_B = P^B v = \frac{1}{4}(O(E)v - O(C_{4z})v + O(C_{2z})v - O(C_{4z}^{-1})v), \tag{A.3}$$

$$v_E = P^E v = \frac{1}{4}(O(E)v + iO(C_{4z})v - O(C_{2z})v - iO(C_{4z}^{-1})v), \tag{A.4}$$

and its complex conjugate

$$v_E = P^E v = \frac{1}{4}(O(E)v - iO(C_{4z})v - O(C_{2z})v + iO(C_{4z}^{-1})v), \tag{A.5}$$

where for instance $O(C_{4z})v$ is a loop with the shape obtained rotating of $\frac{\pi}{2}$ the initial loop v. For example, the graphical representation of eq. (A.3) is illustrated in the following figure:
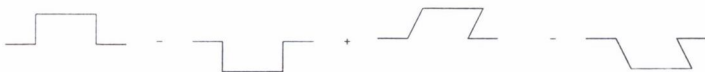
for the simplest staple

It is easy to check that v^R with $R = A, B, E$ transforms irreducibly, since $O(T)v^R = \chi(T)v^R$ for all $T \in C_4$ (for one dimensional representation $\chi(T) = \Gamma(T)$), thus v^R, given by eq. (A.2)-(A.5) is a basis function for the corresponding one-dimensional representation R. In order to label each of these representations with the corresponding value of the irreducible representation j of the continuum group, $SO(2)$, it is best to note that, as any abelian group, C_4 is a cyclic group (of order 4) with generator C_{4z}, since $C_{4z}^4 = E$ as expected. Thus the characters can be written as $\chi(C_{4z}^m) = e^{\frac{2\pi i m j}{4}}$ with $j = 0, 1, 2, 3$. Looking at the table above we can therefore make the following identifications: the representation A corresponds to $j = 0$, B to $j = 2$, E to $j = 3$ and its conjugate to E to $j = 1$. Also note that the states that transform irreducibly under a representation labelled by j, transform irreducibly also under $j' = j \pm 4k$ for $k = 0, \pm 1, \pm 2 \ldots$.

We can now easily generalize the procedure to the non abelian group $C_{4\nu}$: it is the semi direct product $C_4 \otimes \mathbb{Z}_2(\mathcal{P})$ where $\mathbb{Z}_2(\mathcal{P}) = \{E, IC_{2x}\}$, IC_{2x} being the reflection in the plane passing through the principal axis z. Thus the group $C_{4\nu}$ consists of 8 elements: the four elements of C_4, $\{E, C_{4z}, C_{2z}, C_{4z}^{-1}\}$, and the four elements obtained by group multiplication of IC_{2x} with them:
$\{IC_{2x}, IC_{2a} = IC_{2x}C_{4z}, IC_{2b} = IC_{2x}IC_{4z}^{-1}, IC_{2y} = IC_{2x}C_{2z}\}$. It is easy to check that they form 5 classes:

- $C_1 = \{E\}$,

- $C_2 = \{C_{2z}\}$,

- $C_3 = \{C_{4z}, C_{4z}^{-1}\}$,

- $C_4 = \{IC_{2x}, C_{2y}\}$,

- $C_5 = \{IC_{2a}, C_{2b}\}$.

Since the sum of the square of the dimensions d_i $(i = 1, \ldots, 5)$ of the inequivalent irrep is equivalent to the order of the group G there are 5 irreducible representations with dimensions $d_1 = d_2 = d_3 = d_4 = 1$ and $d_5 = 2$. The simplest procedure for finding the representations is to start from those previously determined for C_4, which, as already noted, is a subgroup of $C_{4\nu}$. The eigenvalues of IC_{2x} are ± 1, since $IC_{2x}^2 = E$. Hence taking the basis function v_A of the representation A of C_4 we have either $O(IC_{2x})v_A = \pm v_A$. Thus we obtain both the character table and the basis functions of the two one-dimensional representations A_1 and A_2, symmetric and antisymmetric under the reflection IC_{2x}, given respectively by

$$v_{A_1} = v_A + O(IC_{2x})v_A, \tag{A.6}$$

$$v_{A_2} = v_A - O(IC_{2x})v_A. \tag{A.7}$$

These two representations correspond to the continuum states given by $0^\pm$. Similarly, taking the basis function v_B of the representation B of C_4 we obtain both the character table and the basis functions of the two one-dimensional irreducible representations B_1 and B_2 by

$$v_{B_1} = v_B + O(IC_{2x})v_B, \tag{A.8}$$

$$v_{B_2} = v_B - O(IC_{2x})v_B. \tag{A.9}$$

These two representations correspond to the continuum states given by $2^\pm$. The characters of the two-dimensional representation can now be found using the following property

$$\frac{1}{g} \sum_{T \in G} \chi^p(T)^\star \chi^q(T) = \delta_{pq} \ i \neq j, \tag{A.10}$$

where g is the order of the group, $g = 8$. In particular we have to impose the following conditions:

$$\chi(C_1) + \chi(C_2) + 2\chi(C_3) + 2\chi(C_4) + 2\chi(C_5) = 0, \tag{A.11}$$

$$\chi(C_1) + \chi(C_2) - 2\chi(C_3) + 2\chi(C_4) - 2\chi(C_5) = 0, \tag{A.12}$$

$$\chi(C_1) + \chi(C_2) + 2\chi(C_3) - 2\chi(C_4) - 2\chi(C_5) = 0, \tag{A.13}$$

$$\chi(C_1) + \chi(C_2) - 2\chi(C_3) - 2\chi(C_4) + 2\chi(C_5) = 0, \tag{A.14}$$

Also, since a representation is irreducible if and only if

$$\frac{1}{g} \sum_{T \in G} |\chi(T)|^2 = 1,$$

we have to impose the following condition

$$|\chi(C_1)|^2 + |\chi(C_2)|^2 + 2|\chi(C_3)|^2 + 2|\chi(C_4)|^2 + 2|\chi(C_5)|^2 = 8. \tag{A.15}$$

From these five equations we obtain $\chi(C_1) = 2$, $\chi(C_2) = -2$ and $\chi(C_3) = \chi(C_4) = \chi(C_5) = 0$. The complete character table is here illustrated.

C_{4v}	J^P	E	C_{4z}	C_{2z}	C_{4z}^{-1}	IC_{2x}	IC_{2a}	IC_{2y}	IC_{2b}
A_1	0^+	1	1	1	1	1	1	1	1
A_2	0^-	1	1	1	1	-1	-1	-1	-1
B_1	2^+	1	-1	1	-1	1	-1	1	-1
B_2	2^-	1	-1	1	-1	-1	1	-1	1
E	1	2	0	0	-2	0	0	0	0

In order to obtain the two basis functions for this two-dimensional representation we employ the character projection operator P of eq (A.1). Since we are dealing with a two dimensional representation the procedure is not as straightforward as it was when we derived the basis function of the one-dimensional representations for C_{4v}. The steps are the following:

- Take a test state $\mathbf{u}$ such that $P\mathbf{u}$ is not identically zero.

- Construct $O(T)P\,\mathbf{u}$ for each transformation $T \in G$.

- From these states extract $d = 2$ linearly independent states.

Following the steps above it is easy to build the following two basis functions:

$$\mathbf{u^1} = \begin{pmatrix} O(E)v - O(C_{2z})v - O(IC_{2x})v + O(IC_{2y})v \\ -O(C_{4z})v + O(C_{4z}^{-1})v + O(IC_{2a})v - O(IC_{2b})v \end{pmatrix}, \qquad (A.16)$$

and

$$\mathbf{u^2} = \begin{pmatrix} O(C_{4z})v - O(C_{4z}^{-1})v + O(IC_{2a})v - O(IC_{2b})v \\ O(E)v - O(C_{2z})v + O(IC_{2x})v - O(IC_{2y})v \end{pmatrix}, \qquad (A.17)$$

where again v can take any torelon shape. The basis functions for each representation are summarized in the following table.

C_{4v}	J^P	E	C_{4z}	C_{2z}	C_{4z}^{-1}	IC_{2x}	IC_{2a}	IC_{2y}	IC_{2b}
A_1	0^+	1	1	1	1	1	1	1	1
A_2	0^-	1	1	1	1	-1	-1	-1	-1
B_1	2^+	1	-1	1	-1	1	-1	1	-1
B_2	2^-	1	-1	1	-1	-1	1	-1	1
E	1	$\begin{smallmatrix}1 & 0\\0 & 1\end{smallmatrix}$	$\begin{smallmatrix}0 & -1\\1 & 0\end{smallmatrix}$	$\begin{smallmatrix}-1 & 0\\0 & -1\end{smallmatrix}$	$\begin{smallmatrix}0 & 1\\-1 & 0\end{smallmatrix}$	$\begin{smallmatrix}-1 & 0\\0 & 1\end{smallmatrix}$	$\begin{smallmatrix}0 & 1\\1 & 0\end{smallmatrix}$	$\begin{smallmatrix}1 & 0\\0 & -1\end{smallmatrix}$	$\begin{smallmatrix}0 & -1\\-1 & 0\end{smallmatrix}$

The irreducible representations of C_{4v} could have been found, in a more formal way using the induced representation method on the group C_4, that is, however, a lengthy method.

It is easy now to solve the problem of finding irreducible representation for the direct product $C_{4v} \otimes \mathbb{Z}_2(\mathcal{R})$ where $\mathbb{Z}_2(\mathcal{R})$ is the group with just two elements $\mathbb{Z}_2(\mathcal{R}) = \{E, \mathcal{R}\}$ and $\mathcal{R}$ is the reflection on the plane perpendicular to the principal axis z. In fact each representation of C_{4v} gives rise to two representations of the direct product, one which is symmetric and one which is antisymmetric with respect to the reflection $\mathcal{R}$, denoted by the index u and g respectively.

Bibliography

[1] Greiner, Schramm and Stein, Quantum Chromodynamics, 2nd Edition

[2] J. Greensite, hep-lat/0301023.

[3] K.G. Wilson, Phys. Rev. D10, 2445 (1974).

[4] M. Lüscher and P. Weisz, JHEP 11 (2000) 030, hep-th/0207003.

[5] M. Lüscher and P. Weisz, Phys. Lett. B 158 (1985) 250.

[6] M. Lüscher, G. Münster and P. Weisz, Nucl. Phys. B 180 (1980) 1.

[7] G. S. Bali, hep-ph/0001312.

[8] C. Bachas, Phys. Rev. D33 (1986) 2723.

[9] K.G. Wilson, Rev. Mod. Phys. 55 (1983) 583.

[10] G.P. Lapage, Nucl. Phys. B (Proc. Suppl.) 47 (1996) 3.

[11] K. Symanzik, Nucl. Phys. B226 (1983) 187 & 205.

[12] G.P. Lepage, hep-lat/9607076

[13] Parisi, High Energy Physics 1980, AIP Conference Proceedings No 68

[14] G.P. Lepage and P.B. Mackenzie, Phys. Rev. D48 (1993) 2250

[15] C. Morningstar, hep-lat/9608019

[16] C. Morningstar and M. Peardon, hep-lat/9911003

[17] C. Morningstar and M. Peardon, Phys. Rev. D56, 4043 (1997).

[18] C. Morningstar and M. Peardon, Nucl. Phys. B (Proc. Suppl.) 47, 258 (1996).

[19] C. Morningstar and M. Peardon, Phys. Rev. D 60 (1999) 114501, hep-lat/9910007.

[20] M. Alford, W. Dimm, G.P. Lepage, G. Hockney and P. Mackenzie, Phys. Lett. B361 (1995) 87.

[21] M. Alford, I.T. Drummond, R.R. Horgan, H. Shanahan, M. Peardon hep-lat/0003019.

[22] R. Sommer hep-lat/9310022.

[23] A. Patel et al., Phys. Rev. Lett. 57, 1288 (1986).

[24] G. Bhanot and M. Creutz, Phys. Rev. D24 3212 (1981).

[25] G. Bhanot, Phys. Lett. B108 337 (1982).

[26] U. Heller, Phys. Lett. B 362, 123 (1995).

[27] U. Heller, Nucl. Phys. Proc. Suppl. 47 (1996) 262, hep-lat/9509010.

[28] T. Blum, C. DeTar, U. M. Heller, L. Kärkkäinen, K. Rummukainen and D. Toussaint, Nucl. Phys. B 442 (1995) 301, hep-lat/9412038.

[29] C. Morningstar and M. Peardon, hep-lat/9808045.

[30] H.B. Nielsen and P. Olesen, Nucl. Phys. B61 (1973) 45.

[31] G. 't Hooft, Nucl. Phys. B72 (1974) 461.

[32] G.S. Bali, K. Schilling, Ch. Schlichter, hep-lat/9409005.

[33] S. Necco, A. Sommer, Phys. Lett. B523 (2001) 135, hep-ph/0109093.

[34] S. Necco, Nucl. Phys. B 683 (2004) 137, hep-ph/0309017.

[35] M. Hasenbusch, S. Necco, hep-ph/0405012.

[36] J. Juge, J. Kuti, C. Morningstar, Phys. Rev. Lett. 90, 161601 (2003)

[37] J. Juge, J. Kuti, C. Morningstar, hep-lat/0312019

[38] J. Juge, J. Kuti, C. Morningstar, Nucl.Phys.Proc.Suppl.119:682-684,2003

[39] J. Juge, J. Kuti, C. Morningstar, Nucl.Phys.Proc.Suppl.106:691-693,2002

[40] J. Juge, J. Kuti, C. Morningstar, hep-lat/0103008

[41] J. Juge, J. Kuti, C. Morningstar, Nucl.Phys.Proc.Suppl.83:503-505,2000

[42] J. Juge, J. Kuti, C. Morningstar, Nucl.Phys.Proc.Suppl.73:590-595,1999

[43] J. Juge, J. Kuti, F. Marescaf, C. Morningstar, M. Peardon hep-lat/0309180

[44] A. Polchinski, Polyakov, Gauge Field and Strings, Harwood Academic Publishers, 1987

[45] B. Lucini and M. Teper, Phys. Rev. D64 (2001) 105019,hep-lat/0107007

[46] B. Berg and A. Billoire, Nucl.Phys.B221:109,1983

[47] M. Teper, Phys. Rev. D59:014512,1998, hep-lat/9804008

[48] M. Teper, Phys. Lett. B311 (1993) 223-229

[49] M. Teper, hep-lat/9812187

[50] A. Hart and M. Teper, Phys.Rev.D65:034502,2002, hep-lat/0108022

[51] M. Teper, Phys.Lett.B183:345,1987

[52] C. Michael and P.W. Stephenson, Phys.Rev.D50:4634-4638,1994

[53] C. Morningstar and M. Peardon, Phys.Rev.D69:054501,2004,hep-lat/0311018

[54] 0. Philipsen, M Teper and H. Wittig, hep-lat/9602006

[55] J. Polchinski and Strominger, Physical Review Letters 67, 13, 1991;

[56] J. Polchinski, String theory, Vol 1;

[57] Green, Schwarz, Witten, Superstring theory, Vol 1;

[58] Cornwell, Group Theory in Physics, Vol 1;

[59] Hamermesh, Group Theory and its application to physical problems;